Max-Planck-Institut für Kolloid- und Grenzflächenforschung
Abteilung für Grenzflächen

Feedback active coatings based on mesoporous silica containers

Dissertation

zur Erlangung des akademischen Grades
"doctor rerum naturalium"
(Dr. rer. nat.)
in der Wissenschaftsdisziplin "Physikalische Chemie"

eingereicht an der
Mathematisch-Naturwissenschaftlichen Fakultät
der Universität Potsdam

von

Dimitriya Borisova

Potsdam, den 1. Oktober 2012

Abstract

Metals are often used in environments that are conducive to corrosion, which leads to a reduction in their mechanical properties and durability. Coatings are applied to corrosion-prone metals such as aluminum alloys to inhibit the destructive surface process of corrosion in a passive or active way. Standard anticorrosive coatings function as a physical barrier between the material and the corrosive environment and provide passive protection only when intact. In contrast, active protection prevents or slows down corrosion even when the main barrier is damaged. The most effective industrially used active corrosion inhibition for aluminum alloys is provided by chromate conversion coatings. However, their toxicity and worldwide restriction provoke an urgent need for finding environmentally friendly corrosion preventing systems. A promising approach to replace the toxic chromate coatings is to embed particles containing nontoxic inhibitor in a passive coating matrix. This work presents the development and optimization of effective anticorrosive coatings for the industrially important aluminum alloy, AA2024-T3 using this approach.

The protective coatings were prepared by dispersing mesoporous silica containers, loaded with the nontoxic corrosion inhibitor 2-mercaptobenzothiazole, in a passive sol-gel (SiO_x/ZrO_x) or organic water-based layer. Two types of porous silica containers with different sizes (d ≈ 80 and 700 nm, respectively) were investigated. The studied robust containers exhibit high surface area (≈ 1000 m^2 g^{-1}), narrow pore size distribution (d_{pore} ≈ 3 nm) and large pore volume (≈ 1 mL g^{-1}) as determined by N_2 sorption measurements. These properties favored the subsequent adsorption and storage of a relatively large amount of inhibitor as well as its release in response to pH changes induced by the corrosion process.[1]

The concentration, position and size of the embedded containers were varied to ascertain the optimum conditions for overall anticorrosion performance. Attaining high anticorrosion efficiency was found to require a compromise between delivering an optimal amount of corrosion inhibitor and preserving the coating barrier properties.[2-3] The barrier properties of the intact coatings were assessed with electrochemical impedance spectroscopy. The active corrosion inhibition was evaluated during a corrosion process using the scanning vibrating electrode technique.

This study broadens the knowledge about the main factors influencing the coating anticorrosion efficiency and assists the development of optimum active anticorrosive coatings doped with inhibitor loaded containers.

1. D. Borisova; H. Möhwald; D.G. Shchukin, ACS Nano 2011, 5(3), 1939-1946.
2. D. Borisova; H. Möhwald; D.G. Shchukin, ACS Applied Materials & Interfaces 2012, 4(6), 2931-2939.
3. D. Borisova; H. Möhwald; D.G. Shchukin, ACS Applied Materials & Interfaces 2012, submitted.

TABLE OF CONTENTS

LIST OF ABBREVIATIONS

BET	Brunauer-Emmet-Teller
cmc	critical micelle concentration
CPE	constant phase element
IEP	isoelectric point
IMPs	intermetallic particles
IUPAC	International Union of Pure and Applied Chemistry
LbL	layer-by-layer
MBT@NCs	mesoporous silica nanocontainers loaded with 2-mercaptobenzothiazole
MBT@SHS	spherical hollow silica containers loaded with 2-mercaptobenzothiazole
MSP	mesoporous silica particles
MWCO	molecular weight cut off
NCs	mesoporous silica nanocontainers
NLDFT	non-local density functional theory
PdI	polydispersity index
SDA	structure directing agent
SHS	spherical hollow silica containers
wt	weight
ρ_{sld}	scattering length density

Chemicals

8-HQ	8-hydroxyquinoline
BTA	1H-benzotriazole
CTAB	cetyltrimethylammonium bromide
CTACl	cetyltrimethylammonium chloride
EAA	ethyl acetoacetate
GPTMS	(3-glycidyloxypropyl) trimethoxysilane
MBT	2-mercaptobenzothiazole
MeBT	2-methylbenzothiazole
TEA	triethanolamine
TEOS	tetraethyl orthosilicate
TPOZ	tetra-n-propoxy-zirconium

Methods

DLS	dynamic light scattering
EDX	energy-dispersive X-ray spectroscopy
EIS	electrochemical impedance spectroscopy
SAXS	small-angle X-ray scattering
SEM	scanning electron microscopy
SVET	scanning vibrating electrode technique
TEM	transmission electron microscopy
TGA	thermogravimetric analysis
UV-Vis	ultraviolet-visible

1   Introduction

Metal destruction by corrosion leads to large maintenance costs in many industries.[1] The protection of metals from corrosion is a challenging task for materials science in view of increasing environmental requirements. For example, the development of non-chromated, "green alternatives" of potentially cancerogenous chromate conversion coatings for aluminum alloys used in aerospace industry has caused large research activity.[2-3] The search for replacements has led to a new generation of self-healing coatings providing both passive and active protection.[4] Passive protection is realized by intact coatings that function only as a physical barrier between the metal and the corrosive environment. In contrast, active protection offers corrosion inhibition when the coating is disrupted, and the barrier properties are lost. One strategy to actively protect metals from corrosion is by the direct addition of corrosion inhibitors to coatings. However, this approach has several drawbacks such as degradation of coating integrity, inhibitor deactivation or undesired leaching.[5-6]

A promising approach to avoid these disadvantages is the encapsulation of the corrosion inhibitors in containers dispersed in the coating. The embedded containers store the inhibitor and prevent any detrimental interaction with the coating matrix. There are reports on different encapsulation approaches using nanotubes,[7] porous inorganic nanocontainers,[8] layered double hydroxides,[9] polymer containers,[10] and nanocontainers with polyelectrolyte shells.[11] In all cases, the containers are first loaded with the active agent and then randomly dispersed in the whole coating matrix. The inhibitor is released when the barrier properties of the coating are lost, *i.e.* at coating rupture. This release is triggered by changes in the local environment in the damaged area, such as changes in the local pH, ionic strength, humidity or presence of aggressive ions.[12] The inhibitor molecules either deactivate the corrosive species or form a thin protective film over the exposed metal surface.[13-14] Thus the anticorrosive properties of the coating are recovered due to the active protection offered by the encapsulated inhibitor.

However, optimum corrosion inhibition can be obtained only after fulfilling certain technical requirements as: (i) homogeneous dispersion of the embedded containers; (ii) good compatibility of the embedded containers with the coating matrix; (iii) strong

adhesion of coating to metal surface; (iv) good coating barrier properties and (v) sufficient amount of available corrosion inhibitor. All these requirements are strongly influenced by the embedded containers and in particular, their size, concentration and position in the coating matrix. However, the influence of these important aspects on the overall coating performance has been scarcely described in the literature.

This work describes the optimization of the performance of active anticorrosive coatings by tuning the concentration, position and size of the embedded containers loaded with corrosion inhibitor. Mesoporous silica particles are used as containers due to their high loading capacity, structural stability, low toxicity, good compatibility with the used inorganic and organic coating matrices and inertness to inhibitor and coating matrix. The selected model inhibitor is the nontoxic 2-mercaptobenzothiazole (MBT), which is reported to be an effective corrosion inhibitor for the studied aluminum alloy, AA2024-T3.[13]

The physical and anticorrosive properties of the developed coating systems are studied in order to evaluate the effect of container concentration, position and size on the overall performance of the coatings. The optimum conditions for these factors are determined considering a balance between good coating barrier properties, efficient active inhibition and sufficient adhesion between the coating system components. As a result, active anticorrosive coatings with optimum anticorrosion performance are developed.

2   Fundamentals and literature survey

2.1 Feedback active systems

Feedback generally translates the information about the gap between the reference and the actual level of a system parameter into an action to alter the gap in some way.[15] Feedback is often part of naturally occurring or constructed systems. In a feedback system cause-and-effect relations between system variables form a closed-loop wherein the output couples back to the input.[16] In this way, a feedback system can respond to its environment. A typical block diagram of a feedback control system is shown in Figure 1. The input is an external signal applied to the system and represents the desired or reference value of a controlled variable. The output is the actual value of the controlled variable, which can be upset by the undesirable input signal of the disturbance acting on the system. The feedback elements sense the disturbance (change) in the system and identify the functional relationship between the output and the feedback signal. The feedback loop can either amplify or reduce the effect of the disturbance. Therefore, feedback systems are commonly divided into two types: positive and negative.
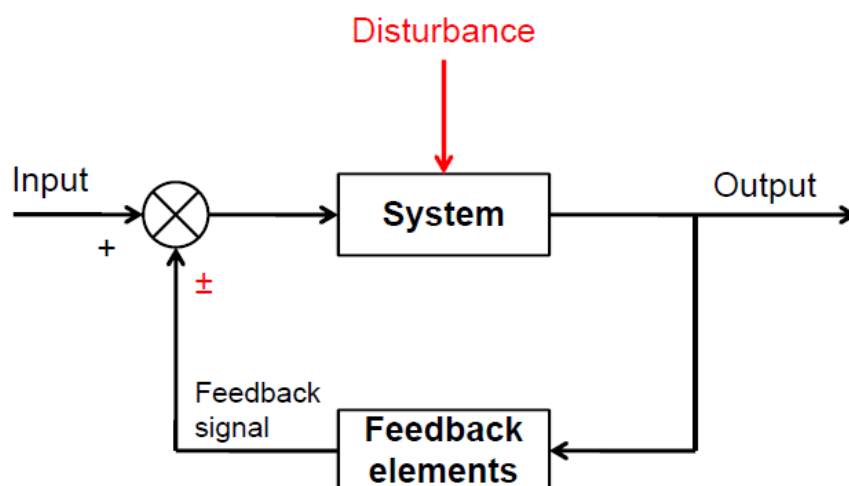

Figure 1.1 A general block diagram of a feedback control system.

In positive feedback systems the net gain around the feedback loop is positive and increases changes. Positive feedback is a process in which the effects of an outside disturbance (change) on a system are amplified instead of corrected.[17] System parameters will be changed from original equilibrium towards extreme values, which may lead to instability or a new stable state of the system. Blood clotting is an example of a useful positive feedback system in our body.[18] Upon rupture of a blood vessel wall, activated blood platelets release chemicals to attract even more platelets and form a sticky clot at the damaged site. The process continues until the hole in the blood vessel is sealed and the bleeding stopped. In fact, every useful positive feedback cycle is part of an overall negative feedback system. For example, the negative feedback system responsible for the maintenance of a normal blood volume includes the positive feedback clotting process.

A negative feedback system senses a change in the outside environment and opposes it to return the system to the equilibrium state.[15] If a disturbance (change) adds to a system output, the negative feedback acts to subtract or reverse the effect of the disturbance and keep the system stable. For example, negative feedback is used to control human body temperature. If body temperature increases above 37 °C, negative feedback increases the heat loss from the body by the production of more sweat in order to reduce the body temperature and restore the reference, normal body temperature (37 °C) essential for survival. Another practical example of a common negative feedback system is a thermostat. A change in the room temperature away from the set temperature of the thermostat is fed back to the heater and its function is directed in order to minimize the difference between reference and actual temperature. Thus, negative feedback restores the stability or desired function of a system by correcting an external disturbance (stimulus).

2.2 Feedback active coatings

Mimicking the concept of feedback active systems in the field of synthetic coatings opens up a number of opportunities for the development of "smart" coatings with stimuli-responsive behavior. Feedback active coatings undergo a change in response to an external stimulus (trigger) in order to enhance the system performance. These coatings are of great scientific and technological importance, as they can be applied in various fields such as medicine, biotechnology or material science. Their main, passive function as coatings is to protect the underlying substrate from contact with the environment. In addition to their barrier properties, they also possess active properties due to their environmentally responsive function.

A successful approach to impart feedback functionality to a coating is by the incorporation of encapsulated active material in the coating matrix.[19-20] The great versatility of encapsulation technologies, active agents and coating matrices offer an unlimited number of coating design strategies. However, feedback active coatings can be generally classified according to the external stimulus to which they respond. Various external **stimuli** of **mechanical, biological, physical or chemical** nature can cause a change in the coating followed by the self-recovery of an initial coating property.

2.2.1   Mechanical stimuli

Mechanical impact is an important external stimulus, which affects coating barrier properties in a negative way by causing microcracking or other microdamage in the coating. Using mechanical stress as a trigger to recover the mechanical stability by autonomic crack healing was demonstrated for the first time in 2001 by the group of S. R. White.[21] They encapsulated a healing agent (a monomer) in polymer microcapsules embedded in an epoxy matrix containing a catalyst. Upon crack formation the embedded microcapsules are ruptured and the healing agent is released in the crack due to capillary forces and comes into contact with the embedded catalyst. The resulting polymerization of the healing agent leads to crack healing and recovery of the barrier properties of the coating. Such coatings are defined as self-healing coatings and

the term "self-healing" refers to the restoration of an initial property or a function of a system in response to an external stimulus.[22]

Since the breakthrough in autonomic self-healing polymer materials, most of the efforts in designing feedback active coatings have been concentrated on encapsulating active materials within polymer microcapsules[23-27] or the core of a fiber[28-30] that rupture upon mechanical impact. Simultaneous incorporation of two types of capsules containing different active agents[31] or sub-micrometer size capsules filled with reactive epoxy resin[32-34] were also reported to lead to successful crack healing. Encapsulation of highly air-sensitive and moisture reactive materials, such as metal oxide precursors[35], organosiloxanes[10] or linseed oil[36] in polymer microcapsules is an interesting approach to design self-healing coatings, which respond to combined external stimuli, *e.g.* mechanical and chemical stimulus. In such coatings, the active material is first released due to crack propagation and forms an impermeable layer on the substrate only after oxidation or hydrolysis by atmospheric oxygen or humidity. Sometimes preserving the initial liquid state of the released active material can be advantageous. In self-lubricating coatings friction causes simultaneously fatigue and self-repair of the coating due to lubricant release triggered by crack propagation.[37-38] Successful self-healing in response to mechanical stress depends on the properties of the embedded microcapsules and active agents. The microcapsules size should be large enough (50 – 200 µm) to enable easy rupture and sufficient amount of active agent.[39] However, the integration of big microcapsules in thin coatings is limited. Microcapsule shells should be rigid to preserve the capsule integrity during embedding in the coating matrix and brittle to facilitate capsule rupture upon crack formation. The active agent should be of low viscosity and of excess amount to render multiple healing. Ideally, the active agents should be low-cost and nontoxic in order to make their application in industrial coatings attractive.

2.2.2   Biological stimuli

Microorganisms such as bacteria, fungi or viruses represent a biological disturbance in our modern hygienic lifestyle. Microbial adsorption and growth on coated surfaces may have various negative impacts like discoloration or malodor of the coating as well as microbial corrosion in the case of metallic substrates.[40-41] Feedback active antimicrobial

coatings respond to biofilm formation by the release of classical biocides, which either inhibit the growth of bacteria (biostatic) or kill them (biocidal). In order to enhance the durability and efficiency of antibacterial coatings, microcapsules containing biocides have also been embedded in the coating matrix.[42-44] For example, the commercially available product Caliwel™ based on this concept is claimed to retain antimicrobial activity for up to six years.[45] This is realized by the slow release of calcium hydroxide encapsulated in a latex membrane along with a stabiliser. The biocidal effect is caused by the very high pH value of calcium hydroxide, which can be lethal to microorganisms in contact.

Ships or constructions in coastal waters are exposed to the attack of marine organisms and their unwanted deposition and growth on coated surfaces known as "fouling". The prevention of this negative biological impact relies on the slow leakage of microencapsulated antifouling products, which are dispersed in the matrix of antifouling coatings.[46-47]

2.2.3   Physical stimuli

Electromagnetic irradiation (*e.g.* UV light) and temperature belong to the physical stimuli, which affect coating durability the most. However, the attractive feature of feedback active coatings is to utilize the factors that cause the most damage to the coating, (*e.g.* UV light or high temperature) and initiate self-healing.

Various kinds of polymeric microcapsules with light responsive properties are known and suitable for application in feedback active coatings.[48] For example many self-cleaning coatings are based on the photocatalyst titanium dioxide due to its photo-induced high oxidation power and hydrophilicity. Thus, self-cleaning coatings make use of the negative impact of UV irradiation to remove organic contaminants or microbial species from the coating and thus increase the longevity of the coating. Direct incorporation of photocatalytic TiO_2 particles in polymer coatings is difficult because it would lead to oxidation of the organic components of the coating matrix. However, recent developments have reported on the successful encapsulation and application of TiO_2 particles in organic self-cleaning coatings.[49-52]

Exposure to high temperature is usually unfavorable for classical coatings. However, in bioactive coatings it triggers the release of healing agent from the coating. The released

material can have antibacterial or anti-inflammatory effects. An example of a bioactive coating triggered by temperature to obtain antibacterial properties was recently reported.[53] The coating design is based on phospholipid vesicles loaded with healing agent (*e.g.* silver ions) and dispersed in a biocompatible polyelectrolyte coating. Upon a temperature increase above the main phase transition temperature of the vesicles, the encapsulated healing agent is released and diffuses out of the coating matrix.[54]

2.2.4   Chemical stimuli

External stimuli or changes in the local environment of a coating can also be of chemical nature (*e.g.* electrochemical potential, pH, ionic strength or humidity). Feedback active coatings containing hydrogels or microcapsules with a layer-by-layer assembled polyelectrolyte shell are especially responsive to chemical stimuli. Changes in pH, ionic strength, electrochemical potential or dielectric permeability of the solvent can trigger swelling/shrinkage of the capsules or permeability change of the capsule shells.[55-61] This property enables the release of encapsulated active material in response to external chemical stimuli and the consequent recovery of a coating function. For example, a feedback active coating based on polyelectrolyte microcapsules incorporated in a conducting polymer film was reported to demonstrate electrochemically reversible permeability in response to electrochemical potential change. Such coatings can be applied as a new generation of chemically rechargeable accumulators.[62]

A broad range of feedback active coatings responsive to a change of local pH or ionic strength can be used to control the delivery of active material (*e.g.* drugs, pesticides, fragrances or fertilizers) and find potential application in biomedicine, packaging or functional clothes.[63-64] Another possible application of huge scientific and industrial interest is as anticorrosive coatings. Such coatings can be classified as feedback active coatings, which utilize the corrosion process as a chemical stimulus (change in local pH or ionic strength) to self-recover their protective function. Since anticorrosive coatings are the class of feedback active coatings representing the main focus of this work, they will be described more thoroughly in the following chapter.

2.3 Anticorrosive coatings

2.3.1 Corrosion

Corrosion is the destructive process which affects almost all metals. It occurs when a metal is attacked by an oxidizing agent in its environment, leading to an irreversible oxidation-reduction reaction.[65] Corrosion constitutes a problem of huge importance due to its negative economical, environmental and safety impact.

The various forms in which corrosion occurs can be classified by three main factors: (i) nature of the corrodent, (ii) mechanism of corrosion and (iii) appearance of the corroded metal.[66-67] Especially useful in metal failure analysis is the classification by appearance. Since this classification varies between authors, only the following forms of corrosion, which are widely accepted and of importance for this work will be discussed: (i) uniform, (ii) galvanic, (iii) crevice and (iv) pitting corrosion (Figure 2).
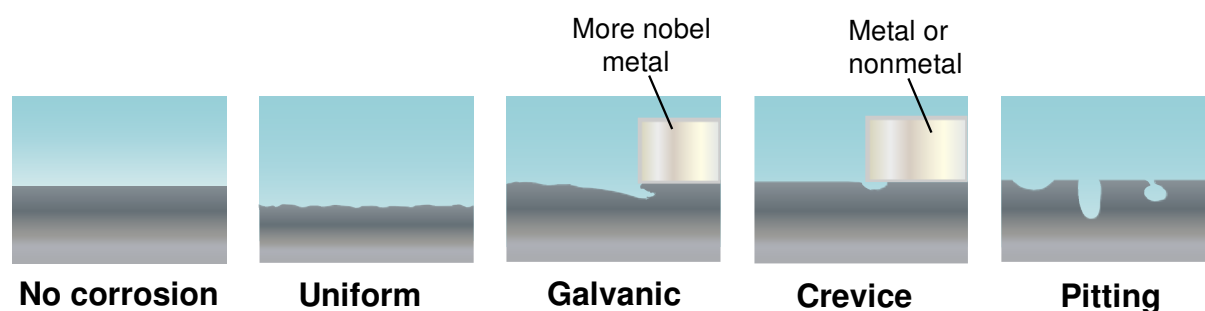

No corrosion **Uniform** **Galvanic** **Crevice** **Pitting**

Figure 1.2 Examples of common forms of corrosion.

Uniform or general corrosion is the most common type of corrosion attack, which leads to uniform dissolution or thinning of the metal over the entire exposed metal surface. However, this type of corrosion is not of great concern because it is ease to quantify and predict.

Galvanic or two-metal corrosion occurs due to a potential difference between two dissimilar metals. When the two metals are in contact, an electron flow is produced as a result of the potential difference. Consequently, the less corrosion resistant metal (the anode) corrodes faster and the corrosion of the more noble metal (the cathode) is inhibited.

Crevice corrosion occurs within shielded, confined areas (crevice) with limited exposure to the bulk electrolyte, *e.g.* under the protective coating. The environment within the crevice is poor in oxygen and more aggressive, which makes the crevice interior subject to corrosive attack. A typical example of crevice corrosion is the crevice formed between a metal surface and a protective coating.

Pitting is a highly localized, self-propagating form of corrosion that causes holes in the metal. It is one of the most vicious and destructive forms of corrosion because it is autocatalytic and can lead to sudden damage. Pitting is difficult to estimate and detect because the pits are relatively small and often covered by corrosion products. Pitting occurs when one area of the metal becomes anodic with respect to the rest of the surface. Therefore, metal alloys are extremely susceptible to pitting.
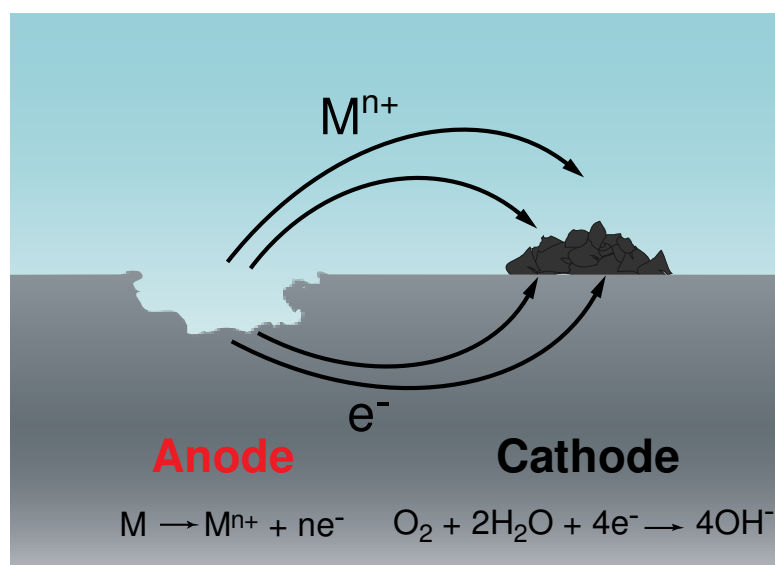

Figure 1.3 Schematic representation of an electrochemical corrosion circuit formed on corroding metal in contact with aqueous solution.

The susceptibility of metals to corrosion is given by their standard electrode potential, E^0. Metals with more negative E^0 have higher tendency to corrode compared to more noble metals with more positive E^0. In the case of "wet" corrosion, a corrosion circuit is formed when a metal comes into contact with an aqueous solution containing aggressive species like chloride ions (Figure 3). An anodic and a cathodic area are

formed on the metal surface. The area with more negative E^0 forms the anode at which the corrosion, *i.e.* the dissolution of the metal due to oxidation occurs. The anodic process leads to the formation of metal ions and electrons ($M \rightarrow M^{n+} + ne^-$). The metal ions are transported via the solution to the cathode, causing direct current flow through the corrosion circuit. The electrons generated at the anode are conducted through the metal to the cathode, where they are consumed by reduction reactions. The most frequently observed cathodic reactions are the hydrogen ion reduction ($2H_2O + 2e^- \rightarrow H_2(g) + 2OH^-$) and the oxygen reduction ($O_2 + 2H_2O + 4e^- \rightarrow 4OH^-$). The latter has a more positive standard electrode potential and is therefore more favorable to occur. With oxygen dissolved in the electrolyte, the corrosion rate is generally higher. That is because the metal oxidation rate is directly proportional to the rate of electron consumption by the reduction reactions. An effective corrosion control can be realized by removal or deactivation of one part of the corrosion circuit, *e.g.* anode or cathode. For instance, the current flow through the corrosion circuit can be decelerated by increasing the resistance of the ionic or electronic current paths. This kind of corrosion control can be achieved by removal of the electrolyte from the corrosion cell, *e.g.* by drying the metal surface.

2.3.1.1 Corrosion of aluminum alloys

Metal alloys are single- or multiphase structures resulting from mixtures of two or more metals with different characteristics. Aluminum alloys, for example, are not homogeneous, pure materials, but complex structures containing multiphases of dissimilar crystallographic structure and chemical composition. Therefore, the alloy microstructure can influence strongly its corrosion susceptibility. Normally, aluminum alloys have good resistance to general (uniform) corrosion due to their naturally formed and highly adherent protective oxide film. The thin (2 – 4 nm), passive film of amorphous Al_2O_3 is stable at pH 4 – 9 but film defects or breakdown can lead to severe pitting corrosion. For example, the ubiquitous, aggressive chloride ions can cause pits in aluminum by first adsorbing on the surface, then reacting with aluminum in the oxide layer and finally thinning the protective oxide layer locally. This localized attack leads to breakdown of the passive oxide film and exposure of the metal to the corrosive environment.[68-69]

Very low pitting corrosion resistance is exhibited by copper-containing aluminum alloys of the series AA2xxx, *e.g.* AA2024-T3. This alloy is used in structural applications, particularly in aircraft and aerospace applications due to its light weight, high mechanical strength and durability.[70] The aluminum alloy, AA2024-T3 is used as a model substrate in this work, due to its high importance for aerospace industry and low corrosion resistance.

The nominal alloying element concentrations for AA2024-T3 on a weight percentage basis are: 3.8 to 4.9 Cu, 1.2 to 1.8 Mg, 0.3 to 0.9 Mn, 0.5 Si and Fe, 0.15 Zn and Ti, 0.1 Cr and the remainder Al.[71] The microstructure of AA2024-T3 is complex, consisting of many ($\sim$ 300 000 particles/cm^2) intermetallic particles (IMPs), which vary in size (1 – 10 µm), shape and composition.[72] The main IMPs Al_2CuMg (S-phase), Al_2Cu (θ-Phase) and Al_7Cu_2Fe contain the noble metal copper and reveal, therefore, cathodic potential relative to the alloy matrix. These IMPs make up around 80 % of the total number of IMPs and function as cathodes, initiating localized (pitting) corrosion of AA2024-T3 by formation of galvanic couples with the surrounding aluminum matrix.[73]

Pitting corrosion in AA2024-T3 is a complex process of several stages (Figure 4). Corrosion initiation begins with localized corrosion attack of S-phase IMPs (Al_2CuMg) surrounded by more noble IMPs (*e.g.* Al_2Cu or Al_7Cu_2Fe).[74] Coupling of IMPs of opposite electrochemical activity increases the corrosion rate significantly. Consequently, S-phase IMPs acting as anodes are attacked first and undergo dealloying due to dissolution of Mg and Al (Figure 4a).[75] This dealloying leads to the formation of copper-enriched S-phase remnants, which are then etched out to leave a pit in the metal surface. These copper species have the tendency to electrochemically replate and redeposit on the neighboring cathodic IMPs (Figure 4b). This copper relocation increases the cathodic character of the IMPs around the pit, which in turn leads to stable pitting corrosion. This process is followed by trenching (etching) at the grain boundary of the cathodic IMPs, which is due to dissolution of aluminum from the continuous phase.[76] This phenomenon results from the oxygen reduction at the cathode and the generation of hydroxide anions, which lead to a local pH increase of up to around 10. Such high, alkaline pH values cause the instability and breakdown of the passive aluminum oxide film, resulting in dissolution of the underlying aluminum metal around the IMPs. The trenches penetrate very rapidly the metal, providing a favorable

environment for further subsurface attack (Figure 4c). Thus, the anode switches from the S-phase particles to the more anodically active base of the trenches. Eventually, the anode is driven in the subsurface attacking the grain boundary network in depth as well as laterally.[77] This process is accompanied by hydrogen gas evolution. In short, S-phase dealloying and copper redeposition are the key factors in stable pit formation and suppressing them is essential to increase the corrosion resistance of AA2024-T3. This can be accomplished by optimizing the external factors such as pH, temperature, concentration of dissolved O_2 or by using inhibiting agents. Inhibitors are widely used to suppress corrosion of aluminum alloys and an overview of the ones used for AA2024-T3 is given in the following chapter.
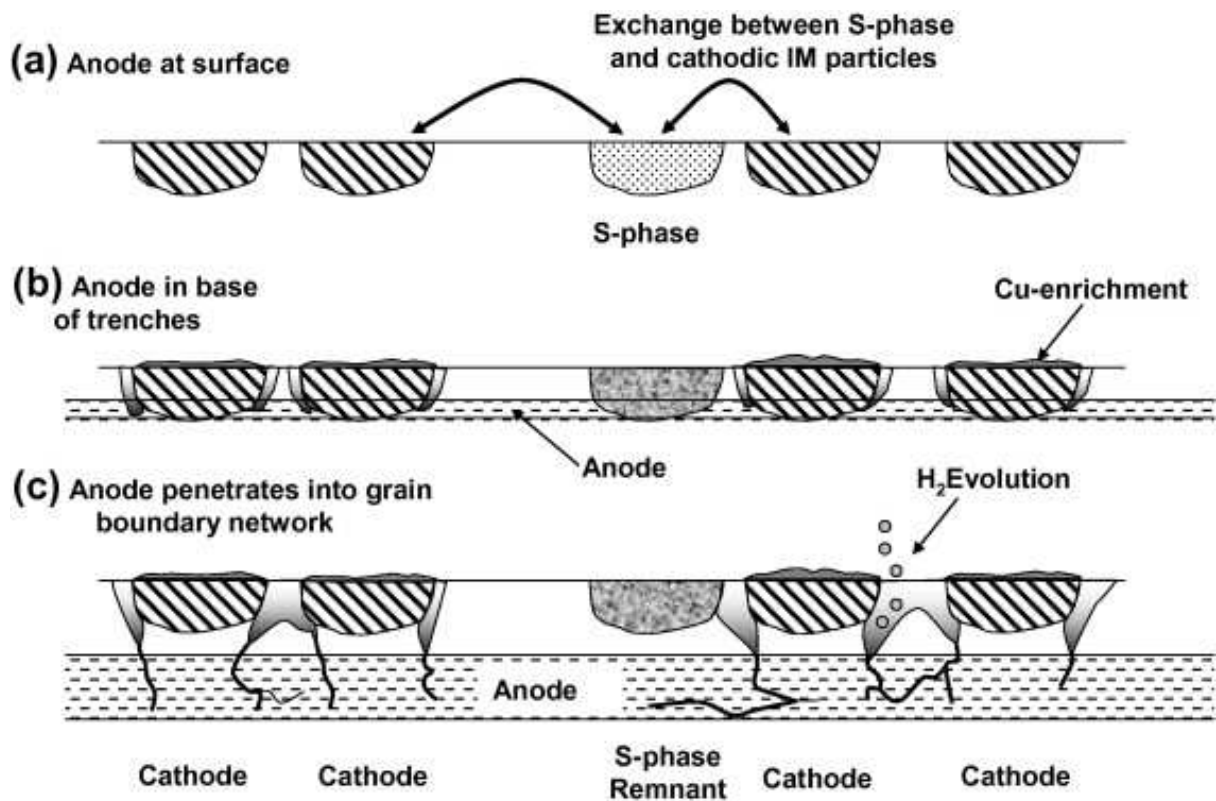

Figure 1.4 Model of pitting corrosion propagation on AA2024-T3. (a) Initiation through coupling of IMPs, (b) formation of trenches around cathodic IMPs, and (c) subsurface attack of the grain boundary network.[76]

2.3.2   Methods to prevent corrosion

2.3.2.1 Inhibitors for aluminum alloys

The principle mechanism of corrosion suppression with inhibitors is via the formation of surface complexes or impermeable layers at the metal/electrolyte interface. In practice, only substances, which prevent the access of corrosive species to the metal at low concentrations, *i.e.* lower than a few mmol/kg, are technically considered corrosion inhibitors. Inhibitors can be organic or inorganic compounds, which have sufficient solubility in the corrosive environment.

Chromates have the highest inhibition effectiveness for AA2024-T3. However, the health and environmental concerns associated with chromates, have led to very strict and international legislative restrictions concerning their use. Therefore, there is an urgent need to find new chromate-free inhibitors with reduced environmental footprint and sufficient inhibiting properties.

Various inorganic inhibitors such as molybdates, vanadates, phosphates, borates, silicates or nitrates have been extensively studied as possible chromate replacements for AA2024-T3.[78-81] These are strong oxidizing agents and function as anodic inhibitors, which retard the anodic reaction by forming a thin invisible passivating oxide film on the anodic sites. Cerium and lanthanum salts are also known to inhibit corrosion of AA2024-T3 by formation of highly insoluble deposits on IMPs and reduction of the active cathodic area.[82-83]

Many organic compounds (*e.g.* triazoles, thiazoles or quinolines) demonstrate good efficiency as anodic or cathodic inhibitors for aluminum-copper alloys. Generally, these compounds form either insoluble complexes with metal cations or impermeable films at the metal surface. Both inhibiting mechanisms lead to passivation of the metal surface. The inhibition efficiency depends on the chemical structure of the organic compound.[84] These compounds are usually amphoteric and exhibit good solubility at very high (at the cathode) or low (at the anode) pH values typical in the areas of corrosion attack. For example, 8-hydroxyquinoline (8-HQ) is an anodic inhibitor that forms insoluble aluminum complexes, which precipitate and passivate the metal surface.[85-86] The triazole and thiazole derivatives are cathodic inhibitors, which deposit at IMPs to decrease the cathodic activity.[87-88] For instance, 2-mercaptobenzothiazole (MBT) demonstrates very high (95%) inhibitor efficiency on AA2024-T3.[13] This very good

corrosion inhibition is due to the thiol group in MBT, which enables the irreversible chemisorption of MBT molecules at copper surfaces and the formation of a protective, hydrophobic monolayer. Thus, an effective deactivation of the corrosion initiation sites (IMPs) is provided. The practical application of inhibitors is realized by direct incorporation in protective coatings or encapsulation in suitable capsules, which are then dispersed in the coating matrix.

2.3.2.2 Anticorrosive coatings for aluminum alloys

The main function of anticorrosive coatings is to protect the underlying metal from corrosive attack. The various coatings acting as a protective barrier can be generally classified as metallic, organic and inorganic. In aerospace a multilayer coating system consisting of a pretreatment, primer and topcoat is typically used for aluminum alloys. The layer thickness increases with increasing distance between metal and coating layer. Thus, the pretreatment is the thinnest layer ($\sim$ 5 µm) and is positioned at the primer/metal interface. Sol-gel derived inorganic coatings have been investigated as potential replacements of chromate-based pretreatments. The sol-gel method is quite promising for preparation of protective oxide materials with good adhesion to both metal surface and organic primer. For example, sol-gel derived silane and siloxane-based coatings form covalent bonds with the aluminum surface oxide (–Al–O–Si–), giving rise to a highly adherent sol-gel layer comprised of a dense –Si–O–Si– network.[89] Unfortunately, the barrier properties of the sol-gel coatings are restricted due to their high potential to form pores and microcracks during the curing step. Thus, the penetration of corrosive species towards the metallic surface is not prevented.[90] However, the overlying primer and top-coat composed of highly cross-linked organic polymers and other additives function as a better physical barrier. Organic coatings can be generally classified as solvent- or water-borne according to the solvent used to disperse the coating components. Restrictions in the coating industry concerning the emission of volatile organic compounds have led to the preferential use of water-borne coatings. Yet, these organic coatings have worse barrier and adhesion properties in comparison to the solvent-borne ones.[91-92] The major drawback of all coating types described above is that they lose their protective function when they are damaged, *i.e.* they provide only passive protection. In contrast, anticorrosive coatings with active

protective properties protect the underlying metal from corrosion even when they are not intact. Imparting such functionality is possible by the addition of inhibitors to the coating.[93-94] The direct incorporation of inhibitors to the coating is not straightforward and has several drawbacks. For example, deterioration of the integrity and physical barrier properties of the coating can be caused.[6, 95-96] Further disadvantages are uncontrolled release, leaching and too low concentration of the inhibiting agents.[5] In order to prevent the weaknesses of this corrosion inhibition approach and preserve the active functionality of the coating, the direct contact of inhibitor species with the coating matrix should be avoided.

A promising strategy to isolate the inhibitor from the coating components is by encapsulating it in nano-/microcontainers prior to mixing with the coating formulation. This approach offers not only isolation of the inhibitor but also its homogeneous incorporation in higher amounts. Anticorrosive coatings based on inhibitor loaded containers function as feedback active systems and self-recover their anticorrosive, protective function. This is realized by releasing corrosion inhibitor in response to changes in the coating integrity (cracks) or local environment (pH shift) caused by corrosion attack. These self-healing systems have been extensively investigated because they are potential replacements of the banned chromate-based coatings. Various types of containers for inhibitor encapsulation have been reported so far. These differ in their size (nano- and microcontainers), chemical nature (organic, inorganic), shape (spheres, tubes, platelets) and structure (core-shell, porous, layered). This huge variety implies also different possible stimuli for inhibitor release (pH shift, ion exchange or mechanical rupture) resulting in numerous anticorrosive coating designs.

Anticorrosive coatings responsive to mechanical impact usually recover only the coating barrier properties and cannot actively passivate corrosion. Usually, such systems are organic coatings containing polymer capsules filled with active material (*e.g.* polymerizing or water-repelling agent).[10, 97] Crack formation due to mechanical stimuli causes the rupture of the capsules at the crack front and the consequent release of active agent that fills the crack. The encapsulation of corrosion inhibitor in polymer capsules that can be mechanically opened was also recently reported.[98-99]. For the protection of AA2024-T3, this was realized using emulsion polymerization to synthesize polyurea microcapsules containing the liquid corrosion inhibitor 2-methylbenzothiazole

(MeBT). These microcapsules were dispersed in water-borne organic primer to obtain anticorrosive coatings with enhanced active corrosion resistance.[99] However, all organic capsules, which rupture upon mechanical impact, have the disadvantage to release the encapsulated agent very fast in an uncontrollable way.

A better control over the release of inhibitor can be achieved by immobilizing inhibitor at ion-exchange pigments. In this case, the inhibitor is released in response to reactions with corrosive ions or corrosion products. An example of cation-exchange pigment is bentonite clays. The stacked negatively charged aluminosilicate layers are perfect hosts for Ce^{3+} ions, which are known to be effective cathodic inhibitors for AA2024-T3.[100-101] When incorporated in an anticorrosive coating for AA2024-T3, these cerium loaded cation-exchangers have two positive functionalities: (i) they entrap cations (Na^+ or Al^{3+}) and (ii) release Ce^{3+} ions, which react with hydroxide ions to build insoluble cerium hydroxide precipitates on the cathodic sites. As a result of this cation exchange, corrosion activity is effectively decreased.[102-103] Anion exchangers are promising structures for immobilization of anionic inhibitors, which can be exchanged with corrosive chloride ions. For example, Al-Zn layered double hydroxide compounds (*e.g.* hydrotalcite) were reported as effective anion-exchangers. Epoxy-based coatings with inhibitor loaded hydrotalcite demonstrated enhanced corrosion resistance when applied to AA2024-T3.[103] However, ion-exchange triggered nanocarriers cannot prevent the entrapped inhibitor from adversely interacting with the coating matrix.

Utilizing pH shift as stimulus for corrosion inhibitor release is the natural and the most promising approach to design anticorrosive coatings with sufficient corrosion resistance. That is because the corrosion process leads to local pH decrease in anodic areas and local pH increase in cathodic ones. Therefore, in order to sense and eliminate the negative impact of corrosion, pH sensitivity needs to be imparted to the functionalities of anticorrosive coatings.

An attractive approach to achieve this is by integrating pH sensitive inhibitor capsules in the coating. One way to form such capsules is by the layer-by-layer (LbL) assembly of oppositely charged species (*e.g.* polyelectrolytes) on templating colloidal nanoparticles. The template can be either removed to form a hollow structure or kept to provide better mechanical stability.[104-107] The advantages of this method are the variety of the charged species suitable for shell construction, the adjustable layer thickness and flexibility. The most useful feature of LbL polyelectrolyte systems is

their sensitivity to pH change, which causes switching of the capsule shell between "closed" and "open" states. Thus local changes in pH near anodic and cathodic areas can cause the opening of the capsule shell and release of the encapsulated inhibitor. For example, silica nanocontainers with 1H-benzotriazole (BTA) loaded LbL shell were dispersed in sol-gel coating and demonstrated good corrosion resistance.[108-110] However, such nanocontainers cannot prevent spontaneous leakage of the loaded inhibitor from the LbL shell into the surrounding environment. This undesired inhibitor loss is very unfavourable because LbL nanocontainers with dense silica core have anyhow low inhibitor loading capacity.

A promising approach to increase the amount of inhibitor in LbL nanocontainers is to load the inhibitor in a porous core protected by a LbL shell. This was demonstrated by loading organic inhibitors in porous metal oxide nanoparticles (TiO_2 and SiO_2) and then coating them by polyelectrolyte multilayers. These pH sensitive nanocontainers were dispersed in SiO_x/ZrO_x sol-gel coatings and improved the coating corrosion inhibition properties.[111-113] However, the complexity of such nanocontainers restricts their up-scaling and industrial application.

In contrast, the industrially mined, viable and inexpensive halloysite nanotubes have high potential as inhibitor nanocontainers. Halloysites are two-layered aluminosilicates with hollow tubular structure. Their size varies within 0.5 – 15 µm of length and 10 – 150 nm of lumen inner diameter. Halloysite nanotubes were loaded with the inhibitor, 2-mercaptobenzothiazole and covered by a LbL polyelectrolyte shell to improve the control over the inhibitor release.[7, 114-115] The sol-gel coatings doped with halloysites demonstrated very good corrosion inhibition in long-term corrosion tests. These results are due to the favourable halloysite structure, which provides good inhibitor storage in the lumen and limits spontaneous inhibitor leakage due to the small-diameter (20 – 50 nm) ends covered by the polyelectrolyte shell. Another promising approach to keep the inhibitor inside the lumen and release it in response to a pH change is by designing pH sensitive stoppers at the halloysite ends. Successful formation of stoppers for halloysites was demonstrated by exposing halloysites loaded with 1H-benzotriazole to a Cu(II) containing solution to form insoluble metal—benzotriazole complexes at the halloysite ends.[116-117] The release time was tuned by controlling the thickness of the stopper complexes. The prolonged inhibitor release time improved the long-term corrosion resistance of sol-gel coatings.

Sufficient active corrosion inhibition was also achieved by simpler design strategies. For example, BTA or 8-HQ loaded halloysites without protective shell or stoppers successfully imparted self-healing properties to sol-gel coatings.[118] The direct introduction of inhibitor loaded TiO_2 and SiO_2 nanoparticles without protective polyelectrolyte shell in organic coatings was reported to prevent spontaneous inhibitor leakage and increase the corrosion inhibition efficiency.[119-121] However, the biggest drawback of the approaches described above is the low amount of loaded inhibitor (~ 5 wt %) that limits the long-term anticorrosion performance.

This disadvantage could be overcome for organic coatings by using porous organic microcapsules formed by emulsion polymerization[99] or nanoparticle stabilized polymer nanocontainers based on Pickering emulsions.[122] The achieved loading was 45 wt % for the liquid inhibitor (MeBT) and 20 wt % for solid inhibitor (8-HQ). Unfortunately, organic micro-/nanocontainers of this type have the following significant restrictions: (i) the inhibitor can interact negatively with the containers resulting in its deactivation and (ii) the container loading efficiency is limited to the inhibitor solubility in the emulsion oil phase forming the container core and cannot be increased by further loading cycles.
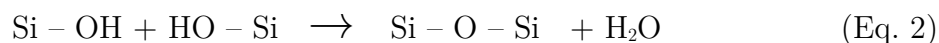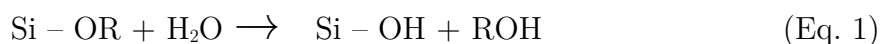
An attractive alternative to the inhibitor containers described above are mesoporous inorganic materials. For example, mesoporous silica particles (MSP) with large pore volume (~ 1 mL·g^{-1}) and surface area (~ 1000 m^2·g^{-1}), were used as nanocontainers for organic inhibitors and demonstrated two times greater inhibitor uptake than previously reported.[123-125] The incorporation of such high amount of inhibitor entrapped in mesoporous nanocontainers into sol-gel coatings improved significantly the coating corrosion resistance. This improvement was reported to be due to the enhanced passive and active functionalities of the anticorrosive coatings. On one hand, the coating barrier properties were improved by reinforcement of the coating matrix due to introduction of mechanically stable, robust silica nanoparticles. On the other hand, the large amount of encapsulated inhibitor and its controlled, local release on demand, *i.e.* upon corrosion attack, provided superior active corrosion inhibition.

Generally, employing MSP as inhibitor containers in anticorrosive coatings is very advantageous. Their chemical characteristics, low toxicity and inertness to inhibitor and coating matrix exclude any negative impact on the coating performance due to undesired interactions between the coating components (inhibitor, container and

coating matrix). Their good mechanical stability and resistance to elevated temperatures help them survive the harsh conditions to which a coating is exposed, *e.g.* high curing temperatures or crack formation. Embedding mesoporous silica nanoparticles reinforces the coating matrix not only due to the particle robustness but also due to their monodispersity, which limits particle agglomeration and favors homogeneous distribution in the coating. The various, well-established methods to synthesize porous silica particles allow easy tuning of size and morphology of both particles and pores. Thus, the incorporation of porous silica particles in coatings of different thickness (thicker than 100 nm) and chemical composition (organic and inorganic) is possible due to their controllable size and good compatibility with the coating components. In addition, the pore openings at the particle outer surface increase the roughness of the particles, which improves their adhesion to the coating matrix. Moreover, the large pore volume and high surface areas of MSP make them potential inhibitor hosts with very high loading capacity. The inhibitor loading takes place after the particle synthesis, which introduces an additional production step. However, this additional step provides control over the amount of loaded inhibitor. The complex porous system does not only provide high uptake capacity but also good storage and protection of the encapsulated inhibitor. Due to the latter property, the inhibitor is prevented from undesired, spontaneous leakage or unfavorable interaction with the coating matrix. Thus, a controlled and prolonged inhibitor release occurs in response to a local pH shift caused upon corrosion attack. Functionalizing the surface of silica particles is a possible approach to gain multifunctionality and further control over inhibitor uptake and release. In short, the characteristics of mesoporous silica nanoparticles are in favour of their successful application as inhibitor containers.

2.4 Mesoporous silica particles

According to the IUPAC nomenclature, mesoporous materials exhibit pores with diameters in the range of 2 – 50 nm.[126] For their synthesis amphiphilic molecules consisting of hydrophilic and hydrophobic parts are usually used as structure directing agents (SDAs). Typical representatives of such molecules are surfactants or block co-polymers. Surfactants are classified as anionic, cationic or non-ionic surfactants. All types of surfactants have a long hydrophobic alkyl rest and hydrophilic head group. In contrast, block co-polymers are uncharged and consist of hydrophilic A-blocks and hydrophobic B-blocks connected in supramolecular structures like ABA triblock co-polymers. Driven by their amphiphilic character, such molecules assemble themselves to form supramolecular structures or micelles in aqueous systems. By increasing the concentration of amphiphilic molecules a critical micelle concentration (cmc) is reached and different micelle structures are formed. A transformation from spherical to cylindrical and then to rod-like micelles followed by mesophases or lyotropic phases can be observed. In addition, the micelle formation and shape can be influenced by the temperature and additives (counter ions or alcohols).[126-127] The formation of these phases defines the porosity of the mesoporous silica materials. For the sol-gel synthesis of periodic mesoporous silica networks, silica precursors are added to an appropriate solution of structure directing agents (SDAs). The organic silica precursor (*e.g.* tetraethyl orthosilicate (TEOS)) undergoes first hydrolysis (Eq. 1) and then condensation (Eq. 2).

$$Si - OR + H_2O \longrightarrow \quad Si - OH + ROH \qquad\qquad (Eq.\ 1)$$

$$Si - OH + HO - Si \quad \longrightarrow \quad Si - O - Si \ + H_2O \qquad\qquad (Eq.\ 2)$$

The hydrolysis may be base or acid catalyzed and vary between minutes and days depending on the type of the precursor or SDA employed. In order to obtain silica/SDA composite structures and avoid phase separation, attractive interactions between the two components should be facilitated.[128] Therefore, in the case of base catalyzed hydrolysis, a cationic SDA is normally used.[129] That is because the silica species are negatively charged above their isoelectric point at pH = 2 and electrostatic attraction drives the adsorption of the silica species at the periphery of the positively charged surfactant micelles. In contrast, lowering the pH of the reaction mixture below

pH = 2 leads to positively charged silica species, which can assemble around anionic and non-ionic surfactants or block co-polymers due to electrostatic interactions or weak hydrogen bonds. The organization of silica species around the SDA micelles is followed by the development of a dense silica network. The silica condensation starts with the formation of oligomeric ring structures, which condense further around the template to build a 3D network.[130] Once the mesoporous material has reached a sufficient degree of condensation the SDA can be removed to acquire the desired mesoporous structure. The SDA removal can be achieved by different methods, e.g calcination or solvent extraction.[131-132]

The size and morphology of MSP and their pores can be tuned by using different templates, by varying the synthesis pH or by adding co-solvents or additives.[133] Moreover, the particle surface can be easily functionalized with various molecules in different regions of the particle.[134] Therefore, MSP are of great interest in many areas of application, including catalysis,[135] chromatography,[136] drug delivery,[137] adsorption[138] and host-guest chemistry.[139-140] These materials can be used as reactors or templates for the formation of conductive polymers or carbon nanowires in their pores.[141-143] The successful loading of substances of various sizes, shapes, and functionalities in the pores of MSP was demonstrated numerous times. For example, organic molecules, fullerenes, drugs and even very large molecules such as enzymes were immobilized in the pores of MSP.[144-146] Additionally, a controlled release of the encapsulated substance can be achieved by functionalizing the pore inner surface[147] or entrance.[148] Closing the particle pores with cleavable caps was demonstrated by pH sensitive polyelectrolyte complexes,[149] solid nanoparticles (*e.g.* CdS, Fe_3O_4),[150-151] photocontrollable coumarin derivatives[152] or proteins (*e.g.* insulin, biotin).[153-154] In short, the easy control over particle design allows for various mesoporous silica derivatives with high encapsulation capacity and stimuli-responsive release properties.

3   Materials and methods

3.1 Materials

All chemicals used were commercially available and used without further purification. Tetraethyl orthosilicate (TEOS, $\geq$ 99%), cetyltrimethylammonium chloride (CTACl, 25% in H_2O), cetyltrimethylammonium bromide (CTAB), triethanolamine (TEA) and (3-glycidyloxypropyl) trimethoxysilane (GPTMOS, $\geq$ 98%) were purchased from Sigma-Aldrich. Ethyl acetoacetate (EAA) and zirconium(IV) propoxide solution (TPOZ, 70 wt % in 1-propanol) were purchased from Alfa Aesar. Nitric acid (HNO_3, 65%) and hydrochloric acid (HCl, 37%) were supplied by Carl Roth. Sodium chloride (NaCl, analytical grade), sodium hydroxide (NaOH, 1 M), acetic acid (100%) and 2-mercaptobenzothiazole (MBT) were obtained from Merck. Ethanol (EtOH) and propan-2-ol were purchased from VWR Prolabo. Hydrogen peroxide (H_2O_2, 30 %) and buffer solutions were supplied by Fluka. Dialysis tubing (Spectra/Por 6, 50 kDa MWCO) was obtained from Spectrum. The water used in all experiments was purified in a three-stage Millipore Milli-Q Plus 185 purification system. The aluminum alloy, AA2024-T3, used for corrosion testing was supplied by EADS Deutschland and cut into appropriate dimensions for the different analyses of the anticorrosive properties. The water-based organic coating was provided by Mankiewicz GmbH. For adhesion tests, 3M two component adhesive (Scotch-Weld DP 490) was used.

3.2 Synthesis

3.2.1   Synthesis of mesoporous silica containers

Two types of mesoporous silica containers of different size were used in this work.
The first type is mesoporous silica nanocontainers (NCs), which were synthesized applying the procedure introduced by Möller *et al.*[155] A stock solution was prepared by mixing 64 mL of milli-Q water (3.55 mol), 10.5 mL of ethanol (0.179 mol), and 10.4 mL of a 25 wt % CTACl water solution (7.86 mmol). After stirring this mixture for 10 min at room temperature, 4.125 mL of TEA (0.031 mol; 1:1 TEOS/TEA ratio) were added and stirred until all TEA was dissolved resulting in a pH value around 11.

Subsequently, 20 mL of this stock solution were heated to 80 °C in an oil bath. 1.454 mL of TEOS (6.5 mmol) were added dropwise to the pre-tempered solution (within 1 – 2 min) under vigorous stirring. The mixture was refluxed at 80 °C for 2 h. A white solution developed after 10 min. Finally, the mixture was cooled to room temperature. The pH had decreased to around 9. The molar ratio of the individual components of the reaction mixture was: $TEOS/CTACl/TEA/H_2O/EtOH$ = 1:0.27:1:137:6.2. The template extraction was conducted in ethanol/HCl mixture (15 mL HCl (37%)/ 150 mL ethanol) for 30 min in ice bath under ultrasonic agitation (100 W, 35 kHz). The surfactant molecules were separated by centrifugation (49000 g, 20 min) and the solid cakes were repeatedly washed with water to obtain mesoporous silica NCs free of template.

The second type of containers is spherical hollow silica particles (SHS) with porous shell and submicron size ($\approx$ 700 nm). SHS were synthesized following a sol-gel/emulsion (oil-in-water/ethanol) approach suggested by Teng *et al.*[156] First, a 40.5 mL mixture of water and ethanol in the volume ratio of 0.59 (15 mL ethanol / 25.5 mL water) was prepared. To this mixture 0.5 mL of TEOS and 0.08 g of CTAB were added. This was followed by addition of 0.5 mL ammonia solution (25 wt % NH_3 in water) under stirring (700 rpm). The reaction mixture was stirred at this speed at room temperature for 3 hours. The white precipitate was then separated by filtration, washed with water and dried at 70 °C overnight. The surfactant molecules were removed by calcination of the dried powder in air at 550°C for 5 hours.

3.2.2   Loading of mesoporous silica containers with inhibitor

Loading of the silica containers was conducted in a second step after their synthesis. The synthesized containers were mixed with an ethanol solution of 2-mercaptobenzothiazole, MBT (20 mg mL^{-1}) and stirred for 4 hours under reduced pressure (50 mbar). The loaded containers (MBT@NCs or MBT@SHS) were separated by centrifugation, washed with water to remove excess of MBT on the container surface and dried overnight at 60 °C.

3.2.3   Release of inhibitor from mesoporous silica containers

Release of MBT from mesoporous silica containers was determined using a dialysis technique. MBT was released in buffer solutions with pH = 4, 7 and 10. In a typical release experiment 100 mg of MBT loaded containers were dispersed in 10 mL buffer solution and introduced into a dialysis tubing with a pore diameter of 6 – 8 nm (MWCO 50 kDa). The dialysis tubing was immersed in 240 mL buffer to ensure complete dissolution of the loaded MBT. The release medium and suspension in the dialysis tubing were vigorously stirred (900 rpm) at room temperature to eliminate any possible particle agglomeration and release delay due to slow diffusion of MBT from the dialysis tubing to the release medium. Aliquots of 3 mL were taken from the release medium, followed by the addition of 3 mL fresh buffer solution at different time intervals for 24 hours. Analysis of the MBT concentration in the release medium was performed with UV-VIS spectrometry in the wavelength range: 200 – 800 nm. The extinction coefficient of each buffer solution used was determined at the corresponding wavelength, for which maximum MBT absorption was detected. This enabled the comparison between the absolute released MBT amounts at different pH values.

3.2.4   Preparation of the coating matrix

The hybrid SiO_x/ZrO_x sol for the subsequent dip-coating of the aluminum alloy (AA2024-T3) substrates was prepared using a sol-gel process, as reported by Zheludkevich *et al.*[157] The zirconium oxide sol was synthesized by hydrolyzing a 70 wt % zirconium(IV) propoxide (TPOZ) solution in propan-2-ol mixed with ethylacetoacetate (EAA) (volume ratio 1:1) at pH = 0.5 (adjusted with HNO_3). The mixture was sonicated for 20 min to complex the precursor. The second organosiloxane sol was prepared by hydrolyzing (3-glycidyloxypropyl)-trimethoxysilane (GPTMS) in propan-2-ol and acidified water in a molar ratio (GPTMS/propan-2-ol/water) of 1:3:2. The formed zirconia-based sol was mixed with the organosiloxane sol in a 1:2 volume ratio under stirring. The final sol-gel mixture was placed in an ultrasonic bath for 60 min and then aged overnight at room temperature.

The water-based organic coating is a two-component, model coating developed as a primer for aerospace applications by Mankiewicz GmbH. The resin component is an epoxy based primer, which consists of synthetic resins and water. The hardener component consists of polyamines in water. The two components were mixed in a weight ratio (primer/hardener) of 0.7:1 shortly before application.

3.2.5   Embedding and coating

Prior to coating, the aluminum substrates were chemically cleaned by immersion, first in 1 M NaOH for 15 min at 60°C and then in 20 wt % nitric acid for 15 min at room temperature. Subsequently, the substrates were washed with Milli-Q water and dried with N_2 flow.
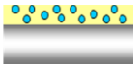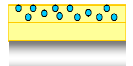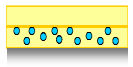
In the case of sol-gel coatings, the pretreated substrates were coated using a Bungard RDC 15 dip coater. The sol-gel films were obtained by immersing the substrate in the respective sol-gel mixture for 100 s, followed by a controlled withdrawal at a speed of 2 mm s^{-1}. After coating, the samples were cured at 130 °C for 1 h.

Using this method different sol-gel coating systems were produced, depending on the concentration and position of MBT@NCs dispersed in the coating matrix.

For **single layer sol-gel coatings**, the following concentrations of MBT@NCs in the initial sol-gel mixture before curing were investigated: 0.25, 0.5, 1, 3, 4, 5 and 10 mg mL^{-1}. The weight loss during curing of the bare sol-gel coating was experimentally determined (by weighing the coated substrates before and after curing) to be ~ 65%. The density of the wet, bare sol-gel was found by weighing a known volume to be approximately 0.9 mg mL^{-1}. Considering this, the concentrations of the MBT@NCs in the final cured coatings were calculated to be 0.04, 0.1, 0.2, 0.5, 0.7, 0.8 and 1.7 wt %.

Double layer sol-gel coatings differed in the position and concentration of MBT@NCs in the coating layers. The designs of the coating systems can be divided into: **(A)** double layer coatings with the top layer doped with MBT@NCs and **(B)** double layer coatings with the bottom layer doped with MBT@NCs. The MBT@NC concentration was varied in both coating systems and was calculated to be 0.04, 0.1, 0.2, 0.5, 0.7, 0.8 and 1.7 wt % in the final cured coating layer containing the MBT@NCs.

Table 1. Summary of the studied sol-gel coating systems.

Coating design	Description	c(MBT@NCs) in cured coating [wt %]
	one layer doped with MBT@NCs	0.04; 0.1; 0.2; 0.5; 0.7; 0.8; 1.7
	two layers, MBT@NCs in top layer	0.04; 0.1; 0.2; 0.5; 0.7; 0.8; 1.7
	two layers, MBT@NCs in bottom layer	0.04; 0.1; 0.2; 0.5; 0.7; 0.8; 1.7

Single layer organic coatings (primers) containing different concentrations of MBT@NCs or MBT@SHS were obtained by the addition of water suspensions of loaded nanocontainers to the pre-mixed two components under stirring. The amount of water used to redisperse the containers prior to mixing with the paint was only 10 wt % of the paint and had no detrimental effect on the paint formulation. The following container concentrations in respect to the cured coatings were embedded: 0.04, 0.2, 0.5, 0.7 and 1.7 wt %. The water-based organic primer was applied on AA2024-T3 plates using a spiral bar coater for 50 µm wet coating thickness. The coated samples were dried at 80 °C for 1 hour after a flash-off time of 15 min at room temperature.

3.3 Analytical methods and apparatus

3.3.1   Scanning electron microscopy

Scanning electron microscopy, SEM (Zeiss Gemini LEO 1550) was employed to analyze the structure of silica containers as well as the coated aluminum alloy substrates before and after corrosion tests. For characterization of particles, a droplet of the particle water suspension was placed on the sample holder and left to dry at atmospheric pressure and room temperature. The coated metal samples (1 x 2 cm^2) were directly glued to the carbon tab on the sample holder. All samples were sputtered with a gold/palladium mixture to avoid electron charging of the samples during SEM analysis. The samples were studied using an operating voltage of 3 kV and different magnifications. SEM and energy-dispersive X-ray spectroscopy (EDX) were used to examine the surface morphology and elemental composition of polished aluminum alloy (AA2024-T3) plates and coated AA2024-T3 after corrosion tests. EDX analysis was performed using a scanning electron microscope (Zeiss DSM 940, Germany) coupled with EDX ISIS, SiLi-Detector, Oxford.

3.3.2   Transmission electron microscopy

Transmission electron microscopy, TEM (Zeiss EM 912 Omega) was used to characterize the morphology, size and porous character of the synthesized silica containers. The sample in form of water suspension was pipetted on a coated copper grid and dried before TEM investigation. Thin slices of the synthesized silica containers were obtained by embedding the silica powders in an epoxy matrix and cutting it with a microtome. The samples were investigated with an accelerating voltage of 120 kV.

3.3.3   UV-Vis spectroscopy

UV-Vis spectroscopy was used to detect the MBT concentration during release studies. A 8453 UV-Visible spectrophotometer, Agilent Technologies was used to detect

absorbance spectra in the wavelength region 200 – 800 nm. MBT solutions were measured in a quartz cuvette with 1 cm path length.

3.3.4   Dynamic light scattering and ζ-potential

Dynamic light scattering, DLS (Malvern ZetaSizer Nano ZS) was used to evaluate the size distribution and monodispersity of the synthesized silica containers. Prior to the measurements, the slightly turbid silica suspensions were redispersed with ultrasonic agitation (100 W, 35 kHz). Typically, each sample was measured three times in backscattering mode at a detector position of 173°. The results of every measurement of 15 runs were averaged and further analyzed with the CONTIN model.

To study the pH dependence of the ζ-potential of silica containers, silica suspensions with different pH values were prepared with diluted HCl and NaOH. All measurements of the electrophoretic mobility were conducted in a DTS 1060C cell and the data were recorded in auto mode using the Smoluchowski method.

3.3.5   TGA

Thermogravimetric analysis (NETZSCH TG 209 F1) was used to detect the amount of loaded inhibitor in dried mesoporous silica containers. This was achieved by determining the weight change of a solid sample exposed to temperature increase from 25 °C to 1000 °C with a heating rate of $10 \, °C \cdot min^{-1}$. The mass loss of a sample (m ~ 10 mg) in a flow of $25 \, mL \cdot min^{-1}$ of oxygen was detected.

3.3.6   Small-angle X-ray scattering

Small-angle X-ray scattering (SAXS) measurements were conducted with dried, empty and MBT loaded silica containers, to investigate the pore structure and composition. SAXS profiles were recorded under vacuum on a Nanostar instrument (Bruker AXS, Karlsruhe, Germany) using Cu-Kα radiation with a wavelength of $\lambda = 0.154$ nm. A single photon counting area detector (HiStar, Bruker AXS) was used at a sample-detector distance of 25 and 105 cm and a range of scattering vector q from 0.1 to 7.5

nm^{-1} was covered. The powder samples were filled into borosilicate capillaries (d = 1 mm) and then sealed. Prior to the measurements, the positions of SAXS profile accumulation for each sample were determined in a nanography by mapping the weakening of the scattering intensity of the used standard substance (glassy carbon).

3.3.7   Nitrogen sorption

The pore structure and surface area of the silica containers were characterized with N_2 adsorption/desorption measurements. The measurements were performed on a Micromeritics TriStar 3000 at -196 °C. Prior to the measurements the powder samples were baked under vacuum at 25 °C for 24 hours. The surface area and pore size distribution were obtained from the N_2 isotherms by applying the BET (Brunauer-Emmett-Teller) theory and the NLDFT (non-local density functional theory) equilibrium model for cylindrical pores, respectively.

3.3.8   Coating thickness

The coating thickness was measured with a coating thickness gauge, Surfix® Pro S, from PHYNIX, Germany, using the Eddy-current principle.[158] Electromagnetic induction was used to create a circulating (Eddy) current in the conducting aluminum substrate. Changes in the current flows induced by different coating thicknesses were detected using a coating thickness probe, FN1.5, attached to a stand and used in a non-ferrous (FN) measuring mode.

3.3.9   Adhesion testing

The adhesion of freshly cured coatings to the Al-alloy substrates was measured following the standard test method, ASTM D4541. Self-aligning aluminum pull-stubs with a flat circular surface with diameter of 20 mm were glued to the coating surface with a two component adhesive and pulled off at a speed of 0.2 MPa s^{-1} using an electronically controlled hydraulic pump (PosiTest® AT-A, DeFelsko) to detach the coating from the metal surface.

3.3.10 Machu test

The Machu test is an accelerated corrosion test, which is part of the specifications to obtain the QUALICOAT quality label for coatings on aluminum and aluminum alloy.[159] Prior to the test, a cross-cut incision (3 x 3 cm²) with a width of 1 mm was introduced on coated aluminum panels with a scratch tool according to Sikkens to cut the coating down to the metal. The uncoated parts of the panels were isolated with adhesive tape. The test solution was a mixture of sodium chloride (50 g L⁻¹), 100 % acetic acid (10 mL L⁻¹) and 30 % hydrogen peroxide (5 mL L⁻¹) in water. The pH of the test solution was 3.0 – 3.3. The coated samples were immersed in the solution, the vials sealed and heated to 37 °C for 48 hours. After 24 hours, 5 mL L⁻¹ of hydrogen peroxide (30 %) were added. The pH of the test solution was also adjusted to 3.0 – 3.3 with glacial acetic acid, if needed. After the test, the area with the cross-cut was scratched and the area with removed coating around the scratch was examined. The result of the Machu test is satisfactory when no infiltration exceeding 0.5 mm on both sides of the scratch is observed. Photographs of the coated samples were taken before and after scratching over the cross-cut on the coated samples.

3.3.11 Scanning vibrating electrode technique

The active anticorrosive properties of the coated samples (1 x 2 cm²) were investigated in 0.1 M NaCl solution using the scanning vibrating electrode technique (SVET, Applicable Electronics). Prior to immersion in the NaCl solution, a controlled, straight scratch was made in the coating with a scalpel blade (Bayha blade No. 22) attached to a lever applying a controlled force. The scratch was deep enough to ensure exposure of the metal surface to the NaCl solution. The coated samples were then sealed with adhesive tape (Tesa, clear, 60 μm thickness) and only an area of 3 x 3 mm² containing the scratch was left uncovered for exposure to the NaCl solution.
SVET provided an in-situ characterization of the corrosion process, which induces an electrostatic potential gradient inside the electrolyte solution leading to an alternating current signal. This is based on the development of anodic and cathodic sites on the substrate surface induced by redox reactions during the corrosion process. The vertical current density was recorded with the help of a vibrating PtIr-electrode. The vibrating

Pt-blackened electrode tip with a diameter of 20 µm was moved at 300 µm above the substrate on a lattice of 21 × 21 points over an area of 3 × 3 mm² (lateral step size: 150 µm). The vibration amplitude was 40 µm with a frequency of 864 Hz. The analyzed sample area was scanned within ca. 5 min and the scans were repeated every 15 min during the 12 h immersion period. After each scan, an optical image was taken automatically by the camera, which is part of the SVET set-up. The subsequent analysis of the SVET data was performed with the help of homemade software to obtain information about the current densities over the scanned area for each scan. The latter can be plotted as a 3D current density map on which a positive peak growing with time can be observed (Figure 3.1).
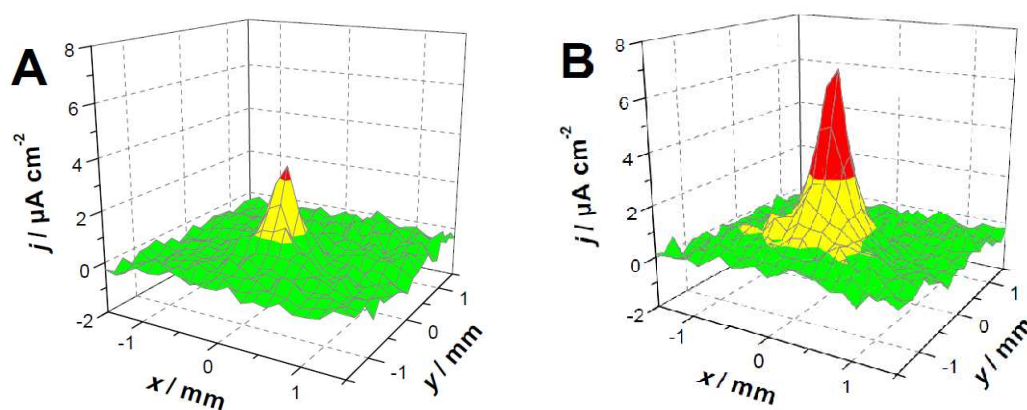
Figure **3.1** Exemplary 3D current density maps obtained after a) 1 h and b) 12 h in a typical SVET measurement.

This peak represents the measured anodic current density generated by electrochemical reactions occurring at the anode, which is localized and stable during corrosion of the studied aluminum alloy. In contrast, the cathode is delocalized and poorly pronounced, which makes it difficult to detect. Therefore, the cathodic current, which does not describe directly the metal oxidation, was not considered in the further analysis of the SVET data. The further evaluation of the current density maps included their integration in order to find the maximum current density for every scan. This was calculated as current assuming that a constant electrical current I_0 flows through the defect in the coating for each complete scan. This is a reasonable approximation given that each scan took only 5 min to complete. Based on this and a current flow only in a

hemisphere, the radial component of the current density, j_r is dependent on the distance r from the current source, as shown in equation 1.[160-161]

$$j_r(r) = \frac{I_0}{2\pi r^2} \tag{1}$$

From this the z-component of the current density, j_z at a height z above the metal surface can be derived as shown in equation 2:

$$j_r(r) = j_r \frac{z}{r} = \frac{I_0 z}{2\pi r^3} \tag{2}$$

3.3.12 Electrochemical impedance spectroscopy

Electrochemical impedance spectroscopy (EIS) was employed to study the barrier properties of the intact coatings. Electrochemical impedance reflects the ability of the studied coatings to resist the flow of electric current and is measured by applying an AC potential to the coated sample and detecting the current flowing through it. The applied small excitation potential, *V(t)* is a sinusoidal wave that as a function of frequency and time has the form:

$$V(t) = V_0 \sin(\omega t) \tag{3}$$

in which *Vo* is the potential amplitude and ω the radial frequency. The system pseudo-linear response to this small excitation signal is a phase shifted oscillating current signal, *I(t)* :

$$I(t) = I_0 \sin(\omega t + \phi) \tag{4}$$

in which I_0 is the current signal amplitude and ϕ the phase shift between the two signals.

Using an expression analogous to Ohm's Law, the magnitude of impedance can be calculated as a function of frequency and phase shift:

$$Z = \frac{V(t)}{I(t)} = \frac{V_0 \sin(\omega t)}{I_0 \sin(\omega t + \phi)} \tag{5}$$

Impedance can be also represented as a vector with length |Z|, which dealt as a complex number consists of a real (Z') and an imaginary (Z") part:

$$|Z| = \sqrt{ZZ^*} = \sqrt{(Z')^2 + (Z'')^2} \quad \text{with } Z = Z' + jZ'' \tag{6}$$

The relationship between the complex impedance and the phase angle can be shown clearly in phasor diagrams and expressed as:

$$\tan\phi = \frac{z''}{z'} \tag{7}$$

Thus, impedance is related to three quantities (phase angle, real and imaginary impedance), which can be measured as a function of frequency in a wide frequency range covering about 10 orders of magnitude. Experimental impedance spectra can be represented as Bode and Nyquist plots. In Nyquist plots, real impedance Z' is plotted vs. imaginary impedance Z". Bode plots represent the phase angle ϕ and the logarithm of the impedance modulus |Z| as a function of the frequency of the applied potential. Bode plots are the preferred display of EIS data because they reveal the minima and maxima of ϕ. The latter are described as time constants and their positions at certain frequencies are sensitive indicators of system properties and their changes with changing experimental conditions.

In a typical EIS experiment, the coated substrates (6×3 cm^2) were placed into home-made cells, whereby a truncated area of 3 cm^2 of the sample was exposed to 1 M NaCl solution at room temperature, which approximately mimics oceanic salinity. A three-electrode set-up was used with impedance spectra being recorded at the open circuit potential. A reference (saturated calomel) and a counter (platinum) electrode were immersed in the cell. The coating at the edge of each sample was removed and the metal substrate, functioning as the working electrode, was connected to the potentiostat. The cell was placed in a Faraday cage and measurements were performed using a CompactStat electrochemical analyzer (Ivium Technologies). The current response was detected in the frequency range 100 kHz to 0.01 Hz at a constant potential (1 V). Six frequencies were typically assessed per decade. The amplitude of the sinusoidal voltage signal was 10 mV. The spectra were obtained and fitted using the software Ivium Soft (release 1.985) and Zview.

4   Results and discussions

4.1 Mesoporous silica containers

In the following section the synthesized two types of mesoporous silica particles are characterized. Their properties and applicability as containers for corrosion inhibitors are described and compared.

4.1.1   Characterization of mesoporous silica containers

Mesoporous silica nanocontainers (NCs) are the first type of containers used in this work. These were synthesized by using CTACl as a template and TEOS as silica precursor.[155] The reproducibility and upscaling of the synthesis have been already verified.[162] Spherical hollow silica particles (SHS) are the second type of investigated containers. SHS were prepared following a sol-gel/emulsion (oil-in-water/ethanol) approach, in which TEOS was used as template and CTAB as stabilizing agent.[156]

The synthesized NCs and SHS are in form of a white stable colloidal water suspension or white powders, respectively. The particle size distribution and colloidal stability at different pH values were investigated by means of dynamic light scattering measurements (Figure 4.1). The ζ-potential and Z-average diameter of the synthesized containers at different pH values were measured because electrostatic repulsion between particles in solution influences strongly their colloidal stability and agglomeration tendency.
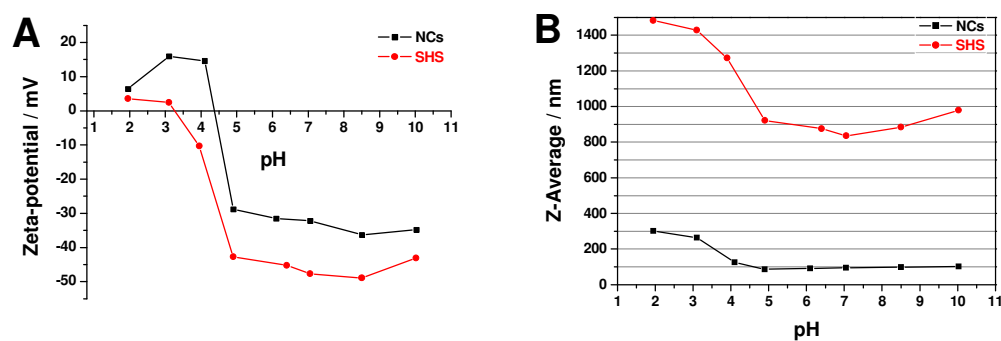
Figure 4.1 Dynamic light scattering results for mesoporous silica nanocontainers (NCs) and spherical hollow silica containers (SHS) showing their a) Zeta-potential and b) Z-average dependence on pH.

The synthesized silica containers possess a zero surface charge at their isoelectric point (IEP), which is at pH ≈ 4.5 for NCs and at pH ≈ 3 for SHS (Figure 4.1a). This difference can be explained by the different synthesis approaches used to remove the templating surfactant molecules. In the case of SHS, the surfactants were completely removed by calcination and the measured IEP occurs at a lower pH, which is close to the one (pH ≈ 2) reported in the literature for silica particles.[163] The more positive charge on the NCs is likely to be due to residual CTACl molecules, which assemble on the silica surface triggered by electrostatic forces. The positively charged heads of the cationic surfactant molecules (CTACl) are attracted by the negatively charged surface of the silica particles and form a layer or bilayer at the particle surface. This leads to the overall more positive ζ-potential of the NCs. Increasing the pH above the IEP leads to negative ζ-potential values for both NCs and SHS, which are in the order of -35 mV and -45 mV, respectively. Positive ζ-potential values were measured in the acidic pH region. At pH extremes (pH = 2 or 10) kinks in the ζ-potential curve were observed. This is due to the addition of too much acid or base to adjust the pH, which can cause shearing of the slipping plane and affect the measured ζ-potential values.

The results shown for the Z-average diameters are calculated using the CONTIN model and include the hydrosolvation shell around the particles (Figure 4.1b). The derived polydispersity indices (PdI) for the NCs (0.1 – 0.3) are smaller than the ones for the SHS (0.6 – 1.0), indicating better colloidal stability of the NCs. The higher PdI of the SHS suggests the presence of intergrown particles and agglomerates. Due to better electrostatic stabilization in the pH range above the IEP, both NCs and SHS are better dispersed and exhibit Z-average diameters ≈ 100 nm and ≈ 900 nm, respectively. Thus, the SHS size is almost one order of magnitude bigger than the NC size. An increase of the measured Z-average diameters and PdI is observed below the IEP, suggesting that the particles exhibit higher agglomeration tendency, when positively charged.

The investigation of the synthesized silica containers with electron microscopy (SEM and TEM) confirms the monodispersity of the samples (Figure 4.2 and 4.3). Both container types exhibit spherical shape and rough surfaces. The NCs preserved their spherical shape after the ultracentrifugation and sonication steps during the purification procedure, which suggests their good structural stability (Figure 4.2).
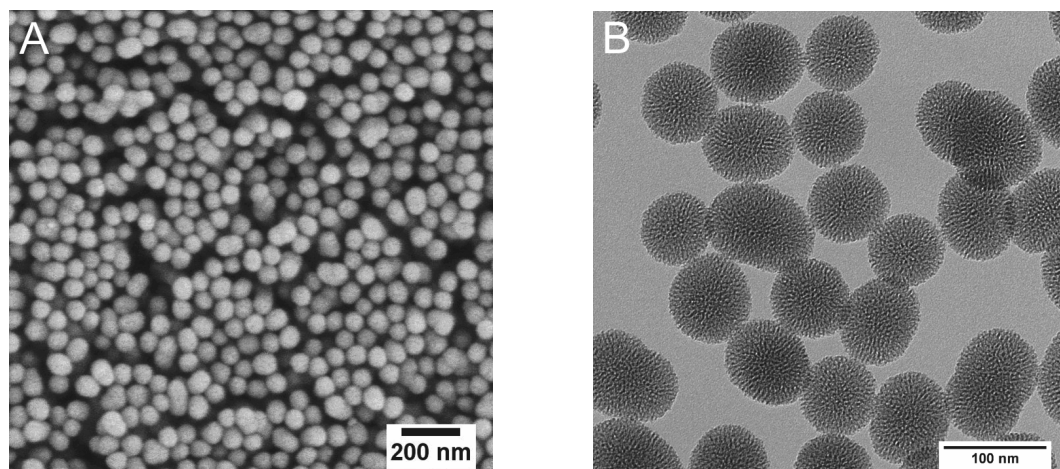
Figure 4.2 a) SEM and b) TEM micrographs of mesoporous silica nanocontainers (NCs).

The TEM micrographs of the NCs reveal a well-developed pore structure (Figure 4.2b). In all NCs, the cylindrical pores are open, not ordered and oriented from the centre to the outer surface, building a complex, worm-like pore system. The NC diameters are in the range between 60 and 80 nm, which favors their incorporation in micrometer thick coatings.

The bigger size (600 – 700 nm) of the second type of containers (SHS) is revealed by the SEM and TEM micrographs shown in Figure 4.3. Generally, the synthesized SHS are very monodisperse. However, some intergrown particles can be observed in the SEM micrograph (Figure 4.3a), which explains the measured higher PdI in comparison to NCs. The particle intergrowing is due to the emulsion synthesis route or sintering during calcination. In this the silica precursor forms small templating droplets in the continuous water/ethanol phase and their attempt to coalesce leads to the formation of particles which adhere to each other. The inter-particle bonding is easy to break as indicated by the existence of some fractured particles with imperfect spherical shape. The TEM analysis of microtomed SHS reveals their core-shell porous character (Figure 4.3b). The shell is around 100 nm thick with worm-like mesopores ordered in short range parallel to each other. The core is more porous in character with disordered cage-like, round pores with diameters on the order of 25 nm (Figure 4.4).
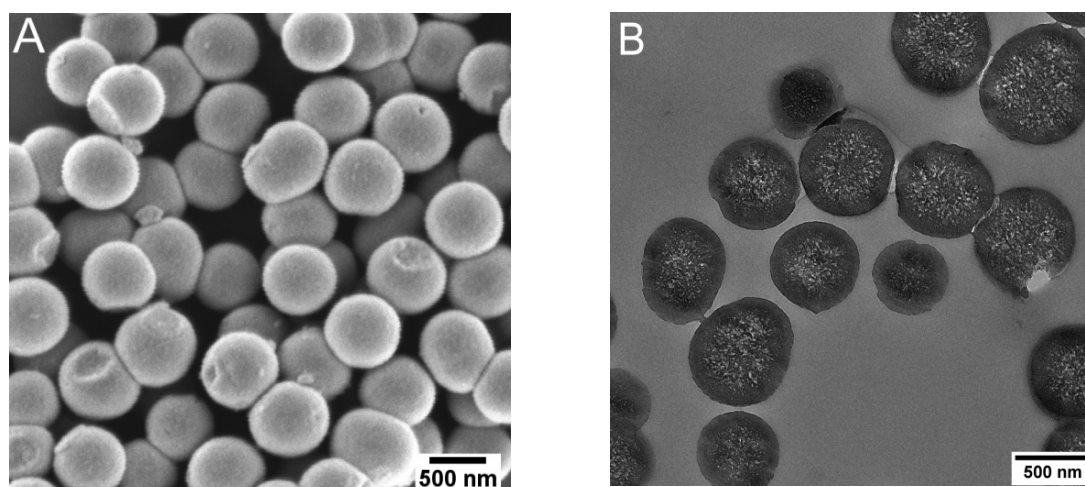
Figure 4.3 a) SEM and b) TEM micrographs of spherical hollow silica containers (SHS).
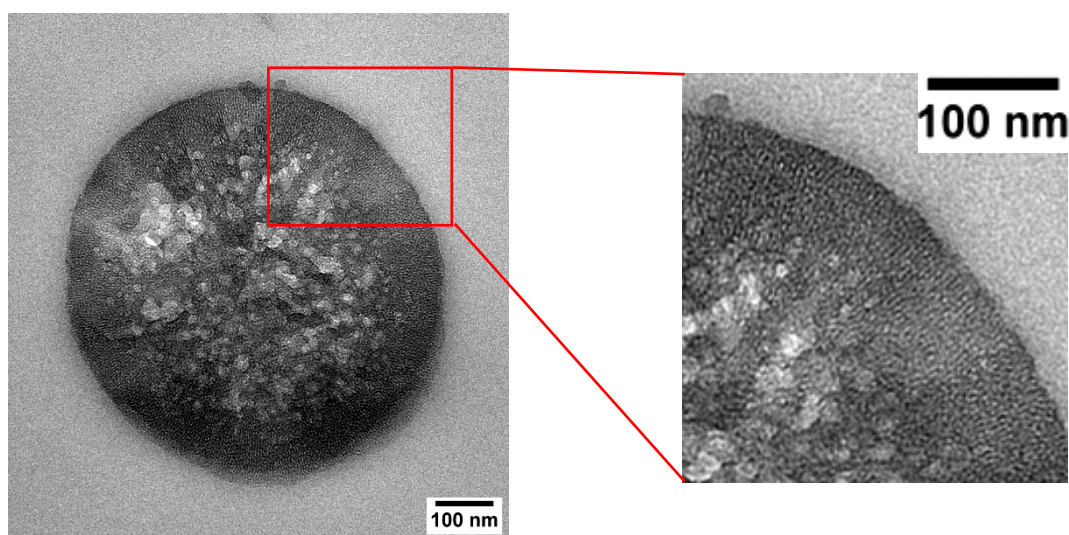

Figure 4.4 High magnification TEM image revealing the pore structure of microtomed SHS.

The porosity of the silica containers was further evaluated with N_2 sorption measurements. The adsorption-desorption behavior of N_2 in the NCs delivered a type IV isotherm with two closed hysteresis loops typical for mesoporous structures (Figure 4.5a). At low relative pressure, monolayer adsorption takes place. This is followed by multilayer adsorption and a strong increase in the adsorption at $p/p_0 = 0.2$ indicating the filling of the mesopores by capillary condensation. The second noticeable increase in the adsorbed volume occurs at relative pressures above 0.8. The hysteresis loop is caused by interparticular pores present due to the nanometer-sized particles and by

pore blocking or cavitation effects.[164] The total surface area determined with the BET model is ≈ 1000 m^2 g^{-1}, making the NCs promising hosts for the adsorption of guest molecules. The NLDFT model for cylindrical pores considering the adsorption branch yields a cumulative pore volume of ≈ 1.2 mL g^{-1} and a narrow pore size distribution with a distinct peak having a maximum at 4 nm (Figure 4.5b).
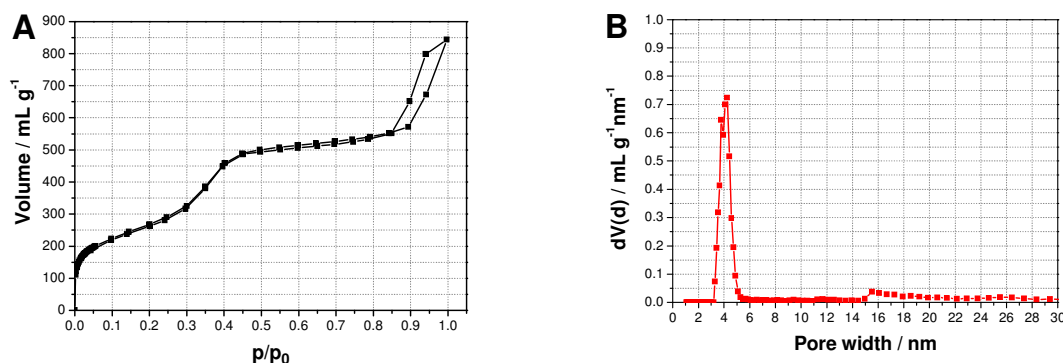
Figure 4.5 N$_2$ sorption a) isotherm and b) pore size distribution of mesoporous silica nanocontainers (NCs).

The N$_2$ sorption isotherms obtained for the spherical hollow silica containers (SHS) are also of type IV and display a distinct hysteresis loop of type H2 in the p/p$_0$ range 0.4 – 1.0 (Figure 4.6).[165] This is an indication of the presence of wide bodied pores with narrow necks (*i.e.* in-bottle or cage-like pores). As revealed by the TEM analysis of SHS (Figure 4.4) the container core consists of bigger cage-like pores and the shell contains smaller cylindrical mesopores. Thus, the H2 hysteresis loop, which is typical for silica particles synthesized by the emulsion method,[166] can be assigned to the porosity of the SHS core. The hysteresis loop closes at p/p$_0 \approx 0.45$, indicating pore blocking during N$_2$ desorption caused by the narrow openings of the wider pores in the SHS core. Despite the different morphology of the studied containers, the surface area of the SHS is similar to the NCs one and also ≈ 1000 m^2 g^{-1}. The pore size distribution curve of the SHS obtained using the NLDFT model for cylindrical pores and the adsorption branch reveals one sharp peak, again indicating a narrow pore size distribution with average pore width of ≈ 3 nm (Figure 4.6b). These mesopores represent the porosity of the SHS shell as observed with TEM. The pore volume of the SHS was calculated to be ≈ 0.8 mL g^{-1}, which classifies the SHS as containers with high loading capacity.
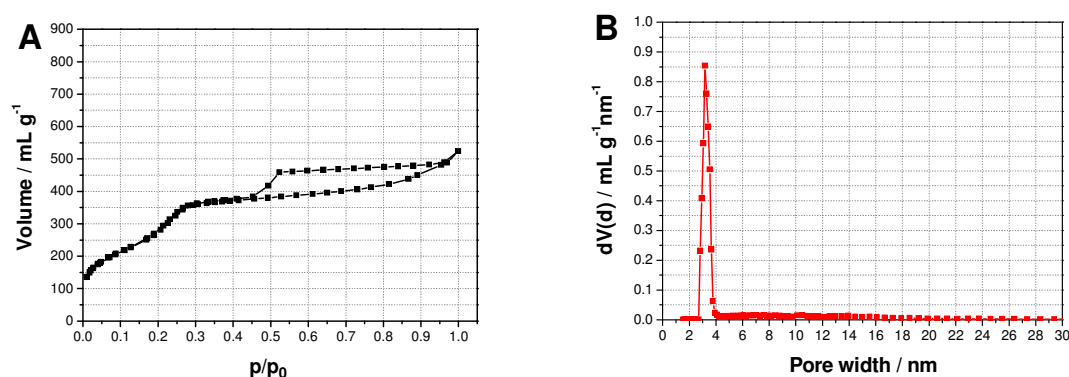
Figure 4.6 N_2 sorption a) isotherm and b) pore size distribution of spherical hollow silica containers (SHS).

Dried NCs and SHS powders were measured with TGA in order to characterize their temperature stability and residual mass of surfactant (Figure 4.7). The weight loss under 100 °C corresponds to the decomposition of water in the samples. In the temperature region 200 – 400 °C a small change in weight of $\approx$ 2 wt % and $\approx$ 1 wt % for the NCs and SHS, respectively was observed. This indicates the successful removal of the templating surfactant molecules. The further weight decrease ($\approx$ 5 and 2 wt % for NCs and SHS, respectively) at T > 400 °C can be due to dehydroxylation of silanol groups at elevated temperatures or an instrument error. The NCs and SHS demonstrated good temperature stability for 25 °C < T > 1000 °C.
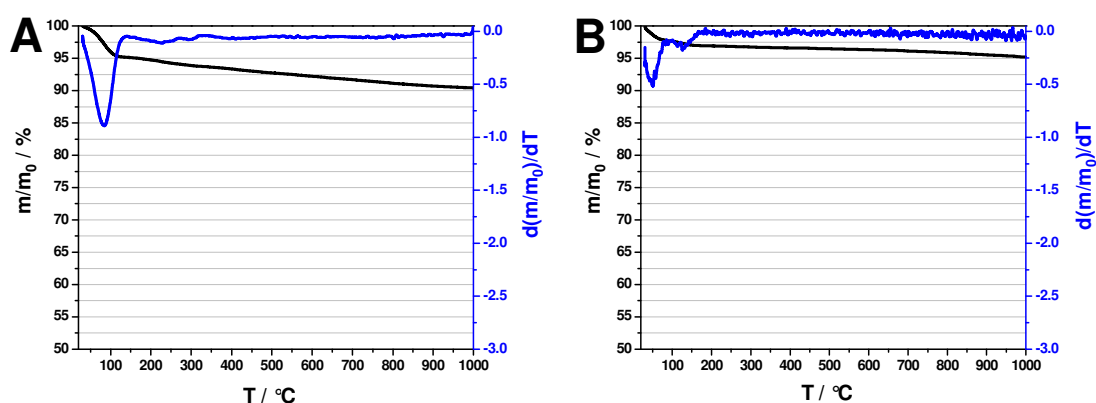
Figure 4.7 TGA results showing the weight loss of a) NCs and b) SHS as a function of temperature.

4.1.2   Inhibitor loading

The big pore volume and surface area of the synthesized silica containers suggest a high loading capacity. In addition, the complex pore system and container structural stability favors good inhibitor storage. The adsorption of the inhibitor, 2-mercaptobenzothiazole (MBT), at the silica containers was conducted in ethanol under reduced pressure (50 mbar). This technique has previously been found to be beneficial in increasing the loading efficiency.[137, 167-168] The corrosion inhibitor 1H-benzotriazole (BTA), which has a similar structure and size as MBT (Figure 4.8) has been already successfully loaded in the mesoporous silica nanocontainers (NCs) used in this work.[123] Using a similar loading approach, a BTA loading of 409 mg (BTA)/1 g (SiO$_2$) was calculated based on N$_2$ sorption measurements and the decreased total pore volume of the loaded NCs. This inhibitor loading is two times higher compared to the inhibitor loading results already reported in the literature for comparable nanocontainers.[113, 118] The feasibility of the reported value for BTA loading was assessed by calculating a theoretical maximum loading capacity using the total pore volume (≈ 1.2 mL g^{-1}) of the empty NCs. Assuming that only the pores are filled with BTA molecules with ρ_{BTA} = 1.36 g mL^{-1} and V$_m$ = 87.6 mL mol^{-1}, maximum 1.53 g BTA can be incorporated in the total pore volume of 1 g NCs. Thus, the maximum theoretical loading capacity of the NCs when loaded with BTA is ≈ 60 wt %. The achieved experimental loading, which is around one third of the maximum one, is considered reasonable. The maximum theoretical loading capacity of the NCs and SHS was calculated also for MBT with ρ_{MBT} = 1.42 g mL^{-1} and V$_m$ = 118 mL mol^{-1}. Accordingly, 1 g NCs or SHS can contain a maximum of 1.7 g or 1.1 g MBT, respectively. This equals to a MBT maximum loading capacity of 63 wt % for the NCs and 52 wt % for the SHS.
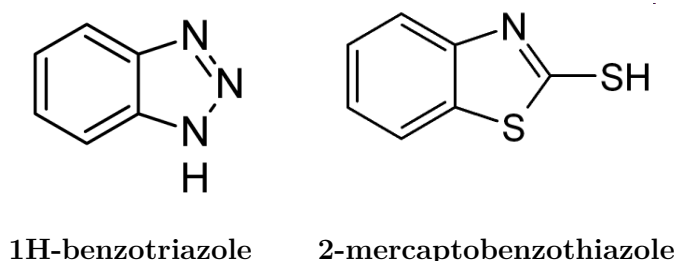

1H-benzotriazole   **2-mercaptobenzothiazole**

Figure 4.8 Structural formulas of the corrosion inhibitors 1H-benzotriazole (BTA) and 2-mercaptobenzothiazole (MBT).

The experimental MBT loading was quantitatively evaluated with TGA measurements. First, the temperature stability of pure MBT powder was studied and the decomposition temperature of MBT was determined to be 288 °C (Figure 4.9).

The thermogravimetric analysis of the silica containers (NCs and SHS) containing MBT (MBT@NCs and MBT@SHS, respectively) showed a distinct weight loss at temperatures around the decomposition temperature of MBT (Figure 4.10). As shown in Figure 4.6 the weight loss of empty silica containers in this temperature region is negligible. Thus, the 20 % mass loss at T ≈ 288 °C measured for both MBT@NCs and MBT@SHS can be attributed mainly to the decomposition of MBT. The experimentally determined amount of loaded MBT is less than half of the calculated maximum loading capacity of the containers. Accordingly, the incorporated MBT amount can fill less than half of the total pore volume of the empty NCs and SHS. Therefore, the achieved experimental loading is acceptable and a further increase in loading should be feasible.
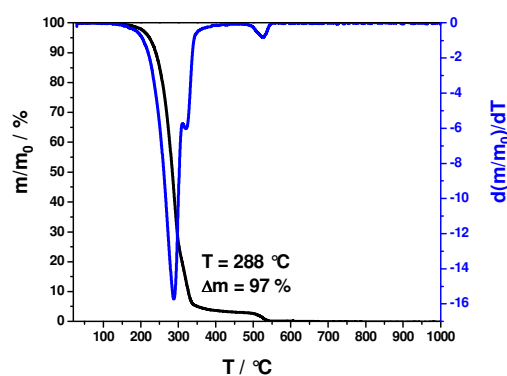
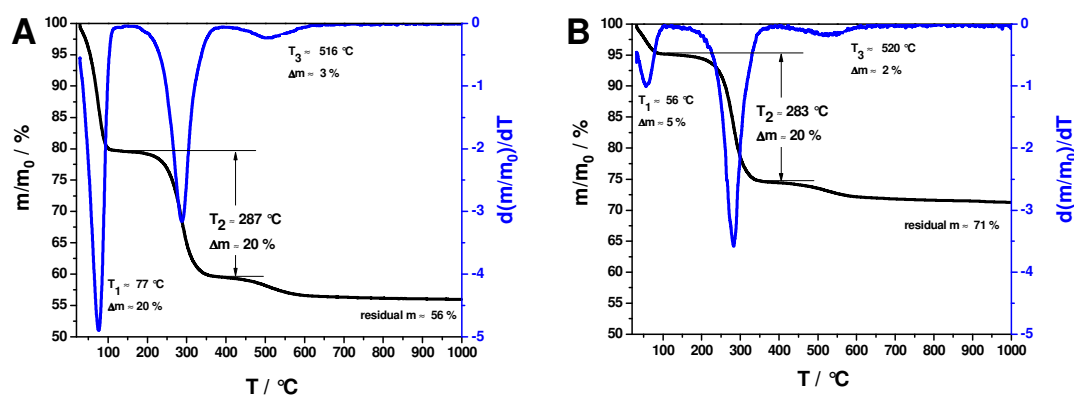**Figure 4.9** TGA results showing the mass loss and decomposition temperature of pure MBT.

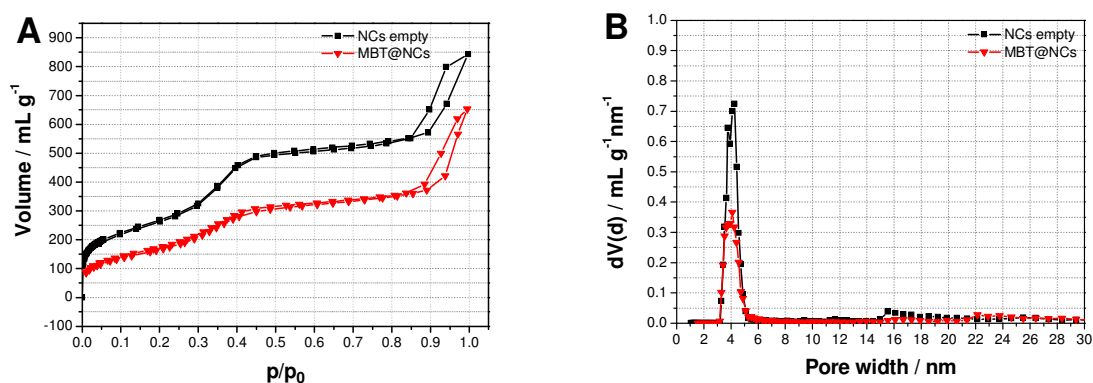**Figure 4.10** TGA results showing the mass loss of MBT loaded a) NCs and b) SHS

Figure 4.11 N_2 sorption a) isotherm and b) pore size distribution of empty and MBT loaded mesoporous silica nanocontainers (NCs and MBT@NCs, respectively).

In order to determine, whether the loaded MBT is incorporated in the pores, N_2 sorption measurements of the MBT@NCs and MBT@SHS dried powders were conducted. It was found that the incorporated MBT molecules change the porosity and surface area characteristics of the silica containers (Figure 4.11 and 4.12). A reduction in the total pore volume and surface area is observed for both MBT@NCs and MBT@SHS

For MBT@NCs, the pore volume corresponding to pores with an average diameter of 4 nm, which contribute the most to the calculated pore volume, is reduced by factor of two after adsorption of the inhibitor molecules (Figure 4.11b). This suggests that the pores are filled with MBT. Using the difference between the total pore volume of empty and loaded NCs, a MBT loading of ≈ 18 wt % can be calculated. This loading value is in agreement with the loading determined with TGA. The MBT amount needed to completely fill the pore volume (≈ 0.7 mL g^{-1}) comprised by pores with widths less than 10 nm is 0.7 g, which corresponds to a loading of ≈ 41 wt %. Thus, it is feasible that the available 0.2 g MBT in 1 g MBT@NCs is stored in the mesopores of the NCs.

The N_2 sorption measurements of MBT@SHS also revealed a decrease in BET surface area and total pore volume (Figure 4.12), suggesting that the presence of inhibitor influences the adsorption behavior of N_2 molecules. The reduction in total pore volume is due to the decreased contribution of both pore types in the SHS (Figure 4.12b).
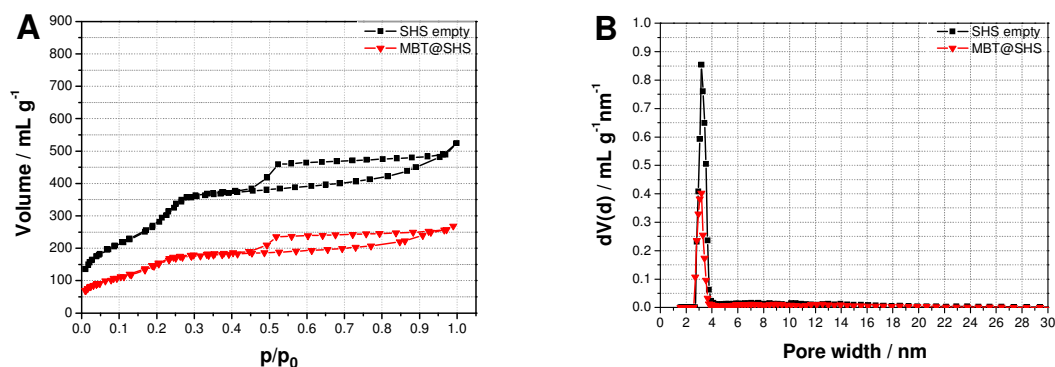
Figure 4.12 N_2 sorption a) isotherm and b) pore size distribution of empty and MBT loaded spherical hollow silica containers (SHS and MBT@SHS, respectively).

After an exact evaluation of the change in volume contributed by each pore type, a reduction factor of approximately two was determined for both pore types. Therefore, it can be suggested that the MBT is incorporated in both the mesopores of the SHS shell and the wider cage-like pores of the SHS core. The volume comprised by the pores with diameters less than 10 nm is ≈ 0.4 mL g^{-1}, in which the threefold of the present amount of 0.2 g MBT (as calculated with TGA) can be incorporated. Based on the N_2 sorption results, a MBT loading of ≈ 30 wt % was calculated for MBT@SHS. This value is higher than the one detected with TGA (≈ 20 wt %). One possible explanation for this can be some residual MBT between the SHS, which contributes to the total weight of the sample used for N_2 sorption measurements and reduces the measured total pore volume and surface area. Furthermore, a possible rearrangement of the MBT molecules during outgassing of the sample prior to N_2 sorption measurements can lead to the adsorption of MBT at the SHS outer surface and pore blocking.

In order to confirm the successful loading of the NCs and SHS pores with MBT, the difference in absolute scattering intensity of loaded and empty silica containers was investigated with SAXS (Figure 4.14). Since X-rays are scattered by electrons, the scattering strength depends on the composition of the investigated material. For this reason, the scattering length density ρ_{sld}, which is among others proportional to the electron density of the material, its molar mass and mass density, directly influences the scattering contrast. Therefore, the scattered intensity, which can be directly measured, relates to the Fourier transform of the scattering length density distribution

in the sample.[169-170] Figure 4.13 shows a comparison of the scattering length densities (ρ_{sld}) of the materials present in the studied samples. It is revealed that the addition of organic or air to the silica reduces the scattering length density.
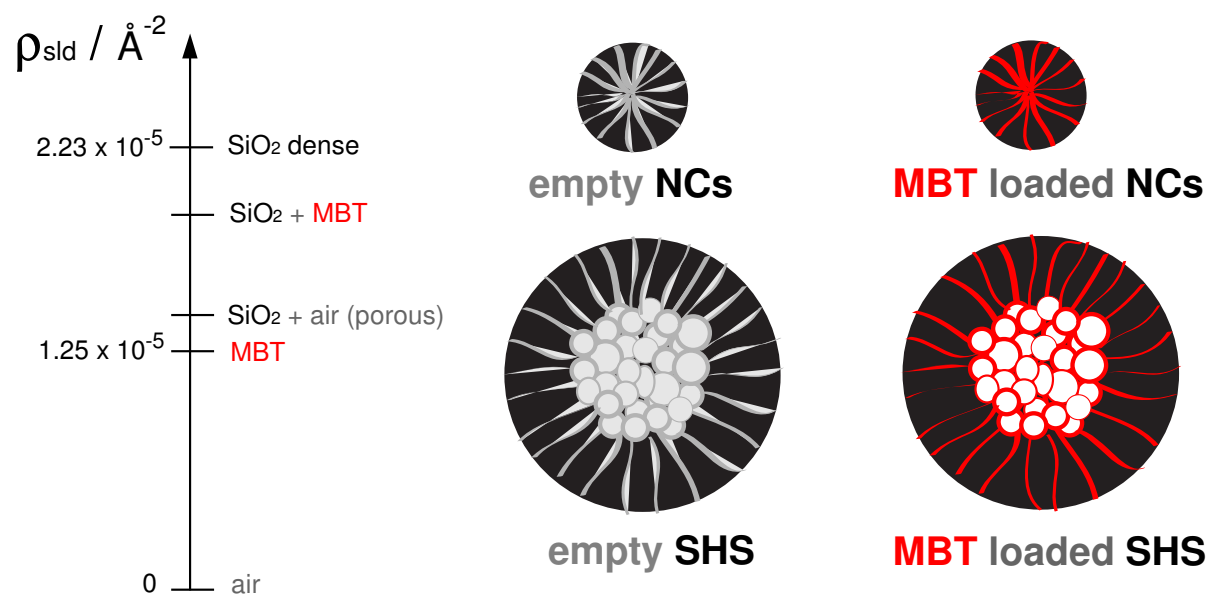

Figure 4.13 Scattering length densities (ρ_{sld}) of the materials present in the samples studied with SAXS and a graphical representation of the empty and MBT loaded silica containers.

The SAXS patterns for empty and MBT loaded NCs were measured only at a detector distance of 105 cm, which explains the smaller q range of the represented data (Figure 4.14a). This q range was big enough to obtain the needed information about the sample. For the NCs only one peak with a maximum at q ≈ 1.3 nm^{-1} was observed which can be attributed to the scattering of the mesopores (Figure 4.14a).[171] This peak is more intense for the empty NCs than for the MBT@NCs. In the case of empty NCs the scattering contrast is due to the difference between scattering length densities (ρ_{sld}) of silica and air in the pores. A drop in scattering intensity for the mesopores can be caused by filling of the pores with the organic inhibitor MBT, which has a higher ρ_{sld} than air (Figure 4.13).[172] Thus, the smaller difference between ρ_{sld}(MBT) and ρ_{sld}(SiO$_2$ dense) causes a decrease in intensity in this q region. Small q values correspond to large scattering distances. These can be calculated with d = 2π/q, so q = 0.1 nm^{-1} corresponds to a distance of order 60 nm, which is comparable with the size of the

studied NCs. Therefore, in the low q range, the detected scattering is caused by the NCs and is strongly influenced by the particle composition and its scattering contrast to the surrounding.[173-174] When the scattering in contrast to the air between the particles is detected, the MBT loaded NCs have a higher scattering due to their higher ρ_{sld} compared to that of empty or air-filled NCs.

The SAXS measurements of empty and MBT loaded SHS were conducted at both detector distances (25 and 105 cm) to cover a q range of 0.1 nm^{-1} – 8 nm^{-1} (Figure 4.14b). In the SAXS patterns three regions, corresponding to different scattering distances are observed. Starting from low q, these are caused by the scattering of (i) the SHS particles, (ii) the cage-like pores ($d_{pore} \approx 25$ nm) in the SHS core and (iii) the mesopores of the SHS shell.

Thus, the two peaks at q > 1 nm^{-1} probably correspond to the mesopores in the SHS shell and represent the scattering contrast between the silica matrix of the SHS shell and pore interior of the mesopores in the SHS shell. For MBT loaded SHS, the scattering intensity is slightly lower than for empty SHS. This result is due to the weaker scattering contrast when the mesopores of the shell are filled with MBT compared to the case, when they are empty (*i.e.* filled with air). In the intermediate region of the SAXS patterns (0.2 nm^{-1} < q < 1 nm^{-1}), the scattering contrast reveals the difference between the ρ_{sld} values of the interior of the cage-like pores in the SHS core and the matrix (*i.e.* the SHS mesoporous shell) surrounding it. Accordingly, when the pores in the SHS core are empty and the mesopores in the SHS shell are filled with MBT, the difference between $\rho_{sld}(air)$ and $\rho_{sld}(SiO_2 + MBT)$ causes the scattering intensity. This was detected to be higher for MBT@SHS than for empty SHS, because the $\rho_{sld}(SiO_2 + air)$ is smaller than $\rho_{sld}(SiO_2 + MBT)$. This result supports the assumption that the MBT is contained in the mesopores of the SHS shell. The scattering signal at q < 0.2 nm^{-1} represents the scattering contrast between SHS outer surface and air between the particles. Thus, the measured higher scattering intensity for MBT@SHS at low q indicates the presence of MBT adsorbed at the container outer surface and shell.
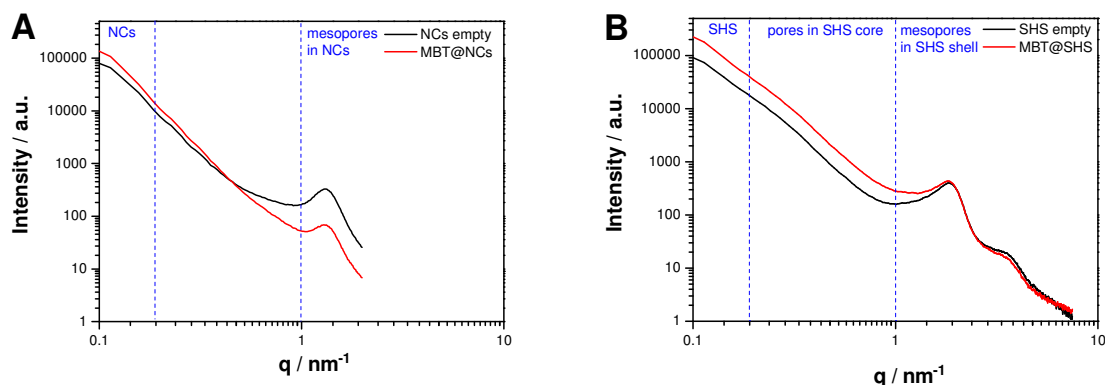
Figure 4.14 SAXS patterns of empty and MBT loaded a) NCs and b) SHS.

The results obtained from the combination of three analytical techniques (TGA, N_2 sorption and SAXS) suggest that the incorporation of MBT in the studied silica containers was successful. It is assumed that after deaeration of the pores due to the reduced pressure, the highly concentrated inhibitor solution enters the particles pores without hindrance. This assumption is supported by the fact that the size of the inhibitor molecules (< 1 nm) is less than 1/3 of the diameter of the silica container pores. It should be noted that the silica containers presented in this work possess much better encapsulating and storage properties than previously reported, similar containers. This makes the studied containers applicable wherever high uptake and controlled delivery of encapsulated molecules are required.

4.1.3   Inhibitor release

The release of the MBT from the MBT@NCs and MBT@SHS was determined using a dialysis technique at pH = 4, 7 and 10. The chosen acidic and basic pH values are typically achieved during the corrosion of aluminum alloys and can be utilized as triggers for inhibitor release. The amount of released MBT was monitored with UV-Vis spectrometry for 24 hours.

The profiles obtained at different pH values are similar in shape for both MBT@NCs and MBT@SHS and reveal two stages of inhibitor release (Figure 4.15). An initial fast release is followed by a more gradual release. In the first stage a high amount of MBT is released within the first hours. This initial burst release is pH-dependent and

particularly important as it describes the amount of inhibitor available on contact with a corrosive solution. The MBT release in alkaline conditions for both container types is faster than for acidic and neutral conditions. In addition, the amount of released MBT is the largest at pH 10. As corroding AA2024-T3 areas have high basicity at the cathode, the larger release at pH = 10 is desirable. On the other hand, the reduced release at pH = 7 should limit the leeching of inhibitor from the coating. The second stage of the release profiles is characterized by a gradual MBT release reaching a saturation level. From the comparison of the results for MBT@NCs and MBT@SHS, it is evident that the MBT release from the SHS is slower. This can be due to the longer mesopores in the SHS shell ($\approx$ 100 nm) compared to the ones of NCs ($\approx$ 40 nm). A prolonged release is of great advantage for long-term corrosion inhibition. The stabilization in MBT release for longer immersion times can be due to reaching a maximum MBT solubility in the release medium and MBT degradation.[175] The maximum released amount of MBT differs with pH because of the pH dependent solubility of MBT.[176-177]

The release study revealed a stimuli-responsive (pH) MBT release from the silica containers.
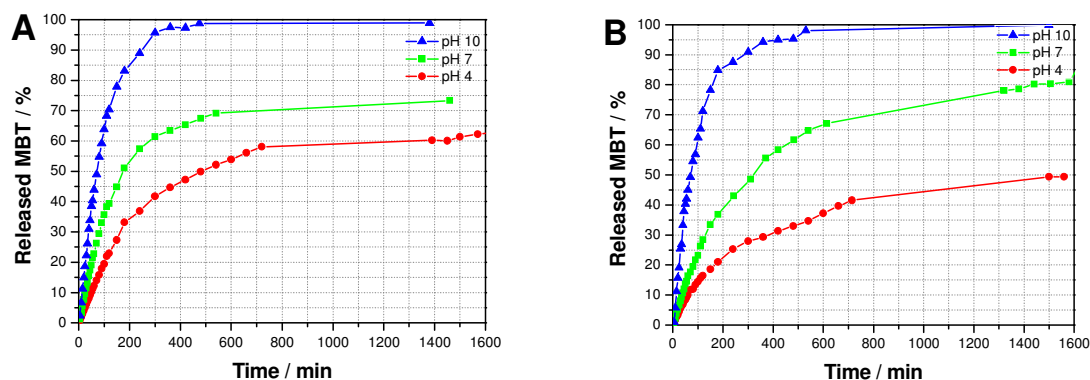

Figure 4.15 Profiles of release of MBT from a) MBT@NCs and b) MBT@SHS obtained during dialysis at different pH values and measured with UV-Vis spectroscopy.

4.2 Active anticorrosive coatings with embedded nanocontainers

In this work, the aluminum alloy AA2024-T3, which is widely applied in aerospace industry, was used as a model substrate. Its high tendency to pitting corrosion makes the development of efficient anticorrosive coatings for it a challenging task. Typically, in air-craft industry, a multilayer coating system consisting of a pretreatment, primer and topcoat is used for AA2024-T3. Standard anticorrosive coatings operate as a physical barrier between the metal and the corrosive environment and provide passive protection only when intact. In contrast, active protection prevents or slows down corrosion even when the main barrier is damaged. The most effective active corrosion inhibition of aluminum alloys is provided by conventional chromate conversion coatings.[178,179] However, their toxicity and worldwide restriction creates an urgent need for finding effective corrosion preventing alternatives without the negative environmental impact of chromate. [2-3, 180]

In this work an effective, active anticorrosive coating system for AA2024-T3 is developed and optimized. The protective coatings were prepared by dispersing mesoporous silica containers, loaded with the nontoxic corrosion inhibitor 2-mercaptobenzothiazole, in a passive sol-gel (SiO_x/ZrO_x) or organic water-based layer (Chapter 3.2.4 and 3.2.5). The choice of the mesoporous silica containers described in Chapter 4.1 is based on their good compatibility with the used coating matrix and their high capacity for inhibitor storage. The selected model inhibitor was the nontoxic 2-mercaptobenzothiazole (MBT), which is reported to be an effective corrosion inhibitor for the studied aluminum alloy, AA2024-T3.[13]

4.2.1   Influence of nanocontainer concentration

Several parameters (nanocontainer concentration, position and size) of the design of the studied active anticorrosive coatings were varied and their influence on the anticorrosion efficiency was investigated. An optimum corrosion inhibition can be obtained only after fulfilling certain technical requirements: (i) homogeneous dispersion of the embedded containers; (ii) good adhesion and compatibility of the containers and the coating matrix; and (iii) sufficient concentration of corrosion inhibitor. All these requirements are governed by the concentration of the embedded containers. This, on one hand, should be as high as possible to provide sufficient inhibitor for active protection. On the other hand, a high container amount may deteriorate the barrier properties. Therefore, studying the complex dependence of coating performance on NC concentration is of great significance, especially considering the scarce reports on it.

4.2.1.1 Physical properties of the coatings

The metal substrate (aluminum alloy AA2024-T3) was coated with a single layer of hybrid inorganic sol-gel (SiO_x/ZrO_x) doped with MBT@NCs using the dip-coating technique. The following concentrations of MBT@NCs, dispersed homogeneously in the final cured coatings, were studied: 0, 0.04, 0.1, 0.2, 0.5, 0.7, 0.8 and 1.7 wt %. These concentrations were chosen in order to preserve the integrity of the coating and to demonstrate that low concentrations of embedded NCs with high inhibitor loading offer sufficient passive and active corrosion resistance. The MBT@NCs were successfully dispersed in the sol-gel precursor solution and no precipitation of MBT@NCs was observed during the dip-coating of the metal plates. The thickness of the obtained coatings was measured on the AA2024-T3 surface with a coating thickness gauge using the Eddy-current principle.[158] The measured thicknesses of the different coating systems were in the range of 4 µm to 5 µm (Figure 4.16). The measurement accuracy is strongly influenced by the high roughness of the metal substrate as well as the low thickness of the coatings.

The dry adhesion of the freshly cured coatings was determined using a pull-off test according to the standard method, ASTM D4541. An aluminum pull-stub with a diameter of 20 mm was first glued to the coating and then pulled off to remove the coating from the metal substrate.
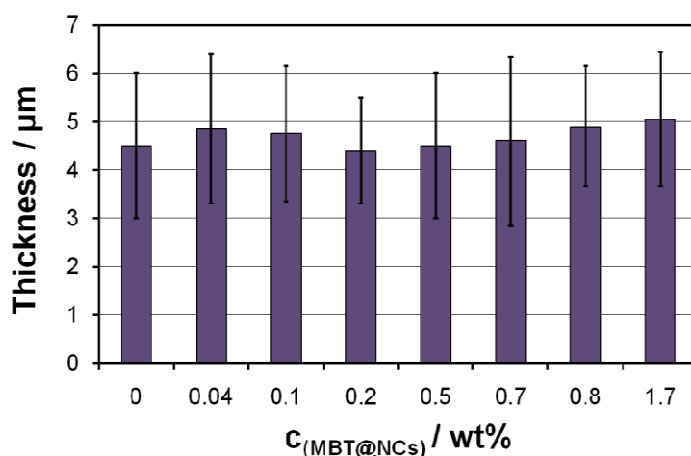
Figure 4.16 Measured coating thicknesses of the cured single layer coatings containing different concentrations of MBT@NCs.

The pull-off force needed for detachment is divided by the test area to express adhesion as tensile stress. The results obtained for coatings with and without MBT@NCs are comparable, and are in the narrow range of 2 – 3 MPa (Figure 4.17).[181-183] This finding means that incorporating MBT@NCs in the sol-gel matrix does not deteriorate the adhesion between the coating and the metal substrate. Furthermore, the adhesion results are an indication for the good stability of the coatings with and without MBT@NCs. However, no well defined correlation between adhesion and MBT@NC concentration could be determined.
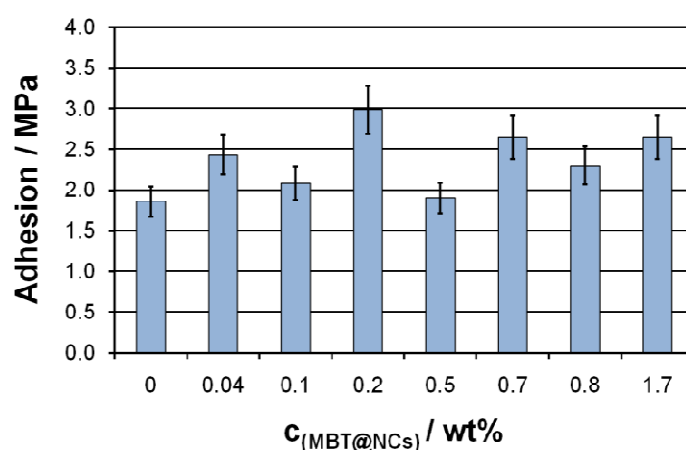

Figure 4.17 Measured adhesion of freshly cured single layer coatings containing different concentrations of MBT@NCs to the metal substrate (AA2024-T3).

The surface of the cured, bare sol-gel film was investigated with scanning electron microscopy, which revealed that nanocracks developed in the passive sol-gel matrix after curing (Figure 4.18). This characteristic may have a negative impact on the barrier properties of the sol-gel coating.
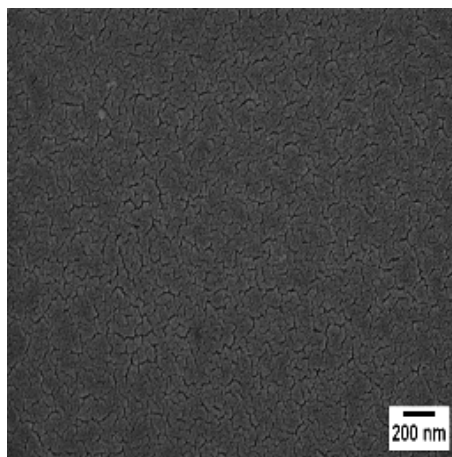

Figure 4.18 SEM micrograph showing the surface of a bare sol-gel film without MBT@NCs dip-coated on a metal substrate (AA2024-T3).

4.2.1.2 Anticorrosive properties of the coatings

4.2.1.2.1 Active corrosion resistance

The active anticorrosive properties of the fabricated coating systems were evaluated in-situ with the scanning vibrating electrode technique (SVET). This technique is ideal for the investigation of the coating performance on the aluminum alloy used in this work. That is because of its high susceptibility to localized corrosion, attributable to its intermetallic particles (IMPs) building galvanic couples with the surrounding matrix. An example of intermetallic particles are S-phase ($CuMgAl_2$) particles, which constitute ~ 60% of the IMPs.[184] Figure 4.19 reveals the distribution, morphology and composition of IMPs on a polished, uncoated AA2024-T3 plate. The IMPs are present as micrometer sized grains dispersed within the whole aluminum matrix. Their composition was studied with EDX mapping and the different elements were color labeled. Thus, Mg (yellow), Mn (green) and Cu (red) were detected to comprise the IMPs.
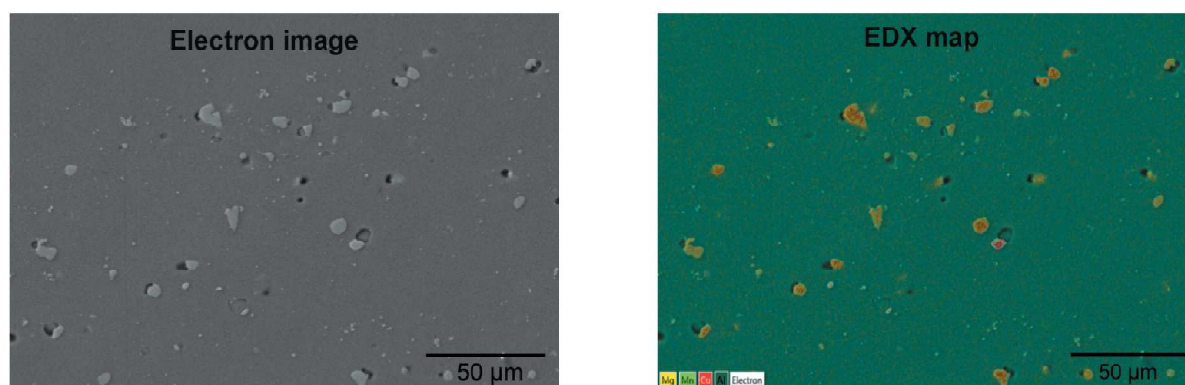
Figure 4.19 SEM-EDX analysis of a polished and uncoated metal substrate (AA2024-T3) showing the intermetallic particles and their composition.

These Cu and Cu-containing phases act as cathodes in the AA2024-T3 alloy, making the aluminum phase the anodic attack site. Thus, upon initiation of corrosion, a positive anodic and a negative cathodic current flow can be detected. Employing SVET, the electric field around a corrosion site is converted into an alternating voltage on the vibrating electrode tip, from which the current density can be calculated. As a result, the measured current density over an area can be plotted as a 3D current density map.[160, 179, 185-187] By indicating the minimum and maximum current densities over the scanned area, a second plot can be drawn showing the change in current density with time.

In this study, the coated samples were scratched in a controlled way (see Chapter 3.3.12) in order to accelerate the corrosion process and evaluate their active anticorrosive properties. In all samples, an anodic activity was measured above the scratch, which can be assigned to excess Al^{3+} ions produced by the oxidation and dissolution of the aluminum alloy. In the 3D maps, this process is expressed as a single positive peak with a constant position during the measurement, indicating that the anode is one defined pitting site (Figure 4.20). In contrast, no localized cathode was detected. Therefore, the poorly pronounced cathodic current that does not describe directly the metal oxidation was not shown.[188]
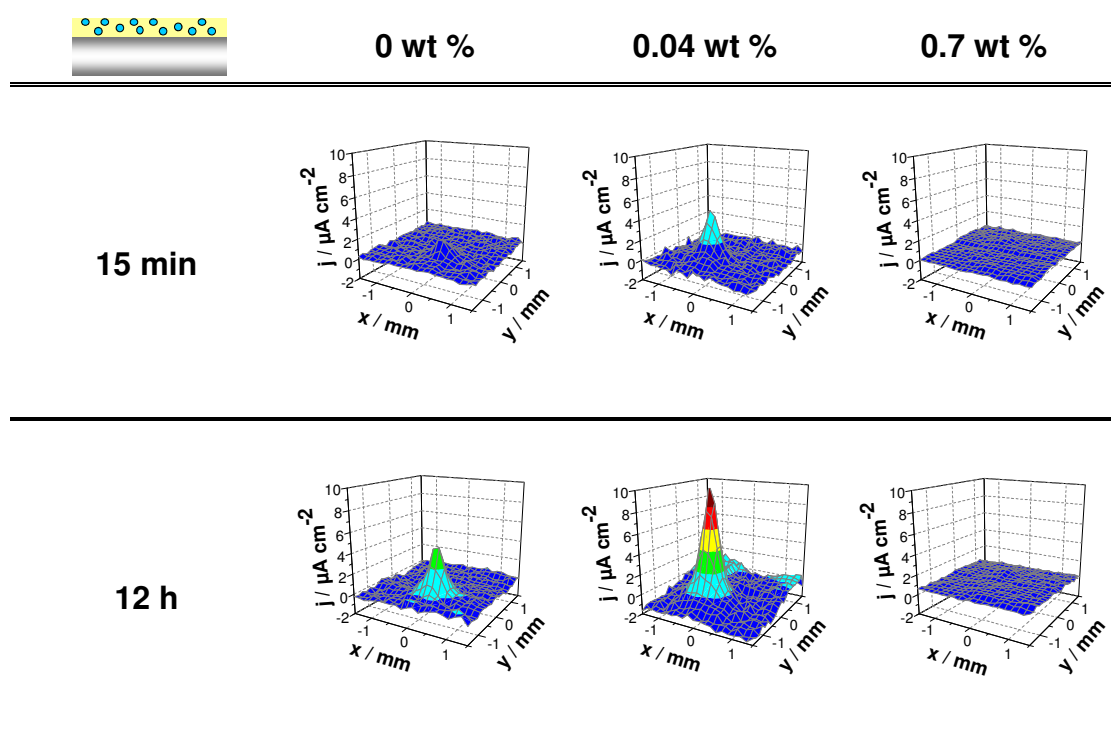
Figure 4.20 SVET 3D current density maps of AA2024-T3 substrates coated with single layer sol-gel coatings containing MBT@NC at different concentrations (0, 0.04 and 0.7 wt %). The results shown are examples for coated samples with detected high (for 0.04 wt %) and low (for 0.7 wt %) anodic current densities, in comparison to the control sample without MBT@NCs, after 15 minutes and 12 hours immersion in 0.1 M NaCl.

The cathodic reaction generates OH$^-$ ions, thereby increasing the local pH in the corroded area. These conditions are favourable for the dissolution of the inhibitor (MBT) molecules[176] adsorbed on the embedded NCs. Accordingly, at the onset of corrosion, the inhibitor molecules are released and diffuse to the metal surface to form a protective layer preventing the direct contact of chloride anions with aluminum and its oxidation to Al^{3+}. As a consequence, an increase of the anodic current density with time can be assessed as a failure of the coating sample to inhibit corrosion evolution. In contrast, suppression of anodic activity is defined as self-healing. Therefore, the coatings inhibiting the corrosion processes in the scratched area are evaluated as being successful in active corrosion prevention. The maximum anodic currents detected as a function of time are represented in Figure 4.21.
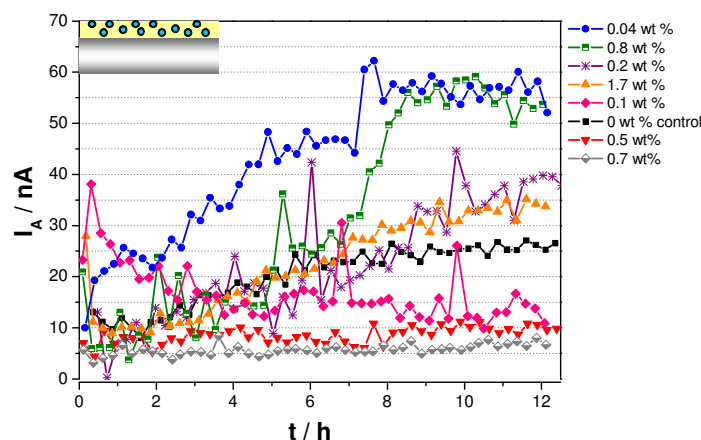
Figure 4.21 Maximum anodic currents detected with SVET over the scanned scratched area during a 12 hour immersion period in 0.1 M NaCl. Results for samples coated with a single sol-gel layer containing different MBT@NC concentrations are shown.

A distinct corrosion propagation expressed by the high values of anodic current, I_A (> 30 nA) can be seen for samples with too high (0.8 - 1.7 wt %) and too low (0.04 - 0.2 wt %) MBT@NC concentrations. These samples reach anodic current values above that of the passive control system, suggesting poor active corrosion inhibition due to an insufficient inhibitor quantity in the case of low MBT@NC concentrations. The coatings with too high MBT@NC concentrations possess poor anticorrosive properties because of a possible deterioration of the passive layer due to more microdefects in the area neighboring the scratch, which are introduced by the higher amount of embedded NCs. Thus, based on the SVET study, a concentration window in which the corrosion process was inhibited successfully was determined to be between 0.5 and 0.7 wt %. The SVET results are supported by the SEM micrographs depicting the scratched area after completion of the SVET tests. The high anodic activity detected by SVET for the control sample originates from an extensive corrosion attack. This is revealed by the formation and accumulation of a large amount of corrosion products covering the scratch in the sol-gel coating (Figure 4.22a). In addition, degradation of the integrity of the coating surrounding the scratch can be observed due to crevice (under-coating) corrosion. In contrast, the coating exhibiting the best active corrosion protection (0.7 wt % MBT@NCs) preserves its integrity and inhibits corrosion sufficiently. This is demonstrated by the defect-free and smooth surface of the scratched area with no traces of corrosion products (Figure 4.22b).
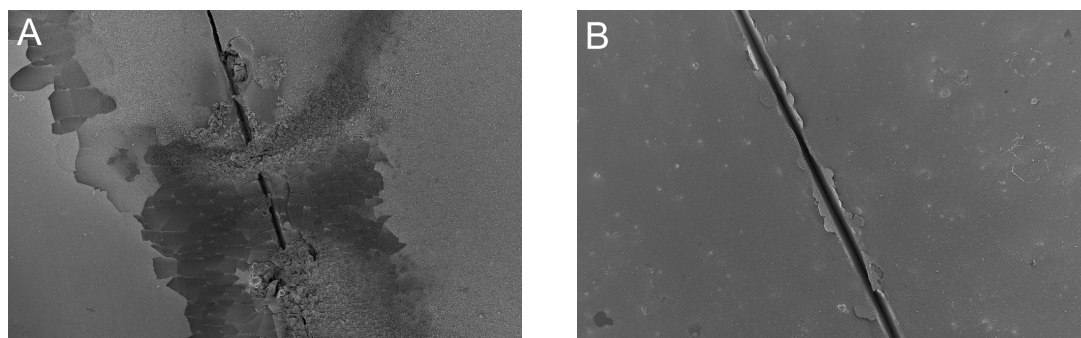
Figure 4.22 SEM micrographs of the scratched area after SVET analysis of a) the control (0 wt % MBT@NCs) and b) the sample exhibiting lowest anodic current density (0.7 wt % MBT@NCs).

4.2.1.2.2 Passive corrosion resistance

Electrochemical impedance spectroscopy (EIS) was used to evaluate the barrier properties and long-term corrosion resistance of the coated samples. The studied coatings functioning as pretreatments were directly exposed to a highly concentrated (1 M) NaCl solution without the deposition of additional layers (primer and top coat), which form an industrial final coating system. EIS spectra were collected over a time range of 14 days in order to understand the mechanism of ongoing corrosion and to quantify the anticorrosion performance of the studied coating. The dependence of the complex impedance on the applied frequency provides information about the capacitance and resistance of the different parts of the coating system. The deterioration of coating barrier properties and protective performance is revealed by an increase of capacitance, C, and decrease of resistance, R, leading to reduced |Z|.

The impedance spectra of the AA2024-T3 coated with intact sol-gel coatings containing different MBT@NC concentrations after 1 day immersion in 1 M NaCl are represented in the form of Bode plots in Figure 4.23. The phase angle spectra (Figure 4.23b) reveal two time constants (two maxima). The high frequency time constant (10^2 – 10^3 Hz) can be ascribed to the sol-gel coating capacitance (C_{coat}) and the low frequency time constant (1 – 10 Hz) to the capacitance of the intermediate oxide layer (Al–O–Si) at the metal-coating interface (C_{oxide}).[189] These elements of the coating system show a resistive response, revealed by the two plateaus in the high (R_{coat}) and
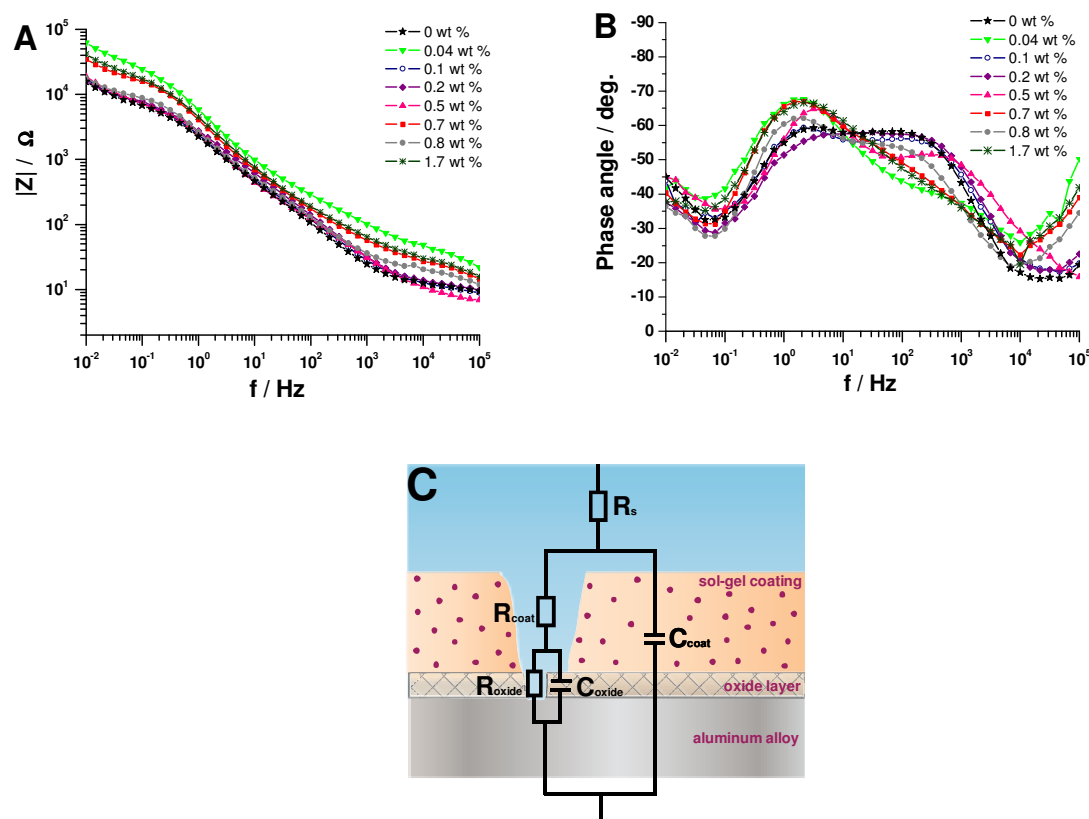
Figure 4.23 Bode plots showing the a) absolute impedance and b) phase angle as a function of frequency after 1 day immersion in 1 M NaCl of AA2024-T3 substrates coated with single layer sol-gel coatings containing different MBT@NC concentrations; c) schematic representation of the coated sample parts and their corresponding equivalent circuit elements.

low (R_{oxide}) frequency regions (Figure 4.23a). These resistive parts result from pores and cracks in the coating, as shown schematically in Figure 4.23c. As a result, sufficient coating barrier properties are revealed by high resistance of the coating pores, which leads to high |Z| values. Therefore, the two times higher |Z| values measured after 1 day immersion for the coatings with 0.04 wt %, 0.7 wt %, 1.7 wt % MBT@NCs account for better coating barrier properties (Figure 4.23a).

With increased immersion time the aggressive electrolyte species diffused into the coating pores and led to further coating deterioration. Consequently, the formed defects at the coating-metal interface provided preferential pathways for the aggressive electrolyte ions to the metal substrate and caused the decrease of |Z| measured after 7 days immersion. The further deterioration of the passive oxide layer resulted in metal dissolution and changes in the EIS spectra (Figure 4.24). Only one time constant at 10 Hz revealing the charge transfer processes
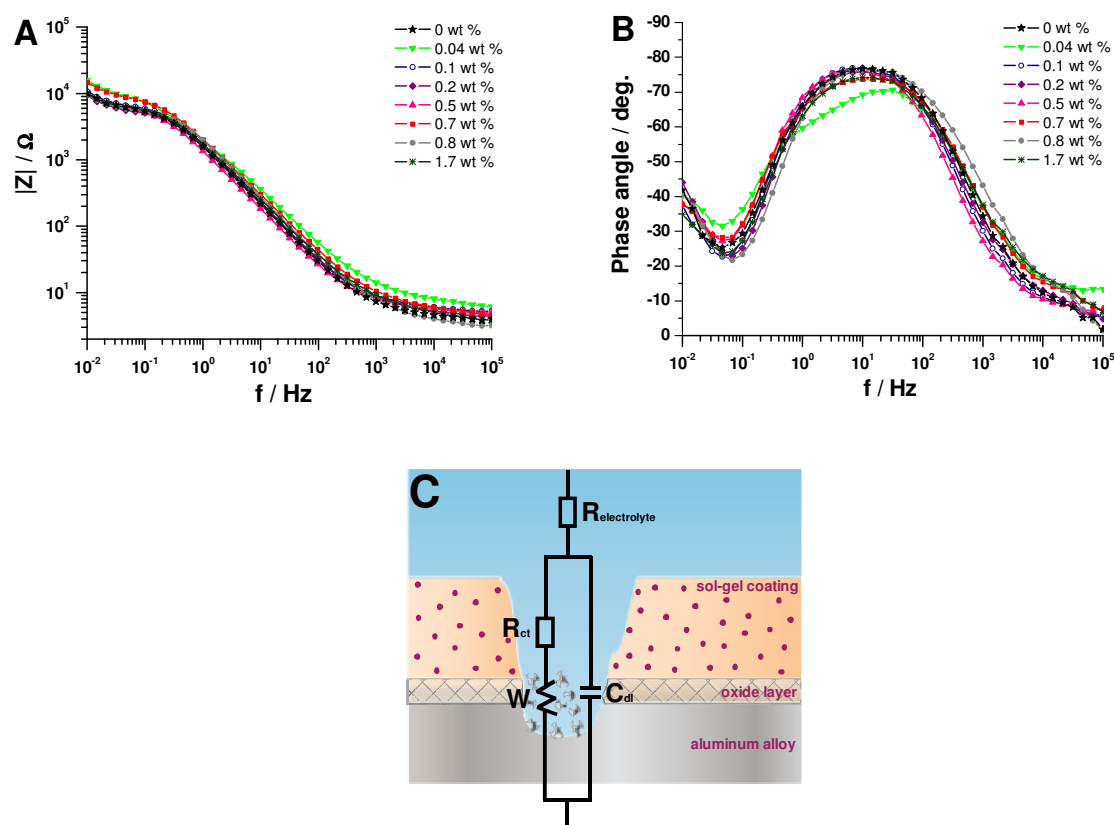
Figure 4.24 EIS data obtained after 14 days immersion in 1 M NaCl and represented as a Bode plot showing the change in a) absolute impedance and b) phase angle as a function of frequency for single layer sol-gel coatings with different MBT@NC concentration; c) schematic representation of the equivalent circuit elements and their physical meaning.

in the corroded areas was detected (Figure 4.24b).[108] In addition, a new time constant at 0.01 Hz was found, accounting for the diffusion controlled mass transfer of the corrosion products and corrosive agents diffusing to or from the metal surface.[190] Thus, after 14 days immersion in the highly concentrated (1 M) NaCl solution, the detected electrochemical impedance response was dominated by the corrosion processes at the coating-metal interface as shown schematically in Figure 4.24c.

The Nyquist plots of all coated samples after 14 days immersion (Figure 4.25a) are characterized by a semicircle at high frequencies, corresponding to the charge transfer processes, and a straight line at low frequencies, representing the Warburg diffusion. Such Nyquist plots originate from electrochemical systems that can be represented by the Randles equivalent circuit (Figure 4.25b, inset).
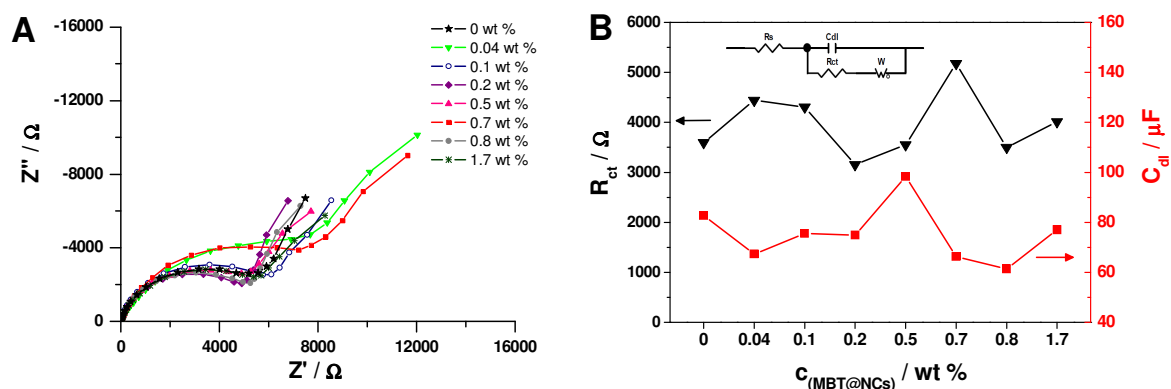
Figure 4.25 EIS data obtained after 14 days immersion in 1 M NaCl for single layer sol-gel coatings with different MBT@NC concentrations: a) experimental data represented as a Nyquist plot and b) calculated data for the charge transfer resistance (R_{ct}) and double layer capacitance (C_{dl}) obtained after numerical fitting of the EIS spectra measured after 14 days immersion with the equivalent circuit shown in the inset.

The Randles equivalent circuit consists of the solution (electrolyte) resistance (R_s), double layer capacitance (C_{dl}), charge transfer resistance (R_{ct}) and Warburg diffusion element (W).[191] The Warburg diffusion element represents the diffusion controlled mass transport of the corrosion products and the corrosive species. The double layer capacitance and the charge transfer resistance characterize the corroded areas and contribute to the absolute impedance values in the low frequency region. Using this equivalent circuit (Figure 4.25b, inset), a numerical fitting of the measured EIS spectra after 14 days immersion was performed. The calculated values of R_{ct} and C_{dl} for the studied coating systems after 14 days immersion in 1 M NaCl are presented in Figure 4.25b. High R_{ct} and low C_{dl} values reveal a limited electrolyte uptake and preserved barrier integrity. Therefore, all coating systems with resistances lower than that of the control coating without MBT@NCs demonstrate poor barrier properties resulting in insufficient corrosion resistance. The highest resistance value was obtained for the coating with 0.7 wt % MBT@NCs, followed by the coating with the lowest studied MBT@NC concentration (0.04 wt %). These coating systems also exhibit very low double layer capacitance values. In addition, they demonstrate the highest absolute impedance values in all frequency ranges during the whole EIS study. The incorporation of MBT@NCs at low concentrations (0.04 – 0.1 wt %) allows homogeneous dispersion of the NCs within the sol-gel matrix resulting in a better

integrity and stability of the coating matrix. Furthermore, having fewer embedded NCs provides less interfacial area between the sol-gel matrix and the NC wall. Consequently, less diffusion paths are present in the coatings with low MBT@NCs concentration, which restricts the diffusion of aggressive electrolyte species towards the metal substrate. The good barrier properties of the coatings with higher MBT@NC concentrations can be explained by the higher amount of available inhibitor. The positive effect of the inhibiting species relies on their release upon the onset of corrosion. The released inhibitor molecules form a layer on the metal surface, which terminates the corrosion processes and restores partially also the coating barrier properties in the damaged coating area. In this study, higher inhibitor concentrations were achieved by using higher MBT@NC concentrations in the coating. However, increasing the concentration of the embedded MBT@NCs above an optimum level (0.7 wt %) leads to poorer anticorrosion performance of the coating, as shown from the impedance data. This effect is due to the deterioration of the integrity and barrier properties of the coating by possible agglomeration of the MBT@NCs embedded at higher concentrations.

A simple way to evaluate the barrier properties of the coating systems is by comparing the absolute impedance values at the lowest measured frequency ($|Z|_{0.01Hz}$) accounting for the corrosion resistance (Figure 4.26).
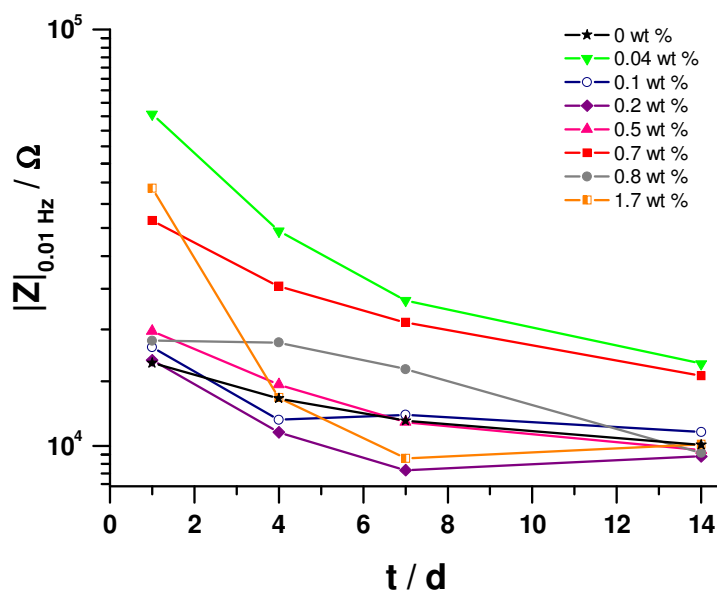

Figure 4.26 Measured absolute impedance values at 0.01 Hz over the course of the EIS study for the different intact coating samples immersed in 1 M NaCl.

The best coating performance over the whole course of the test is provided by the coatings with 0.04 wt % and 0.7 wt % MBT@NCs. These results reflect the ability of the NCs to passively preserve the coating integrity when introduced at very low concentrations and to actively improve the barrier stability by corrosion inhibition when embedded at sufficiently high concentrations.

The EIS results are in good agreement with the visual observation of the coated samples after 14 days immersion (Figure 4.27). The dark pit-like defects and deposits of white corrosion products on the coating surface account for the extensive corrosion attack in the coatings with 0 wt % and 1.7 wt % MBT@NCs. This classifies them as inefficient to provide long-term corrosion resistance. In contrast, a significantly smaller corrosion attack is observed for the coating with 0.04 wt % MBT@NCs, which also demonstrates good barrier properties in the EIS spectra. In addition, the areas in the coated samples, which are undamaged by corrosion, are intact and no coating delamination can be observed. This indicates good coating stability and sufficient adhesion to the metal after 14 days immersion in 1 M NaCl.
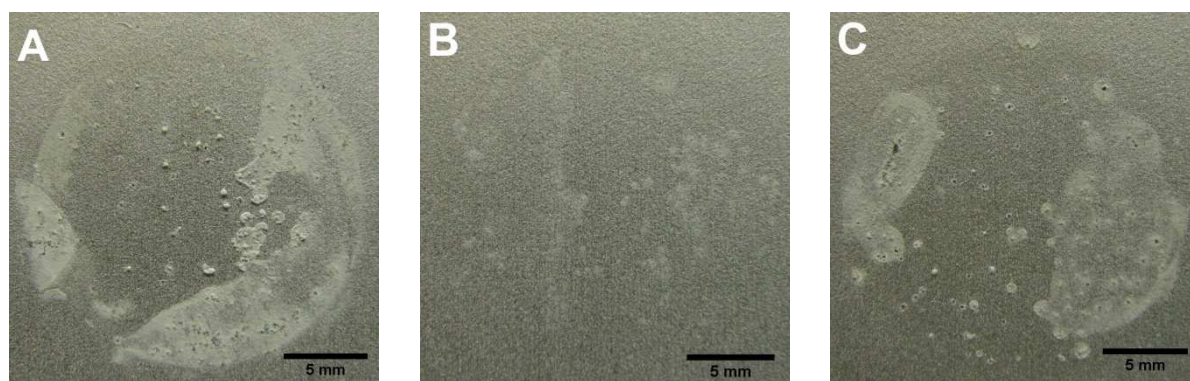

Figure 4.27 Photographs of the samples coated with a single sol-gel layer containing a) 0 wt %, b) 0.04 wt % and c) 1.7 wt % MBT@NCs after 14 days immersion in 1 M NaCl.

In this chapter, the successful incorporation of MBT loaded silica NCs (MBT@NCs) in a passive sol-gel layer was demonstrated. The obtained simple, anticorrosive coatings for the industrially important, corrosion-prone aluminum alloy, AA2024-T3 exhibited good corrison inhibition. This is due to the high amount of nontoxic inhibitor (20 wt %) stored in the NCs, which was released upon corrosion attack to provide active corrosion inhibition on demand. The effect of the concentration of embedded NCs on the coating anticorrosion efficiency was determined to be a critical factor. It was found that incorporating MBT@NCs is not always favorable for the anticorrosion performance of the coating. Embedding MBT@NCs at very low concentrations (0.04 wt %) led to good coating barrier properties but no satisfactory active corrosion inhibition due to an insufficient amount of available inhibitor. In comparison, too high MBT@NC concentrations (0.8 – 1.7 wt %) deteriorate the coating integrity by introducing diffusion paths for aggressive electrolyte species, which results in a loss of anticorrosion efficiency. The best passive and active corrosion resistance was provided by the coating containing 0.7 wt % MBT@NCs, as determined with EIS and SVET analysis. This good anticorrosion performance is due to the preservation of the coating barrier properties and the sufficient inhibitor concentration (0.14 wt %).

Therefore, in order to obtain protective coatings with optimum anticorrosive properties, a compromise between coating integrity and active corrosion inhibition should be found.

4.2.2   Influence of nanocontainer position

In the previous Chapter 4.2.1, it was demonstrated that the nanocontainer concentration in the coating matrix is a critical factor for achieving optimum anticorrosion efficiency.[124] Another important factor with a strong impact on the overall performance of the studied anticorrosive coatings is the distance between the inhibitor loaded NCs and the metal surface to be protected. One might argue that active protection requires the NC to be as close to the metal surface as possible, but this in turn may affect barrier properties and adhesion. In this chapter, the synergetic effect of inhibitor path length to the metal surface and inhibitor amount was analyzed by varying the position and concentration of MBT@NCs in double layer sol-gel coatings. The anticorrosion performance of the studied coating systems was assessed by aiming a balance between optimum barrier properties, active protection and adhesion.

4.2.2.1 Physical properties of the coatings

In order to study the influence of nanocontainer position, double layer sol-gel coatings doped with MBT@NCs were prepared, following a procedure similar to the one used for the single layer coatings (Chapter 4.2.1). Two coating systems differing in the position and concentration of the embedded MBT@NCs were designed: (A) double layer coating with the top layer doped with MBT@NCs and (B) double layer coating with the bottom layer doped with MBT@NCs. Different amounts of MBT@NCs were successfully dispersed in the sol-gel solution to obtain the following concentrations per one layer of the final cured double layer coating systems: 0, 0.04, 0.1, 0.2, 0.5, 0.7, 0.8 and 1.7 wt %. The thickness of the cured coatings deposited on the aluminum alloy was measured with a coating thickness gauge using the Eddy-current principle.[158] Similar coating thicknesses in the range of 4 µm to 5 µm were obtained for both coating systems (Figure 4.28). Considering the measurement error (~ 30 %) due to the high metal surface roughness and thin coatings, the measured thicknesses of the double layer coatings are comparable with the ones of the single layer coatings (4 µm – 5 µm). Taking this into account as well as the coating design, we can assume that the concentration of MBT@NCs in the volume of the whole double layer coating systems is around two times lower compared to the single layer coating system.
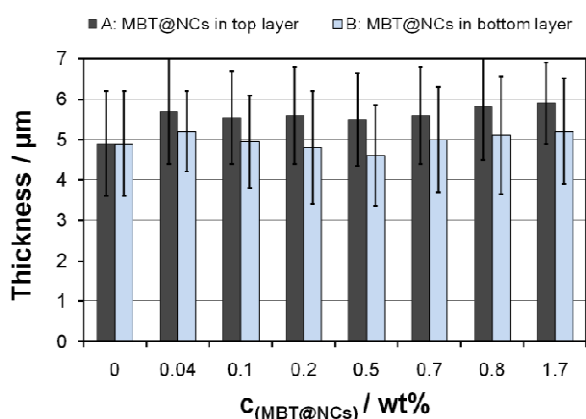
Figure 4.28 Measured coating thicknesses of the cured double layer coatings containing different concentrations of MBT@NCs in the top (A) or bottom (B) layer.

Using a pull-off test according to the standard method, ASTM D4541, the dry adhesion of the freshly cured coatings was determined as described above. The measured adhesion values of both coating systems to the metal surface are comparable and in the range of 2 – 3 MPa (Figure 4.29).[181-183] Coating adhesion did not correlate with embedded MBT@NC concentration in a defined way. However, coatings with MBT@NCs demonstrate comparable or slightly higher adhesion to the metal than the ones without MBT@NCs. This suggests that embedding MBT@NCs in the sol-gel matrix preserves the stability of the coating and its adhesion to the metal. Furthermore, a complete removal of both coating layers was observed for all samples. This indicates good adhesion between the layers of the double layer coating system.
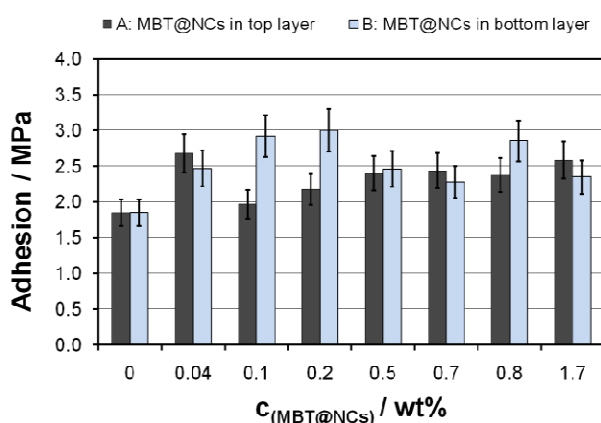

Figure 4.29 Measured adhesion of the freshly cured double layer coatings with MBT@NCs in the top (A) or bottom (B) layer to the metal substrate (AA2024-T3).

4.2.2.2 Anticorrosive properties of the coatings

4.2.2.2.1 Active corrosion resistance

In order to evaluate the active corrosion resistance of the coated samples, the evolution of corrosion in an artificial scratch in the coating was studied using the scanning vibrating electrode technique (SVET). The galvanic coupling between the intermetallic particles and the surrounding aluminum matrix in the aluminum alloy, AA2024-T3, used as a substrate, promotes localized corrosion. Upon initiation of corrosion the electrochemical reactions occurring at the metal surface cause a positive anodic and a negative cathodic ionic current flow, which leads to potential differences in the electrolyte solution. Employing SVET, these potential differences are measured and converted into an electrical current density over the scanned area. For the quantification of the overall electrochemical activity, the current density maps taken periodically were integrated to calculate the minimum (cathodic) and maximum (anodic) currents as a function of time.[179,186] The 3D current density maps obtained for exemplary coated samples after 12 h immersion are depicted in Figure 4.30.
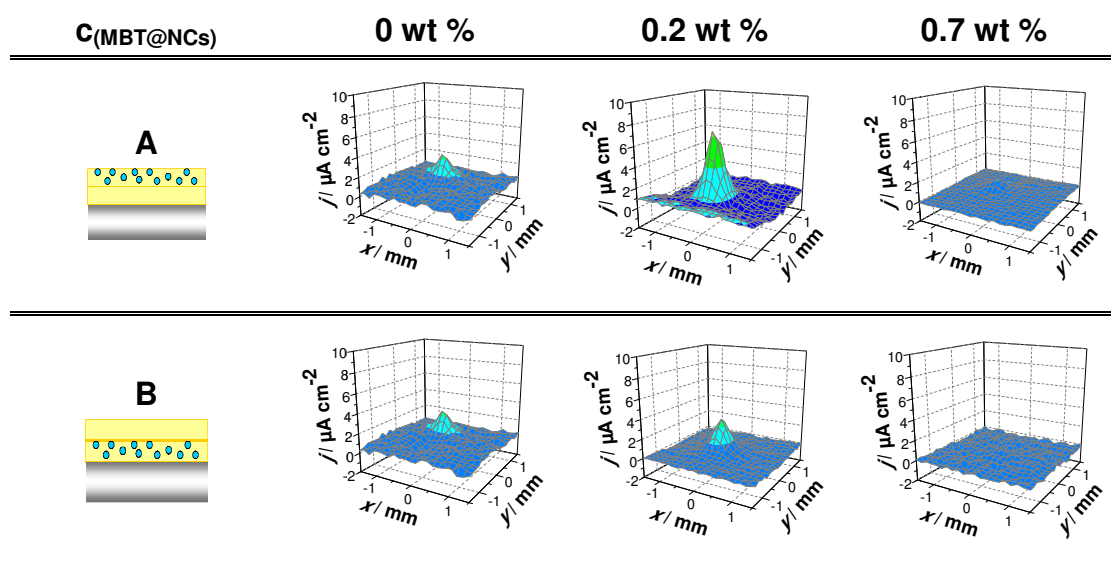

Figure 4.30 SVET 3D current density maps of the studied coating systems A and B (left). Examples of coated samples with detected high (MBT@NCs = 0.2 wt %) and low (MBT@NCs = 0.7 wt %) anodic current densities in comparison to the control (MBT@NCs = 0 wt %) after 12 h immersion in 0.1 M NaCl.

The anodic activity is represented as a single positive peak with a constant position indicating the site of a corrosion anode. The anodic peak intensity is proportional to the degree of metal dissolution. In contrast, a cathodic activity related to the oxygen reduction is poorly pronounced and not characterized by a localized peak. Therefore, the hardly detected cathodic current that is not a direct measure of aluminum degradation is not plotted as a function of time.[188] Instead, the efficiency of corrosion inhibition is described by the increase of the anodic current (Figure 4.31 and 4.32). Coated samples exhibiting higher anodic activity than the control sample without inhibitor possess no self-healing properties. If the MBT@NCs are embedded in the top layer of the coating (coating system A), most of the studied samples fail to actively inhibit corrosion (Figure 4.31). The samples with too low MBT@NC concentration (0.04 – 0.2 wt %) provide insufficient amount of corrosion inhibitor to stop the corrosion propagation, which results in higher anodic activity than the control. Surprisingly, very high amount of available inhibitor (*i.e.* higher c(MBT@NCs) = 0.8 – 1.7 wt %) in the coating system A does not favor the corrosion inhibition. These results can be explained by a possible deterioration of the coating matrix due to the high amount of embedded NCs leading to more paths for the aggressive chloride ions and more corrosive attack sites. Thus, the samples in which the top layer contains MBT@NCs of intermediate concentrations (0.5 – 0.7 wt %) provide the best corrosion inhibition and suppress the anodic current at around 5 nA in comparison to the lower and higher NC concentrations.
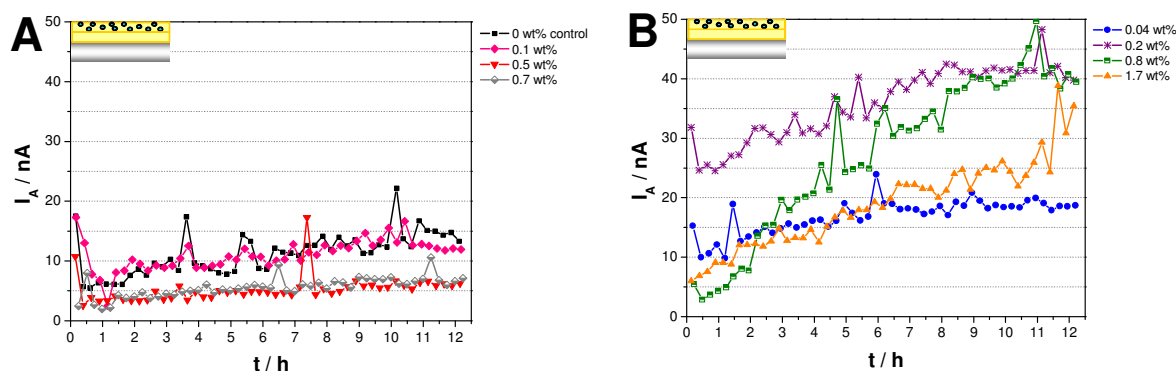

Figure 4.31 Maximum anodic currents detected with SVET over the scanned scratched area during a 12 hour immersion period in 0.1 M NaCl. Results are shown for samples coated with two layers of sol-gel containing different MBT@NC concentrations in the top layer demonstrating a) efficient and b) unsatisfactory active corrosion inhibition.
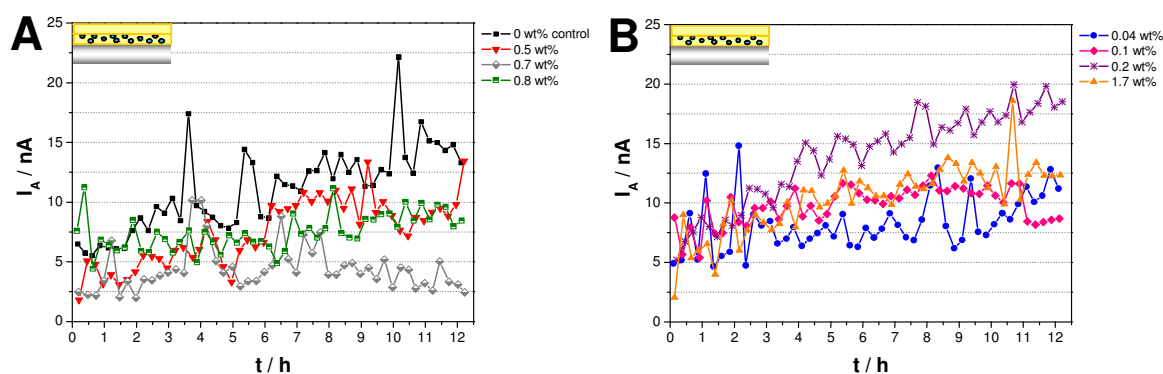
Figure 4.32 Maximum anodic currents detected with SVET over the scanned scratched area during a 12 hour immersion period in 0.1 M NaCl. Results are shown for samples coated with two sol-gel layers containing different MBT@NC concentrations in the bottom layer exhibiting a) efficient and b) unsatisfactory active corrosion inhibition. Note that I_A is plotted for an anodic current range, which is two times smaller than the one in Figure 4.31.

In contrast, the samples with MBT@NCs in the bottom layer (coating system B) close to the metal surface show lower anodic activity (maximum $I_A \sim 20$ nA) than the samples with MBT@NCs in the top layer, qualifying them as coating systems providing better active protection (Figure 4.32). A possible explanation could be the shorter distance between the MBT@NCs and the attacked metal surface providing a shorter diffusion length and time for the inhibitor molecules to reach the corrosion initiation site and to form a surface complex to inhibit corrosion propagation. Furthermore, in the coating system B no well pronounced differences in the detected anodic currents for too high or too low MBT@NC concentrations were observed. However, the anodic current measured for the sample with 0.7 wt % MBT@NCs in the bottom layer was an exception to this trend and remained at the lowest level of 5 nA. Based on the SVET results, the optimum MBT concentration needed for sufficient active corrosion inhibition was determined to be 0.14 wt % (corresponds to c(MBT@NCs) = 0.7 wt %) for both double layer coating systems.

In addition, the double layer coating systems suppressed the anodic activity better than the single layer coatings described in the previous chapter (Figure 4.21).[124] The corrosion propagation in samples coated with a single sol-gel led to anodic currents above 50 nA. This finding suggests that introducing a second layer in the coating improves the active anticorrosive properties.

4.2.2.2.2 Passive corrosion resistance

The barrier properties and passive corrosion resistance of the double layer coatings were studied with electrochemical impedance spectroscopy (EIS). The coated AA2024-T3 plates were exposed to 1 M NaCl for 14 days and EIS spectra were collected at different time intervals. The obtained spectra were normalized with the area of the working electrode (3 cm²) to obtain the impedance in Ω cm². The change with time in corrosion resistance of the studied coatings was evaluated by comparing the impedance at the lowest measured frequency, $|Z|_{0.01Hz}$ (Figure 4.33).
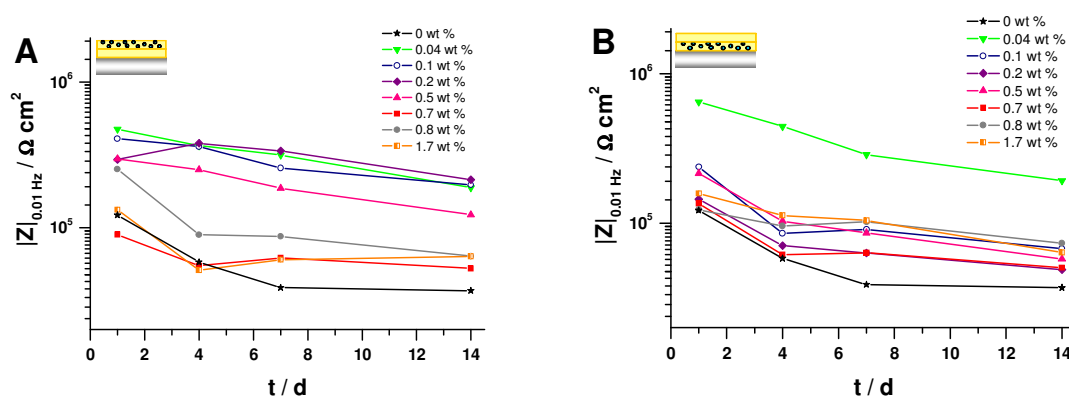

Figure 4.33 $|Z|$ values measured at the lowest frequency, 0.01 Hz over the course of the EIS study in 1 M NaCl. Results for the double layer coating systems containing different MBT@NC concentrations in a) the top or b) the bottom layer are shown.

The relative impedance decrease for all coatings containing MBT@NCs is comparable, which suggests a comparable degradation rate. However, for low MBT@NC concentrations (c < 0.7 wt %), the coating system with MBT@NCs in the top layer exhibits higher $|Z|_{0.01Hz}$ over the whole course of the test compared to the coating system with MBT@NCs in the bottom layer. These results suggest that introducing MBT@NCs in the top layer at concentrations higher than 0.5 wt % leads to a deterioration of the coating barrier properties (Figure 4.33a). This detrimental effect starts at an even lower concentration (0.04 wt %) when the MBT@NCs are embedded in the bottom layer (Figure 4.33b). Nevertheless, the comparison of the normalized $|Z|_{0.01Hz}$ values for single (Figure 4.34) and double layer coatings demonstrates the superior barrier properties of the double layer coatings. This can be attributed only to the coating design because the coating thickness of all coatings is similar.
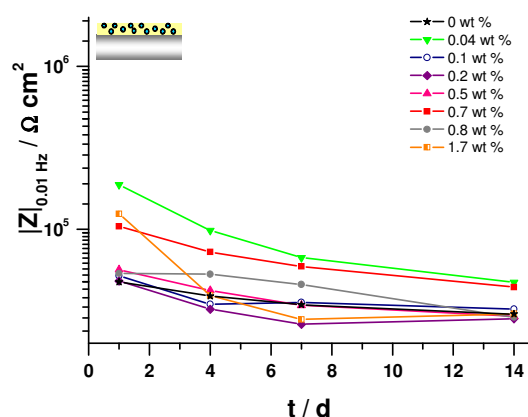
Figure 4.34 |Z| values measured at 0.01 Hz over the course of the EIS study with single layer coating systems immersed in 1 M NaCl. Note that the results were normalized and |Z| values are shown in Ω cm² to enable the comparison with the EIS data for double layer coatings.
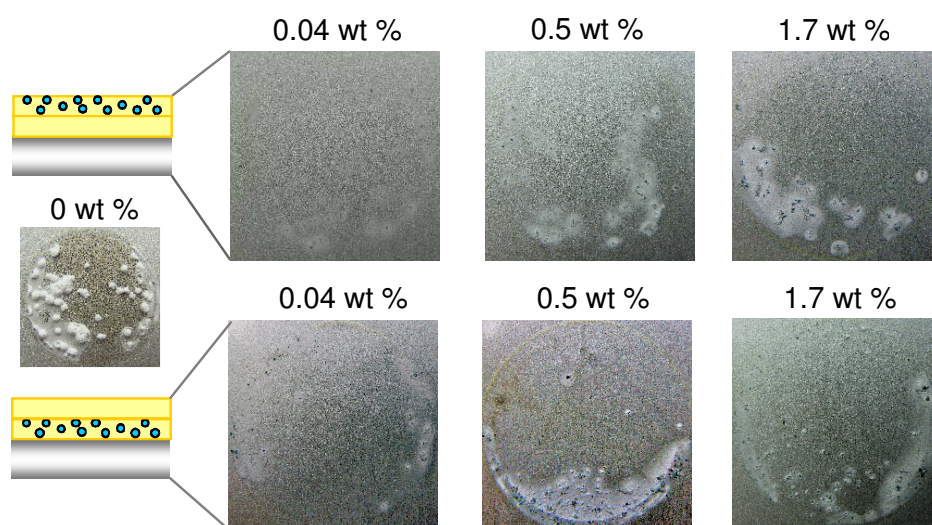

Figure 4.35 Optical photographs of AA2024-T3 coated with double layer coatings containing 0 wt %, 0.04 wt %, 0.5 wt % and 1.7 wt % MBT@NCs after 14 days immersion in 1 M NaCl.

The optical photographs of the coated samples after 14 days immersion in 1 M NaCl reveal some black pits and white deposits, which indicate corrosion attack (Figure 4.35). The visual observation is reflected in the EIS specta (Figure 4.36 and 4.37), which can be characterized by three time constants. The high frequency time constant (10^5 Hz) can be ascribed to the coating response (CPE_{coat} and R_{coat}). The second time constant at intermediate frequencies is usually associated with the native aluminum oxide layer (Figure 4.36).

Figure 4.36 EIS data obtained after 14 days immersion in 1 M NaCl and represented as a Bode plot showing the change in a) impedance and b) phase angle as a function of frequency for double layer coatings containing different MBT@NC concentrations in the top layer.

However, after 14 days immersion of the coated samples in 1 M NaCl, the oxide layer was deteriorated and could not be detected because of the ongoing corrosion as observed also visually (Figure 4.35). Therefore, the occurrence of corrosion (CPE_{dl} and R_{ct}) dominated the EIS spectra after 14 days and was described by the second time constant (1 – 10 Hz). The third time constant at the lowest frequency (0.01 Hz) describes the mass transport of corrosion products and corrosive agents between metal surface and electrolyte.[190]
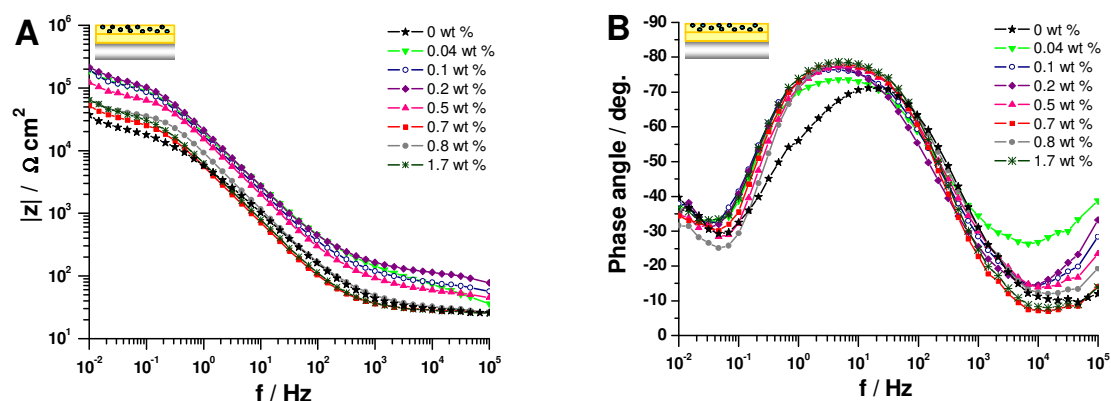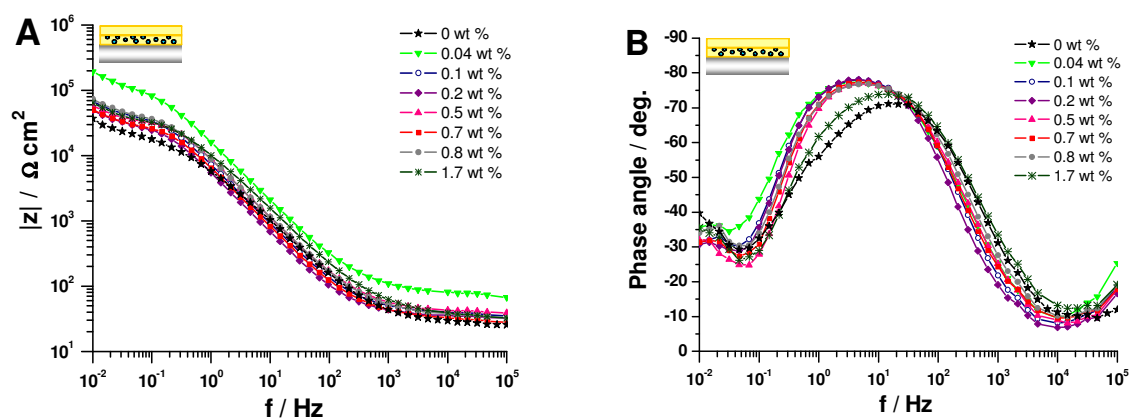

Figure 4.37 EIS data obtained after 14 days immersion in 1 M NaCl and represented as a Bode plot showing the change in a) impedance and b) phase angle as a function of frequency for double layer coatings containing different MBT@NC concentrations in the bottom layer.
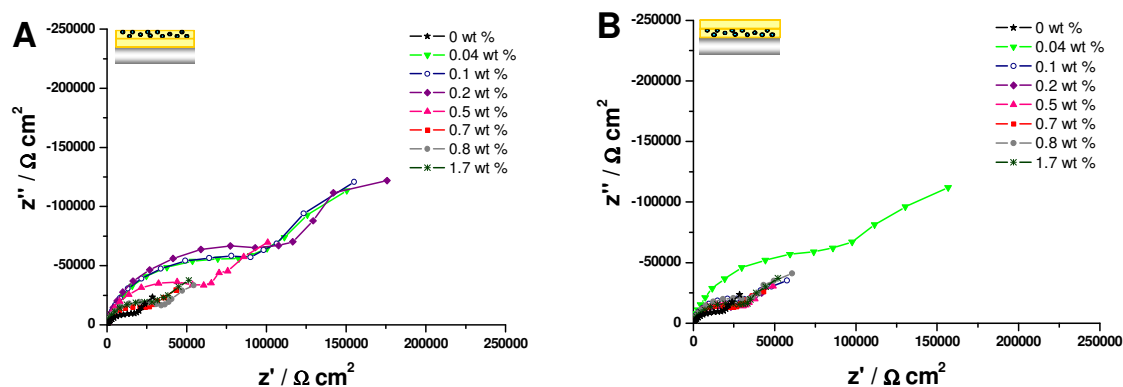
Figure 4.38 EIS data obtained after 14 days immersion in 1 M NaCl and represented as Nyquist plots for the double layer coating systems containing different MBT@NC concentrations in a) the top or b) the bottom layer.

The Nyquist plots of the EIS data obtained after 14 days immersion in 1 M NaCl reflect and confirm the observations from the Bode plots (Figure 4.38). Thus, the incomplete semi-circle corresponds to the corrosion process and the line at low frequencies to the diffusion controlled mass transport of species taking part in the corrosion process.

An equivalent circuit including the above mentioned time constants is shown in Figure 4.39c and was used to numerically fit the EIS spectra for both double layer coatings obtained after 14 days immersion in 1 M NaCl (Figure 4.36 and 4.37). Constant phase elements (CPE) instead of capacitances were used for the fitting because the phase angles deviated from -90°. The capacitances C were calculated using the following equation:

$$C = Q(\omega_{max})^{n-1} \tag{1}$$

in which ω_{max} is the radial frequency at which Z" reaches a maximum for the respective time constant, Q and $0 < n \leq 1$ are parameters calculated for the CPE by fitting.[192]

The calculated values for the charge transfer resistance (R_{ct}) and double layer capacitance (C_{dl}) are presented because these parameters directly indicate the extent of corrosion (Figure 4.39a, b). Good coating barrier properties are revealed by high R_{ct} and low C_{dl} values.
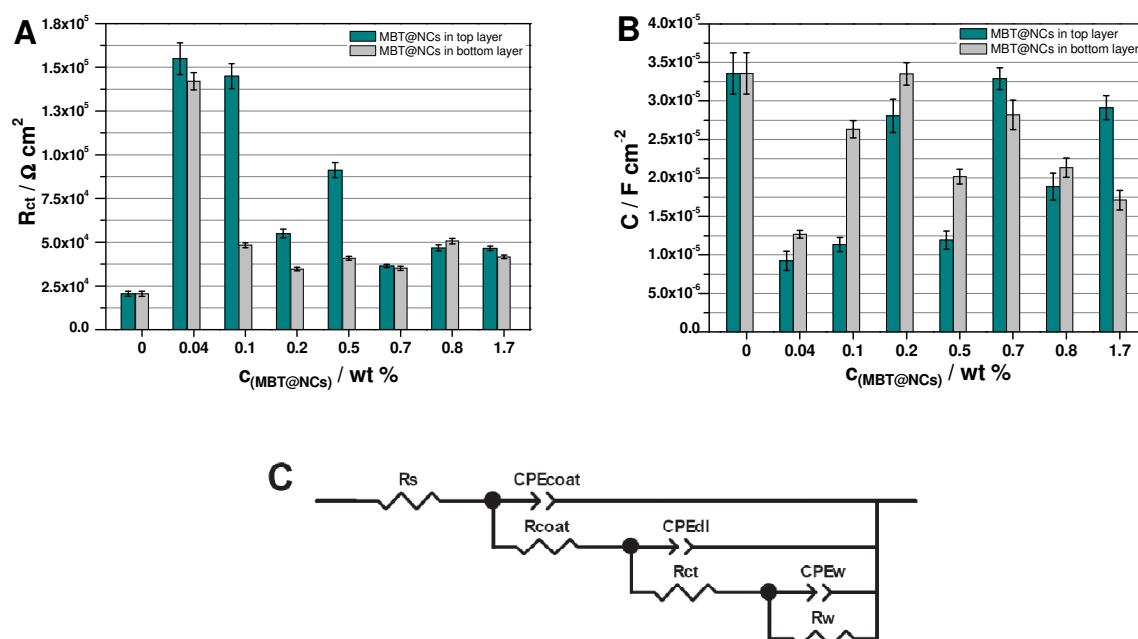
Figure 4.39 Calculated data for a) the charge transfer resistance (R_{ct}) and b) double layer capacitance (C_{dl}) obtained by fitting of the EIS spectra using the equivalent circuit shown in c). EIS spectra of both double layer coating systems measured after 14 days immersion in 1 M NaCl were fitted.

The R_{ct} values for all coatings containing MBT@NCs are higher than for the bare coating. This can be due to the embedded inhibitor, which inhibits the corrosion attack and increases $R_{ct.}$ The incorporation of MBT@NCs at concentrations above 0.5 wt % leads to a comparable electrochemical response for both coating designs. The integration of high MBT@NC concentrations can lead to a degradation of the coating and additional diffusion paths around possible MBT@NC agglomerates. These detrimental effects explain the worse passive corrosion resistance of both coating systems containing high amount of MBT@NCs (c > 0.5 wt %). However, if a small amount of MBT@NCs is embedded, more pronounced differences between the two coating systems can be observed. If the layer with the MBT@NCs is separated from the metal by a bare sol-gel layer, the coating system reveals superior passive corrosion resistance. This can be due to a better adhesion to the aluminum surface of a bare sol-gel layer than a sol-gel layer with MBT@NCs. Thus, the barrier properties of double layer coatings with low MBT@NC concentrations in the top layer compared to the ones with MBT@NCs in the bottom layer are better due to a preserved coating

integrity and good adhesion between coating and metal surface. However, the incorporation of more MBT@NCs leads to the loss of this effect and to a comparable passive corrosion resistance of both coating designs. On the other hand, the addition of NCs to the bottom layer provides better self-healing ability to the coating.

In short, the barrier properties of both coating systems with high MBT@NC concentrations were similar and insufficient. In contrast, embedding low amount of MBT@NCs (c < 0.5 wt %) improved the passive corrosion resistance and classified the coating system with MBT@NCs in the top layer as a better physical barrier.

The coatings systems presented in this chapter contribute to the design of active anticorrosive coatings based on nanocontainers. This was achieved by dispersing the same amount of MBT@NCs as used for the single layer coatings only in half of the whole volume of the double layer coatings. Considering the similar thicknesses of both coating systems, the density of the MBT@NCs in the matrix of the double layer coatings is approximately half of the one in the single layer coatings. Generally, the results obtained for double layer coatings, described in this chapter, revealed that these coating systems protect the AA2024-T3 better from corrosion than the single layer coatings presented in Chapter 4.2.1. Thus, the newly developed design of double layer coatings is a way to obtain satisfactory corrosion resistance even with lower inhibitor amount. Introducing the MBT@NCs close to the metal surface facilitates the fast transport of released inhibitor upon corrosion attack and improves the active corrosion resistance and self-healing ability. On the other hand, better barrier properties are observed for double layer coatings with MBT@NCs in the top layer due to a preserved coating integrity and good adhesion between coating and metal surface.[192-193] Based on this study, optimum active and passive corrosion resistance are provided by double layer coatings containing intermediate MBT@NC concentrations (0.5 – 0.7 wt %) in the top layer.

Although the results obtained in this study describe a specific system, they also provide general information about the factors influencing the anticorrosion performance and properties of active anticorrosive coatings with embedded nanocontainers.

4.2.3   Influence of container size

The choice of containers for active anticorrosive coatings is governed by several factors among which are *e.g.* inhibitor capacity, compatibility with the coating matrix and size. The latter aspect is directly influenced by the coating thickness, which determines the upper limit of the size range for applicable containers. To study the size influence of the embedded containers, two types of porous silica containers, NCs and SHS with d ≈ 80 and 700 nm, respectively, were employed. These containers were thoroughly characterized in Chapter 4.1.1. Due to their comparable specific surface area (~ 1000 $m^2\ g^{-1}$) and pore volume ($\sim 1\ mL\ g^{-1}$) a similar, high MBT loading was obtained (≈ 20 wt %) as revealed by TGA. For the container size study a thicker, water-based organic coating was used. The influence of embedded container size on the thickness and adhesion of freshly cured coatings was investigated to obtain information about the physical properties of the coatings. The barrier properties and self-healing ability of the studied coatings were evaluated by EIS and SVET, respectively. In addition, an accelerated corrosion test, which is part of the specifications to obtain the QUALICOAT quality label for coatings on aluminum alloys, was conducted.

4.2.3.1 Physical properties of the coatings

The water-based organic coating used as a passive coating matrix in the study of the influence of container size is a two-component, model coating developed as a primer for aerospace applications by Mankiewicz GmbH. Single layer organic coatings were applied on AA2024-T3 plates using a spiral bar coater for 50 µm wet coating thickness. Prior to application, water suspensions of MBT@NCs or MBT@SHS of different concentrations were prepared and added to the pre-mixed two-component coating matrix. The following container concentrations in respect to the cured coatings were embedded: 0.04, 0.2, 0.5, 0.7 and 1.7 wt %. The thickness of the cured coatings deposited on the aluminum alloy was measured with a coating thickness gauge using the Eddy-current principle.[158] Similar coating thicknesses ~ 20 µm were obtained for both coating systems (Figure 4.40). A measurement error of ≈ 20 % was obtained due to the high metal surface roughness and the manual coating application method.
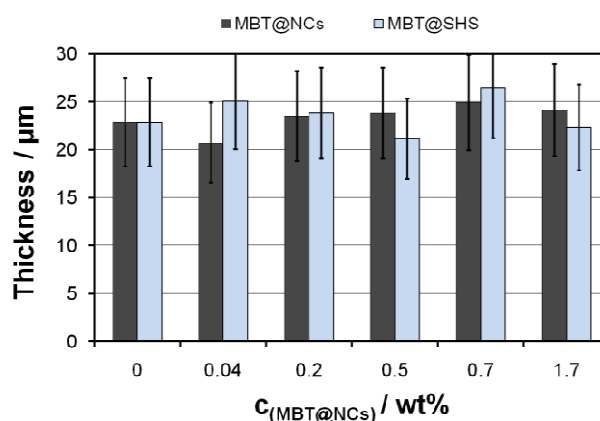
Figure 4.40 Measured coating thicknesses of the cured organic coatings containing different concentrations of MBT@NCs or MBT@SHS.

Considering the measurement conditions, no strong influence of the container size on the coating thickness could be observed and the thicknesses of both coating systems are considered similar. The obtained thickness results classify the thicker organic coating as a better choice for the container size study than the previously described 5 µm thick sol-gel coating, especially assuming a container agglomeration in the coating. The results from the adhesion test with freshly cured organic coatings are shown in Figure 4.41. A measurement error of 10 % was considered due to a glue failure, which led to an incomplete removal of the tested coating area. No exact dependence between measured adhesion, container size and concentration could be observed. All organic coating formulations exhibit similar adhesion to the metal substrate, ~ 3.5 MPa, which is higher than the adhesion values measured with sol-gel coatings (~ 2.5 MPa).
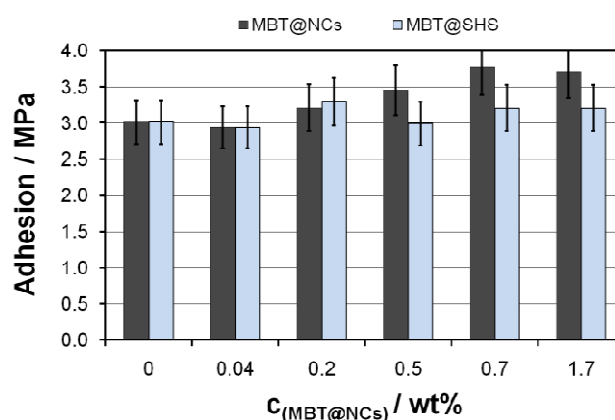

Figure 4.41 Measured adhesion of the freshly cured organic coatings doped with MBT@NCs or MBT@SHS to the metal substrate (AA2024-T3).

4.2.3.2 Anticorrosive properties of the coatings

4.2.3.2.1 Active corrosion resistance

The influence of the container size on the self-healing ability of the anticorrosive coatings was evaluated using SVET. The organic coatings containing different concentrations of MBT@NCs or MBT@SHS were scratched in a controlled way to expose the underlying metal to the corrosive environment (0.1 M NaCl) and to induce a corrosion process. The introduced scratches were ≈ 3 mm long, ≈ 20 µm wide and ≈ 60 µm deep. The scratch dimensions and the dense distribution of intermetallic particles (IMPs) in the aluminum alloy (~ 300 000 particles/cm²)[72] suggest the exposure of enough IMPs to the 0.1 M NaCl to trigger localized corrosion. These IMPs can act as anodes or cathodes depending on their composition, distribution and corrosion stage.[76] Generally, Cu-rich IMPs act as cathodes compared to the surrounding aluminum matrix (the anode) due to their more noble character. The electrochemical reactions occurring at the anode and cathode induce a positive anodic and a negative cathodic current flow, which lead to potential differences in the electrolyte solution. With SVET, the vibrating measuring electrode moved above the scratched sample and detected these potential differences, which were then converted into an electrical current density over the scanned area. In the further data analysis, the current density maps taken periodically were integrated to calculate the minimum (cathodic) and maximum (anodic) currents as a function of time.[179,186] With SVET only currents for anodes and cathodes with sufficient distance between each other could be detected. This limitation comes from the large coating thickness (≈ 20 µm), big measuring height (300 µm), and the assumption that the current between anode and cathode flows in a hemisphere.

It is suggested, that the self-healing effect observed with the studied coatings is triggered by the onset of corrosion and the consequent pH increase (pH ≈ 10) above the cathodes built in AA2024-T3. Basic pH favors the dissolution and release of the loaded MBT, which forms a protective layer on the attacked metal surface. The suggested self-healing mechanism is observed in the SVET data by an increase in the anodic current, accounting for the initiation of corrosion and the consequent suppression of the anodic current, revealing the corrosion inhibition.
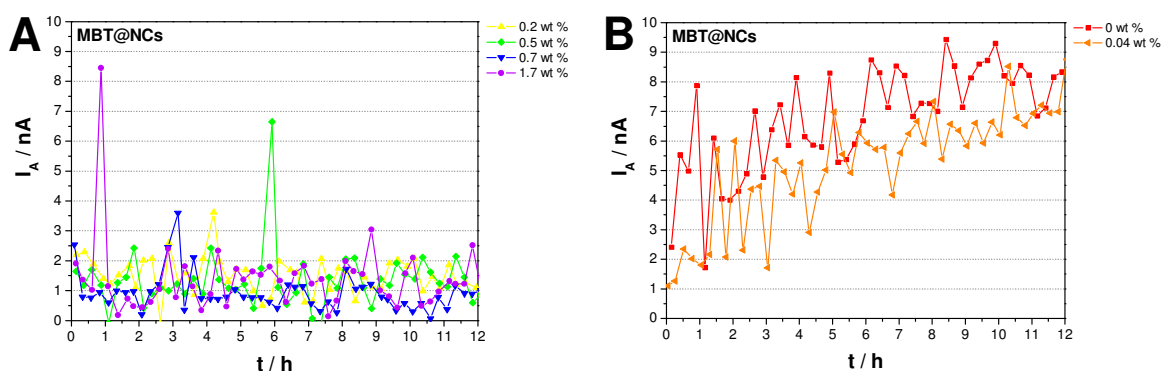
Figure 4.42 Maximum anodic currents detected with SVET over the scanned scratched area during a 12 hour immersion period in 0.1 M NaCl. Results are shown for samples coated with an organic coating containing different MBT@NC concentrations demonstrating a) efficient and b) unsatisfactory active corrosion inhibition.

The detected anodic currents as a function of time for AA2024-T3 coated with organic coatings containing different concentrations of MBT@NCs are shown in Figure 4.42. A constant increase in anodic current with time reflects the dissolution of aluminum due to ongoing corrosion. Such behavior was detected for samples with too low inhibitor amount (c(MBT@NCs) = 0.04 wt %), which was not enough to actively suppress the corrosion (Figure 4.42b). By increasing the amount of available inhibitor in the coatings (c(MBT@NCs) ≤ 0.2 wt %), better active corrosion resistance and self-healing ability was observed. This is revealed by the suppression of the measured anodic current at values lower than ≈ 2 nA. Surprisingly, even very high amount of embedded NCs (1.7 wt %) led to good corrosion resistance. This suggests, for the studied concentration range (c(MBT@NCs) = 0.04 – 1.7 wt %), that the coating barrier properties and integrity are preserved, when high amount of small containers are embedded. In contrast, embedding bigger containers at the same high concentration (c(MBT@SHS) = 1.7 wt %) led to worse barrier properties and insufficient active corrosion resistance (Figure 4.43b). For the first 5 hours of immersion in 0.1 M NaCl, this sample managed to inhibit successfully corrosion due to the high amount of available inhibitor. However, after 5 hours the deterioration of coating barrier properties dominated the overall anticorrosion performance and led to failure in corrosion inhibition.
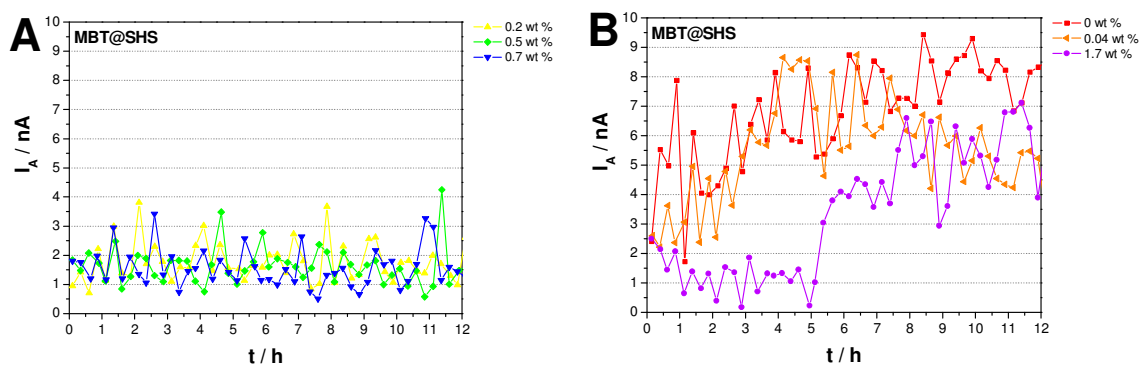
Figure 4.43 Maximum anodic currents detected with SVET over the scanned scratched area during a 12 hour immersion period in 0.1 M NaCl. Results are shown for samples coated with an organic coating containing different MBT@SHS concentrations demonstrating a) efficient and b) unsatisfactory active corrosion inhibition.

When MBT@SHS are embedded at intermediate concentrations (0.2 – 0.7 wt %), the same behavior as for the MBT@NCs was observed (Figure 4.43a). In contrast, for samples with MBT@SHS, no distinct increase of I_A, revealing clearly the onset of corrosion was observed. The detected active corrosion inhibition can be caused by corrosion reactions taking place between cathodes and anodes placed very close to each other. Thus, the resulting corrosion current flows develop very close to the metal surface and cannot be detected by the measuring electrode at 300 µm above the coating surface.

Generally, the currents detected with SVET for samples coated with organic coatings are very low, which might be due to their good self-healing ability combined with strong adhesion of these coatings to the metal surface, good barrier properties and IMPs distribution.

In order to confirm the results obtained with SVET, the coated samples and the area around the scratch were investigated with SEM after the end of the SVET study (after 12 hours immersion in 0.1 M NaCl). The elemental composition of the structures present around the scratch was investigated with SEM-EDX. The SEM image shown in Figure 4.44 depicts a representative coated sample after the SVET study on which the three types of commonly detected structures around the scratch are represented (indicated with red circles).
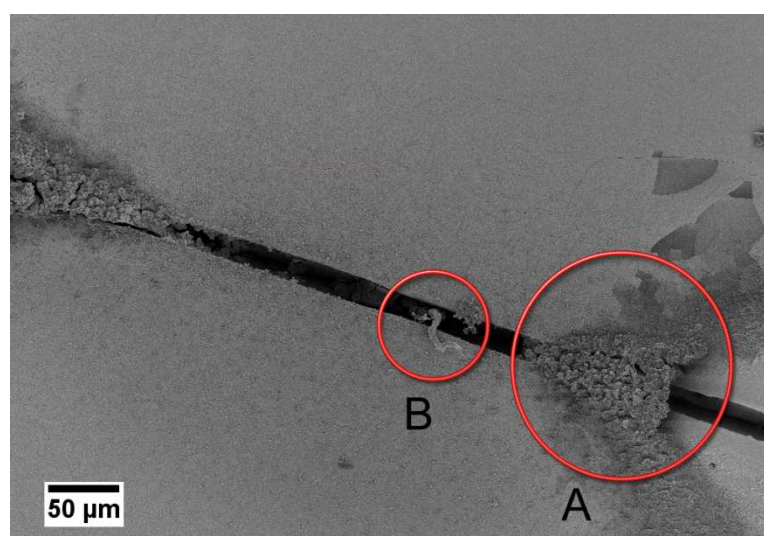
Figure 4.44 SEM micrograph of a representative coated sample measured with SVET. The usually detected structures, accumulated around the scratch are indicated with red circles.

The SEM-EDX spectra obtained for the indicated areas in the SEM micrograph are shown in Figure 4.45. The elements dominating the spectra are aluminum and oxygen, because the investigated structures consist mainly of those elements. A peak for chlorine is also present in the spectra. The small amounts of detected gold result from sputtering the samples with gold/palladium. Thus, the elemental composition of the structures usually detected around the scratched area of coated samples, which were exposed to 0.1 M NaCl for 12 hours during the SVET measurements was revealed by SEM-EDX. Based on these results, it can be concluded that these are corrosion products of the aluminum alloy, which deposit as aluminum oxide or chloride with different morphologies. The most often detected morphology is the grain like accumulations indicated in area A of Figure 4.44.

Figure 4.45 SEM-EDX spectra obtained for the correspondingly labeled areas indicated with red circles in Figure 4.44.

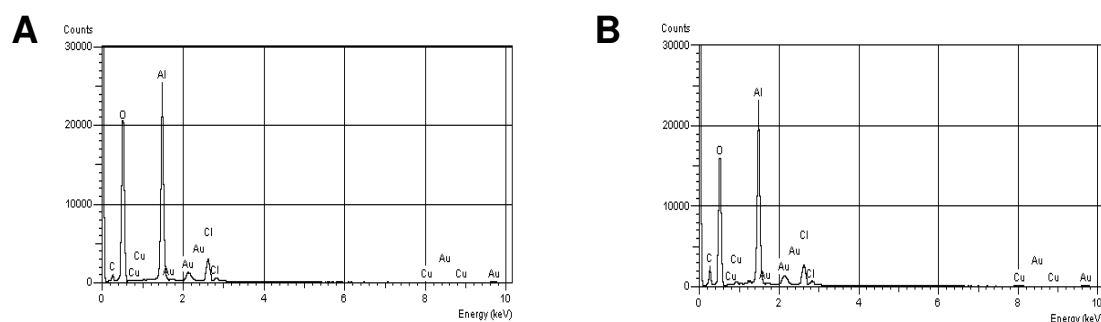The extent of corrosion was assessed in accordance with the amount of corrosion products built around the scratched area (Figure 4.46 and 4.47). For the control sample, a big amount of corrosion products is accumulated at two sites along the scratch, suggesting one anode site between those. In addition, the coating damage at the borders of the scratch reveals a deterioration of the coating barrier properties due to corrosion. Similar SEM results were obtained for the coatings containing a small concentration of MBT@NCs or MBT@SHS (0.04 wt %). Thus, the big amount of corrosion products around the scratch confirms an insufficient active corrosion resistance for low inhibitor amount, as detected with SVET. In contrast, the coatings with efficient active corrosion resistance (0.2 – 0.7 wt %), are characterized by smooth surfaces and no big accumulations of corrosion products. The corrosion for these samples was inhibited successfully and only a small amount of corrosion products could be detected by SEM. These were detected as (i) fine grains dispersed in a thin layer on the coating surface and/or (ii) accumulation of small amount of corrosion products in the scratch.
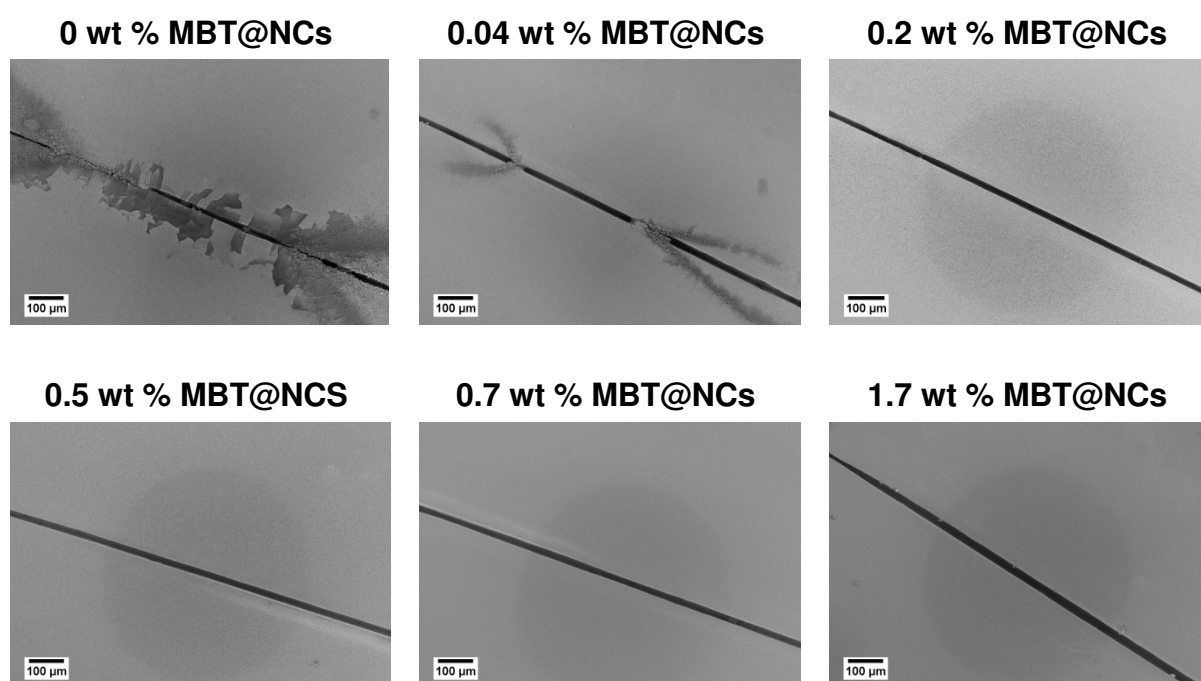
Figure 4.46 SEM analysis of the samples measured with SVET for 12 hours in 0.1 M NaCl. Micrographs are shown for the scratched area of samples coated with organic coatings containing different concentrations of MBT@NCs.
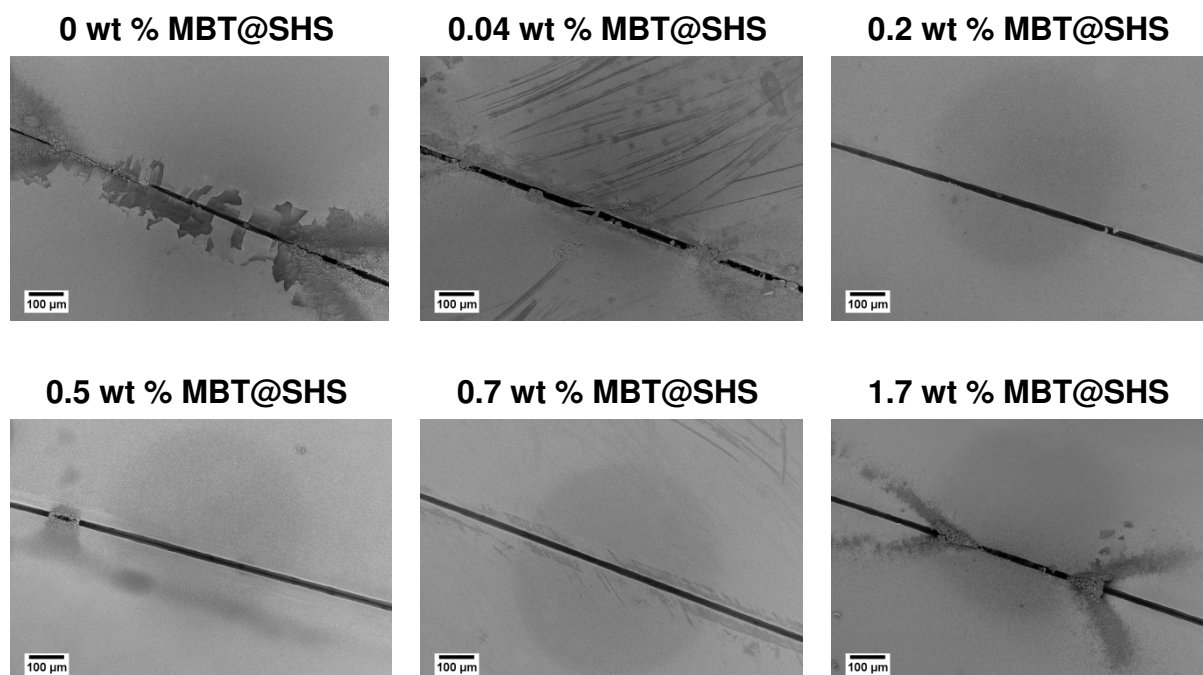
Figure 4.47 SEM analysis of the samples measured with SVET for 12 hours in 0.1 M NaCl. Micrographs are shown for the scratched area of samples coated with organic coatings containing different concentrations of MBT@SHS.

The presence of corrosion products, even a small amount, confirms that the corrosion process was initiated. Thus, when sufficient amount of inhibitor was available in the coating, it was released upon corrosion onset to inhibit the metal dissolution and the further formation of corrosion products. However, this is valid only, when also the barrier properties of the coatings are preserved. The high amount of available inhibitor couldn't compensate for the deteriorated barrier properties on long term, as revealed by SVET and SEM data for the sample with 1.7 wt % MBT@SHS (Figure 4.47).

4.2.3.2.2 Passive corrosion resistance

Coating barrier properties are an important aspect of the coating overall performance. In order to investigate the long-term protection provided by the developed coatings, coated AA2024-T3 plates were immersed in 1 M NaCl and their passive corrosion resistance was studied with electrochemical impedance spectroscopy (EIS) over a time range of 30 days. The longer immersion time was chosen due to the big thickness of the studied coatings, which are usually applied as primers and required to exhibit superior barrier properties.

The impedance spectra of the AA2024-T3 coated with organic coatings containing different MBT@NC or MBT@SHS concentrations after 30 days immersion in 1 M NaCl are represented in the form of Bode plots in Figure 4.48 and 4.49, respectively. The spectra can be generally divided in three frequency regions (high, intermediate and low f), which correspond to different parts of the coated samples. The electrochemical response of the coating is represented at high frequencies. Thus, the observed plateaus correspond to the resistive response of the coating (R_{coat}). Relaxation processes occurring closer to the metal surface are revealed in the EIS spectra at lower frequencies. These can be associated with the native aluminum oxide layer between coating and metal surface (intermediate frequencies, C_{oxide} and R_{oxide}) and the occurrence of corrosion (low frequencies, C_{dl} and R_{ct}).

Figure 4.48 Bode plots showing the a) absolute impedance and b) phase angle as a function of frequency after 30 days immersion in 1 M NaCl of AA2024-T3 substrates coated with organic coatings containing different concentrations of MBT@NCs.
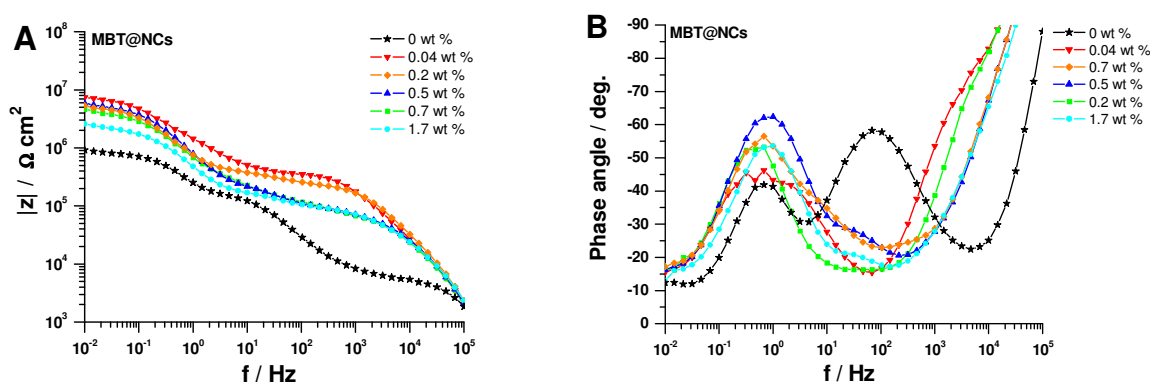
Figure 4.49 Bode plots showing the a) absolute impedance and b) phase angle as a function of frequency after 30 days immersion in 1 M NaCl of AA2024-T3 substrates coated with organic coatings containing different concentrations of MBT@SHS.
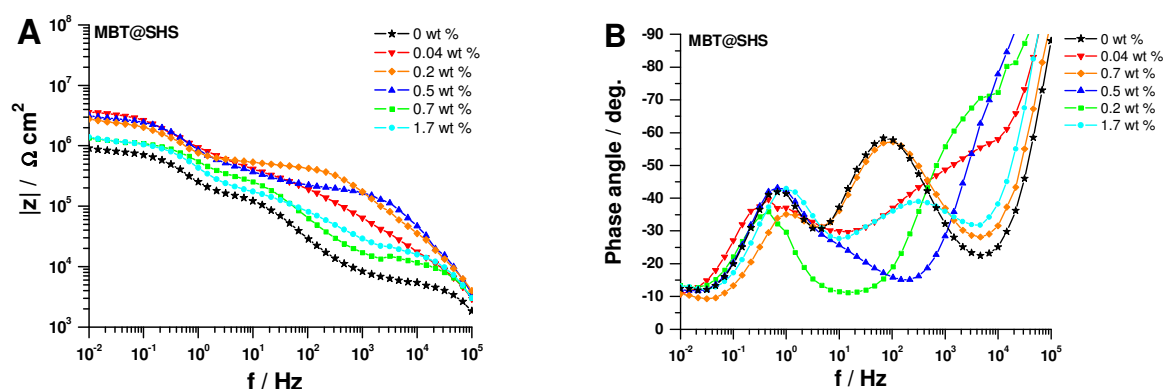
However, the ongoing corrosion causes the deterioration of the oxide layer with immersion time and suppresses its electrochemical response. Therefore, for long immersion times, the corrosion process (C_{dl} and R_{ct}) and mass transport (C_w and R_w) of corrosive species dominate the EIS spectra at lower frequencies (1 – 0.01 Hz). The measured impedance as a function of frequency combines the contributions of all these parts of the coating system and reflects its barrier properties. Accordingly, the lower |Z| measured over the whole frequency range for the coating without MBT loaded containers indicates its worse barrier properties in comparison with the modified coatings containing MBT loaded containers (Figure 4.48 and 4.49). This can be explained by the self-healing functionality of modified coatings. The protective layer formed on the metal surface by the released MBT preserves the passive functionality of the coating as a barrier and suppresses the further destructive action of corrosion. However, with increasing the concentration of embedded inhibitor, a decrease in absolute impedance was detected. The measured |Z| values for MBT@NCs and MBT@SHS concentrations above 0.5 wt % were close to the values for the control, unmodified coating. This is likely to be due to the negative effect of high amount of embedded containers or inhibitor on the coating integrity and barrier properties.

The impedance measured at the lowest frequency ($|Z|_{0.01Hz}$) reflects the corrosion resistance of the coatings (Figure 4.50a). The comparison of the values of $|Z|_{0.01Hz}$ obtained after 30 days immersion in 1 M NaCl for the coatings systems containing MBT@NCs and MBT@SHS reveals two dependencies. First, bigger size of embedded

containers leads to worse passive corrosion resistance. Second, higher concentrations of embedded containers deteriorate the coating barrier properties. In order to better understand the resistive and capacitive contributions of each part of the coating systems, the EIS spectra obtained after 30 days immersion in 1 M NaCl (Figure 4.48 and 4.49) were fitted using the equivalent circuit shown in Figure 4.50b. This equivalent circuit was chosen because of its reasonable physical meaning and fit quality ($\chi^2 \sim 0.01$). It describes very well the electrochemical response of the relaxation processes occurring in the coated samples after this long immersion time (30 days).
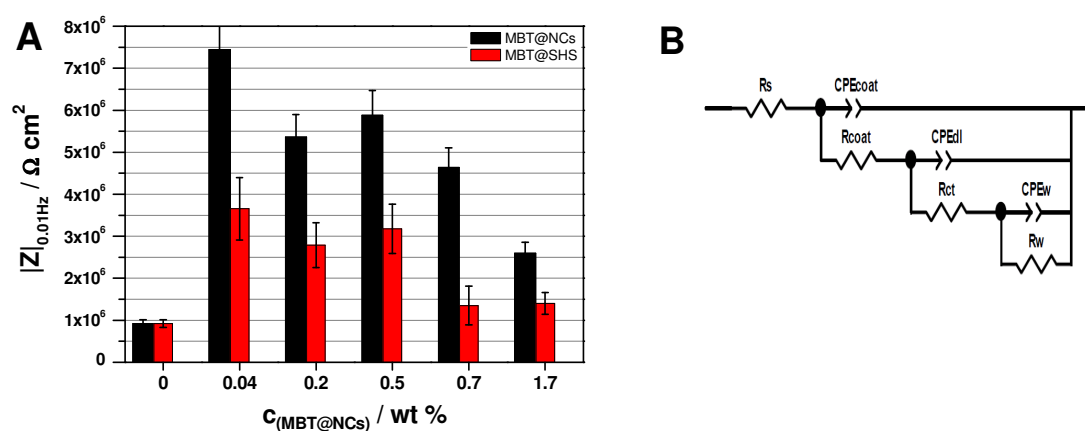
Figure 4.50 a) Impedance |Z| measured at 0.01 Hz after 30 days immersion in 1 M NaCl for organic coatings with different concentrations of MBT@NCs or MBT@SHS and b) the equivalent circuit used to fit the EIS spectra obtained after 30 days immersion in 1 M NaCl.

The obtained fitting parameters for the coating response (R_{coat} and C_{coat}) and occurrence of corrosion (R_{ct} and C_{dl}) reflect the corrosion resistance of the studied systems and are presented in Figure 4.51 and 4.52, respectively. The coating resistance reflects the presence of pores and cracks in the coating. High R_{coat} values correspond to better barrier properties, which can be due to fewer defects in the coating and/or less area of delaminated coating. The resistance of the coating without containers is almost one order of magnitude lower than for the ones with containers (Figure 4.51a). This reveals that the unmodified coating is more degraded compared to the modified coatings, which is likely to be due to the absence of active protection. Incorporating inhibitor loaded containers in the coating provides self-healing functionality but can also deteriorate the integrity of the coating matrix. This negative effect was more pronounced for the big MBT@SHS as revealed by the lower R_{coat} values, in comparison

to the R_{coat} values for MBT@NCs. This might be due to the limited adjustment of the polymer coating to bigger silica containers. This limited coating flexibility leads to the formation of more imperfect sites and diffusion pathways for the aggressive electrolyte. These facts are observed in the decreasing coating resistance with increasing MBT@NC or MBT@SHS concentration. When high amount of containers are embedded, the coatings with the smaller MBT@NCs exhibit again better barrier properties compared to the ones with MBT@SHS. This suggests a low agglomeration tendency of the MBT@NCs due to their possibly better dispersibility in the wet coating formulation and/or stronger adhesion to the dry coating matrix.
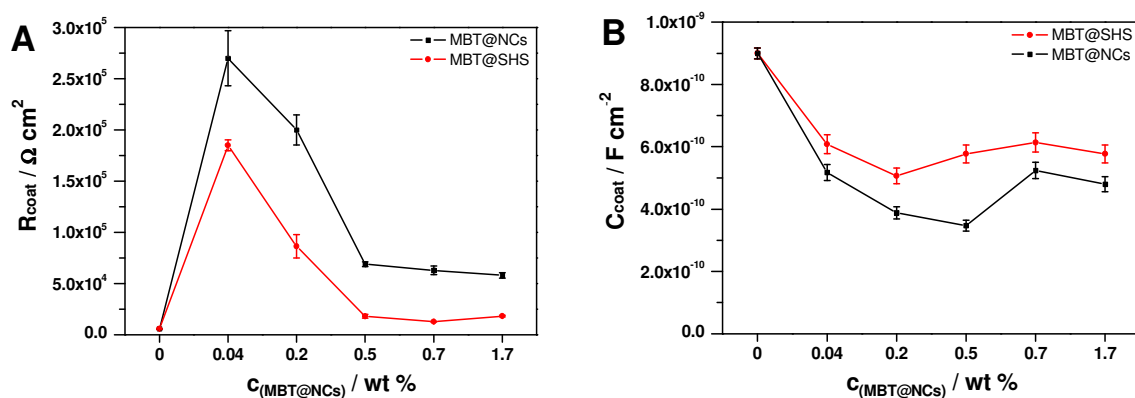
Figure 4.51 Calculated data for the a) coating resistance (R_{coat}) and b) coating capacitance (C_{coat}) obtained by fitting of the EIS spectra using the equivalent circuit shown in Figure 4.50b. EIS spectra obtained for the coating systems with MBT@NCs or MBT@SHS after 30 days immersion in 1 M NaCl were fitted.

The three time constants observed in the Bode plots (Figure 4.48b and 4.49b) correspond to phase angles that deviate from -90 °. Considering this deviation, constant phase elements (CPE) instead of capacitances were used for the fitting. The capacitance values were calculated using eq. 1 in Chapter 4.2.2.2.2.[192] The capacitance of the coating (C_{coat}) is sensitive to the water permittivity of the coating. Its dependence can be described by the simple model of a dielectric, with a capacitance C that is directly proportional to the relative dielectric constant of the coating and to the area A of the capacitor (in this case the surface area of the coating), and inversely proportional to the coating thickness d:

$$C = \frac{\varepsilon \varepsilon_0 A}{d} \qquad (2)$$

The constant ε_0 represents the dielectric constant of free space, $(8.854 \times 10^{-14}$ F cm$^{-1})$. The dielectric constant (ε) of polymers is typically in the range $3 - 8$ and of water 78.3 at 25 °C.[194] Accordingly the penetration of water in the organic coating should lead to a rise in the mixed dielectric constant, resulting in a higher capacitance. Assuming a coating thickness of 20 µm (the average thickness of the studied coatings), A of 1 cm² and a dielectric constant of 8 for an organic coating with no water content, a capacitance value of 3.5×10^{-10} F cm^{-2} is calculated. Thus, the obtained C_{coat} value of $\approx 9 \times 10^{-10}$ F cm^{-2} for the bare coating is approximately 2.5 times higher and indicates water penetration from the electrolyte into the coating during the 30 days exposure time (Figure 4.51b). The coatings with MBT@NCs exhibit lower C_{coat} for all concentrations compared to the ones with MBT@SHS. This suggests a higher water uptake for coatings containing the bigger MBT@SHS, which can be due to the higher extent of diffusion pathways and defects in these coatings. The results for coating capacitance are in agreement with the resistive response of the coating. This confirms that increasing the size and concentration of embedded containers deteriorates the coating barrier properties.

The aggressive electrolyte species accumulated in the coating diffuse to the metal surface and destroy the native oxide layer with immersion time. Thus, after 30 days immersion in 1 M NaCl the electrochemical response of the oxide layer, which usually appears at intermediate frequencies $(1 - 100$ Hz) is suppressed and replaced by the ongoing corrosion at the metal surface.[108] The corrosion rate is described by the charge transfer resistance (R_{ct}). R_{ct} reflects the kinetics of the electrochemical reactions at the interface and is directly dependent on the active corrosion inhibition. Accordingly, the higher R_{ct} values for modified coatings can be due to the embedded inhibitor and self-healing effect (Figure 4.52a). The incorporation of high amount of MBT loaded containers in the coatings compromises the coating barrier properties, as described above. This barrier effect influences the extent of corrosion and is reflected in the obtained results for R_{ct}. Thus, the lower R_{ct} values for coatings with MBT@SHS can be explained by the worse barrier properties of the coating.

The double layer capacitance (C_{dl}) is directly related to the area of metal exposed to the electrolyte. This area results from defects in the coating and increases with higher degree of coating degradation. It also provides information about the wet adhesion of the coating to the metal. Accordingly, the high C_{dl} values for the unmodified coating are due to the high extent of damage and defects in the coating (Figure 4.52b). For modified coatings, the lower values of C_{dl} compared to the unmodified one, can be attributed to the suppressed corrosion evolution provided by the self-healing ability of the coatings. The higher C_{dl} values for bigger container size and amount account for higher extent of corrosion. This can be induced by the higher degree of coating degradation or worse adhesion of the coating to the metal surface. Thus, the obtained results for C_{dl} are in agreement with the resistive response (R_{ct}) of the studied samples. Overall, the EIS study confirmed the better anticorrosion performance of the coating systems with MBT@NCs and MBT@SHS compared to the unmodified, bare organic coating. Despite the loss of barrier effect, observed for high amount or bigger embedded containers, an enhanced long-term corrosion resistance was provided due to the self-healing functionality of the modified coatings.
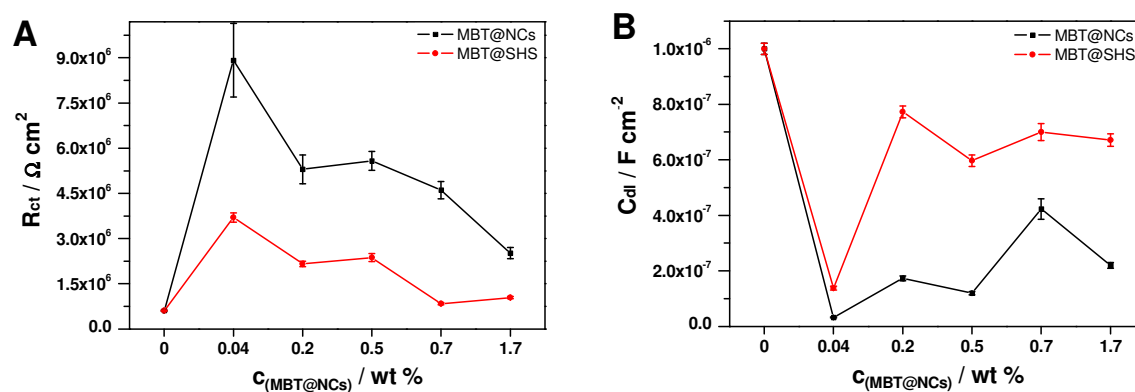

Figure 4.52 Calculated data for the a) charge transfer resistance (R_{ct}) and b) double layer capacitance (C_{dl}) obtained by fitting of the EIS spectra using the equivalent circuit shown in Figure 4.50b. EIS spectra obtained for the coating systems with MBT@NCs or MBT@SHS after 30 days immersion in 1 M NaCl were fitted.

In order to better understand the effect of embedded containers on the coating barrier properties, the contribution of active corrosion resistance needs to be excluded. Therefore, only empty containers were embedded in the organic coating. Their concentration corresponds to the container concentration in 0.5 wt % MBT@NCs and MBT@SHS. This was chosen due to the optimum overall anticorrosion performance of both coating systems containing 0.5 wt % MBT loaded containers. Additionally, MBT was incorporated directly in the organic coating to study its impact on the passive corrosion resistance. The MBT concentration is 0.1 wt % and equals the amount of MBT in 0.5 wt % MBT loaded containers, considering the MBT loading detected with TGA (20 wt %). The EIS spectra of the samples with these coatings after 30 days immersion in 1 M NaCl are shown in Figure 4.53. Lower |Z| values for all frequency regions were detected for the samples with empty containers as compared to the corresponding coatings with MBT loaded containers. This is likely to be due to the absent functionality of the coatings to actively inhibit corrosion and improve the long-term corrosion resistance. Surprisingly, the direct incorporation of MBT in the organic coating led to the worst electrochemical response, classifying this coating formulation as inefficient to inhibit corrosion on long-term.

In order to better understand the processes and their contributions to the overall electrochemical response of the studied systems, the EIS spectra shown in Figure 4.53 were fitted using the equivalent circuit shown in Figure 4.50b.
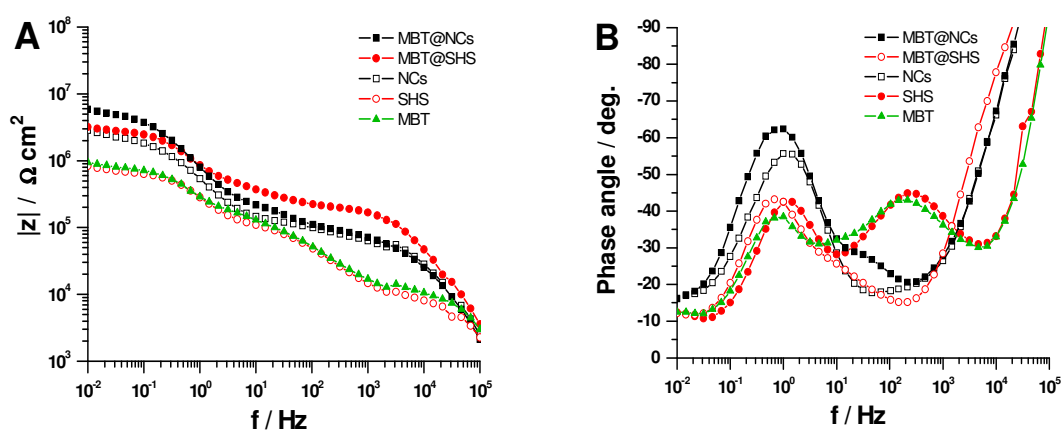

Figure 4.53 Bode plots showing the a) absolute impedance and b) phase angle as a function of frequency after 30 days immersion in 1 M NaCl of AA2024-T3 substrates coated with organic coatings doped with MBT, empty and MBT loaded silica containers (NCs or SHS).
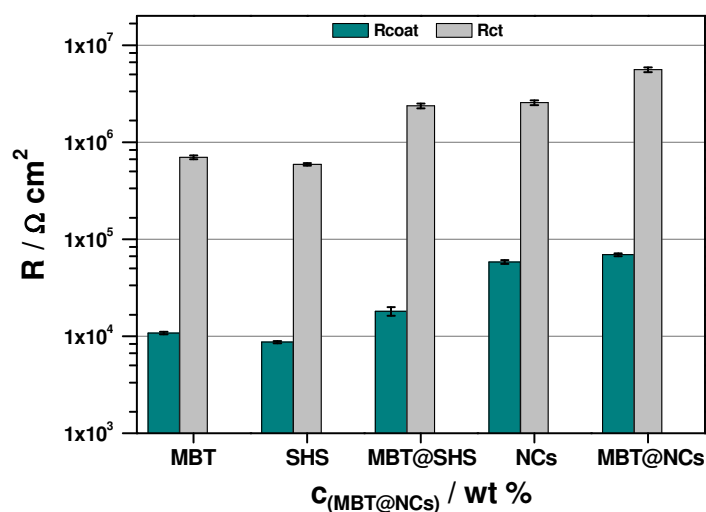
Figure 4.54 Parameters (R_{coat} and R_{ct}) obtained by fitting of the EIS spectra shown in Figure 4.53 using the equivalent circuit in Figure 4.50b.

The resistive responses of the coating (R_{coat}) and charge transfer processes (R_{ct}) were shown because these describe directly the barrier properties and extent of coating degradation. The low R_{coat} value for the coating modified with MBT suggests a detrimental effect of MBT on the coating matrix, when directly introduced into the coating. Additionally, the low R_{ct} accounts for a possible deactivation of the inhibitor, which could explain the insufficient active corrosion inhibition. Conversely, these negative effects are not observed, when the MBT does not come in a prolonged physical contact with the coating matrix. Therefore, the presence of encapsulated MBT in the coating improves the coating corrosion resistance. The R_{coat} values obtained for coatings doped with empty NCs are almost one order of magnitude higher than those for coatings with SHS. The same trend is observed also for the R_{ct} values with a difference of a factor of five. This indicates the worse effect of bigger containers on the coating barrier properties. This can be attributed to the higher stress introduced in the organic, coating matrix by bigger, embedded containers, leading to more cracks and defects. In addition, a possible poorer distribution of SHS in the coating would lead to the formation of agglomerates, which are bigger than the ones of NCs, considering the almost ten times bigger size of the SHS. Thus, more defects and heterogeneity sites are expected, when bigger containers are introduced into organic coatings.

4.2.3.2.3 Machu test

During the Machu test the coated samples with a cross-cut (3 x 3 cm² and 1 mm thick) were exposed to an aggressive, oxidative mixture with pH ≈ 3 for 48 hours.[159] This method provides a criterion for the evaluation of the extent of corrosion underneath a coating and its effect on adhesion. The length of the lateral damage underneath the coating serves as a measure of the anticorrosion efficiency. The result of the Machu test is satisfactory when no infiltration exceeding 0.5 mm on both sides of the scratch is observed. Samples fulfilling this requirement can obtain the QUALICOAT quality label. In order to evaluate the infiltration, the area with the cross-cut was scratched after the test and photographs were taken (Figure 4.55).

The samples coated with unmodified organic coating (the control sample) providing only passive protection, revealed unsatisfactory performance and the infiltration was ~ 5 mm on both sides of the scratch. The organic coatings with directly introduced MBT or empty containers (NCs and SHS) performed the worst of all studied samples, as revealed by the almost complete coating delamination around the scratched area. This indicates bad corrosion inhibition and poor adhesion of coating to metal.

Surprisingly, also for the coatings with MBT@SHS big infiltration was observed. The corrosion attack for low c(MBT@SHS) was so extensive that the coating could be easily peeled off. This is possibly due to insufficient amount of inhibitor and poor adhesion. Coatings with high c(MBT@SHS), suppressed the corrosion evolution more successfully but the infiltration was still above the required value of 0.5 mm. The failure for these can be explained by their poor barrier properties, as indicated by the darker spots revealing localized corrosion attack on the unscratched area.

Better Machu test results were obtained for the samples coated with organic coatings containing MBT@NCs. This is probably due to their self-healing functionality and better barrier properties compared to the coatings with MBT@SHS. In addition, the Machu test results, suggest the good wet adhesion of the coatings with MBT@NCs to the metal substrate. The incorporation of MBT at sufficiently high amount (c(MBT@NCs) > 0.5 wt %) leads to satisfactory overall anticorrosion performance of these coatings in the Machu test. The infiltration was measured to be below 0.5 mm on both sides of the scratch, classifying the coating systems with 0.7 wt % and 1.7 wt % MBT@NCs for the QUALICOAT quality label.

CONTROL
unmodified organic coating   **MBT**   **NCs**   **SHS**

0.04 wt %   **0.2 wt %**   **0.5 wt %**   **0.7 wt %**   **1.7 wt %**
MBT@NCs   **MBT@NCs**   **MBT@NCs**   **MBT@NCs**   **MBT@NCs**

0.04 wt %   **0.2 wt %**   **0.5 wt %**   **0.7 wt %**   **1.7 wt %**
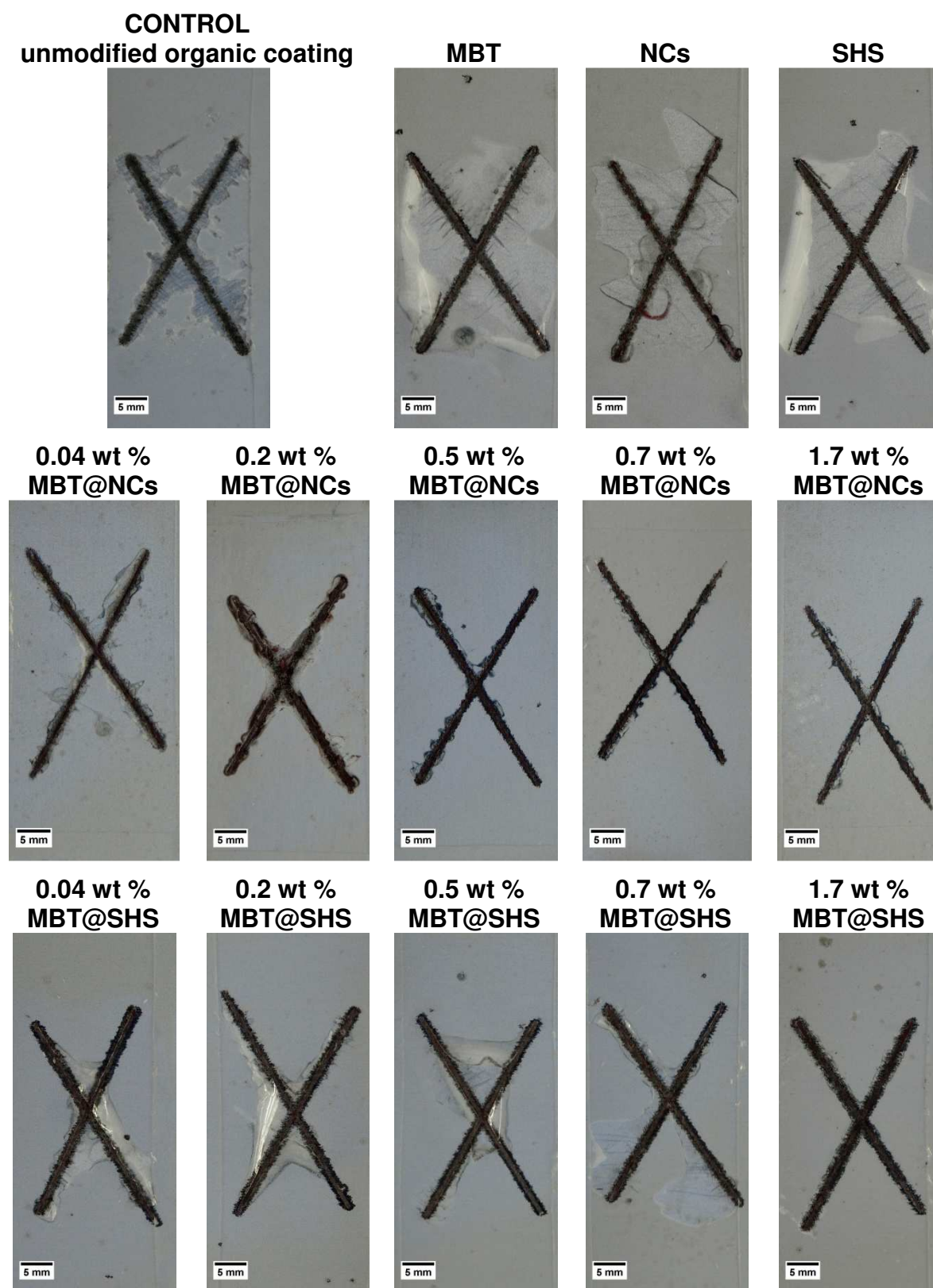**MBT@SHS**   **MBT@SHS**   **MBT@SHS**   **MBT@SHS**   **MBT@SHS**

Figure 4.55 Photographs of the coated samples tested with the Machu test for 48 hours at 37 °C in an aq. mixture of 5 % NaCl, 1 % $C_2H_4O_2$ and 0.15 % H_2O_2.

One of the important factors influencing the performance of active anticorrosive coatings based on embedded containers is the container size. In this chapter, silica containers with similar inhibitor storage capacity but different sizes ($d_1 \approx 80$ nm and $d_2 \approx 700$ nm) were embedded at different concentrations in 20 µm thick organic coatings. The obtained coating systems exhibited similar physical properties (thickness and dry adhesion) for both container types over the whole concentration range. The influence of the container size on the active and passive corrosion resistance was better pronounced. Considering the similar amounts of loaded MBT (20 wt %) in both container types, similar self-healing ability was expected. This was the case for concentrations lower than 1.7 wt %, at which the performance of coatings with bigger containers (MBT@SHS) was dominated by the worse barrier properties. The effect of container size on the coating barrier properties was better revealed by the EIS study. It was found that bigger containers deteriorate the barrier properties of the active anticorrosive coatings due to possible worse integration in the coating matrix or higher agglomeration tendency. In spite of the decrease in barrier effect, observed with inclusion of containers of bigger size or amount, a better long-term anticorrosion performance of all modified coatings compared to the unmodified one was observed due to the self-healing effect provided by the embedded MBT loaded containers.

5 Summary and conclusions

This work contributes to the design of active anticorrosive coatings, which are a subtype of feedback active coatings. The studied coatings are based on a passive coating matrix in which inhibitor (MBT) loaded mesoporous containers are dispersed. The protective coatings were applied on the industrially important aluminum alloy AA2024-T3, which is highly susceptible to localized corrosion attack.

Two types of mesoporous silica containers with different sizes (d ≈ 80 and 700 nm, respectively) were investigated in this work. The first type is mesoporous silica nanocontainers (NCs), which have spherical shape and diameters in the range between 60 and 80 nm, as revealed by SEM and TEM analysis. The NCs exhibit good aqueous colloidal stability and narrow particle size distribution, as observed with DLS measurements. The TEM images of NCs revealed a well-developed pore structure, consisting of open, disordered cylindrical pores, which are oriented from the centre to the outer surface. The total surface area determined with the BET model is ≈ 1000 m^2 g^{-1}, making the NCs promising hosts for the adsorption of guest molecules. NLDFT (non-local density functional theory) modeling yields a cumulative pore volume of ≈ 1.2 mL g^{-1} and a narrow pore size distribution with a distinct peak having a maximum at a pore diameter of 4 nm.

The second type of containers used in this work is spherical hollow silica particles (SHS), which have bigger size (600 – 700 nm) as revealed by SEM and TEM. Thus, the SHS size is almost ten times bigger than the NC size. DLS measurements revealed a slightly higher PdI but still good colloidal stability of the SHS in aqueous medium. Generally, the synthesized SHS are characterized by low polydispersity. The core-shell porous structure of SHS was revealed by TEM. The shell is around 100 nm thick with cylindrical mesopores ordered in short range parallel to each other. The core is more porous in character with disordered cage-like, round pores with diameters on the order of 25 nm. The SHS porosity yields a surface area similar to the one of the NCs (≈ 1000 m^2 g^{-1}). The shell porosity is described by a narrow pore size distribution with average pore width of ≈ 3 nm. The pore volume of the SHS was calculated to be ≈ 0.8 mL g^{-1}, which classifies the SHS as containers with high loading capacity.

The mesoporous silica containers were loaded with the nontoxic corrosion inhibitor, 2-mercaptobenzothiazole (MBT). The size of the inhibitor molecules (< 1 nm) is less than 1/3 of the diameter of the silica container pores, which makes their incorporation in the pores feasible. This assumption was confirmed by the combination of three analytical techniques (TGA, N_2 sorption and SAXS). The incorporation of high amount of MBT (20 wt %) was achieved for both container types. The MBT molecules were loaded evenly in all pores of the NCs. In contrast, a MBT accumulation only in the mesopores of the SHS shell was detected. The obtained MBT loading is much higher than previously reported for similar containers. This is due to the better encapsulation and storage properties of the studied containers. The MBT release was detected to be pH dependent. Alkaline conditions triggered the fastest and largest MBT release for both container types, which is desirable considering the high basicity at the cathodes of corroding AA2024-T3. Thus, the high amount of nontoxic inhibitor (20 wt %) stored in the mesoporous silica containers was released upon corrosion attack to provide active, on-demand corrosion inhibition. This makes the studied containers applicable wherever high uptake and controlled delivery of encapsulated molecules are required.

In addition, both container types exhibit good structural stability, which favors good inhibitor storage during the processing steps of coating preparation. In order to distribute sufficient amount of MBT loaded containers in the coating matrix, the coating should be around ten times thicker than the embedded containers. Thus, the size of the studied containers makes their incorporation in coatings with thickness > 1 µm (for NCs) and > 10 µm (for SHS) suitable.

In this work the successful embedding of MBT loaded silica containers was demonstrated. Sol-gel (SiO_x/ZrO_x) coatings with thickness of ≈ 5 µm were the host matrix for MBT@NCs and 20 µm thick organic coatings incorporated MBT@SHS and MBT@NCs. The obtained simple, anticorrosive coatings protected the underlying metal (AA2024-T3) from corrosion not only passively but also actively due to the embedded inhibitor. The anticorrosion efficiency of these coatings is influenced by several aspects of the coating design, such as: container concentration, position or size. Therefore, in order to optimize the performance of the developed coatings, the influence of these aspects was studied.

The effect of the concentration of embedded MBT@NCs was investigated in the concentration range 0.04 – 1.7 wt % and was assessed to be of high importance for the coating performance. Embedding MBT@NCs at very low concentrations (0.04 wt %) led to good passive but unsatisfactory active corrosion resistance due to an insufficient amount of available inhibitor. In contrast, too high MBT@NC concentrations (0.8 – 1.7 wt %) decreased the coating performance by deteriorating the coating barrier properties. EIS and SVET studies ranked the coating containing 0.7 wt % MBT@NCs, as the one providing the best passive and active corrosion resistance. It was found that the key to optimum overall anticorrosion performance is delivering sufficient amount of corrosion inhibitor and preserving the coating barrier properties.

Another important aspect with a strong impact on the overall performance of the studied active anticorrosive coatings is the position of the embedded MBT@NCs in the coating. In order to study the influence of the distance between the inhibitor loaded NCs and the metal surface, the same amount of MBT@NCs as used for the single layer coatings was dispersed only in half of the whole volume of the double layer coatings. When the MBT@NCs were embedded closer to the metal surface, better active corrosion resistance was detected, possibly due to the shorter distance to metal, facilitating a faster transport of released inhibitor. In comparison, better barrier properties were exhibited by double layer coatings with MBT@NCs in the top layer, suggesting a preserved coating integrity and better adhesion between coating and metal surface. In addition, it was found that the newly developed design of double layer coatings is a way to obtain enhanced anticorrosion efficiency with lower inhibitor amount. Therefore, a balance between delivering an optimal amount of corrosion inhibitor fast enough and preserving the coating barrier properties is required in order to attain satisfactory anticorrosion performance.

The influence of the size of embedded containers was studied by introducing MBT@NCs or MBT@SHS (d ≈ 80 and 700 nm, respectively) in a 20 µm thick organic coating matrix. In addition, the concentration of the embedded containers was varied (0.04 – 1.7 wt %). A self-healing effect was observed for both container types, when sufficient amount of available inhibitor was present (c(MBT) > 0.01 wt %). The active corrosion resistance was similar, which was assumed due to the same amount of loaded MBT in both container types. The negative impact of the embedded containers on the coating barrier properties was stronger pronounced for the bigger MBT@SHS. A

possible reason can be a worse dispersing of bigger particles in the organic coating matrix. This made the hybrid coating more heterogeneous and apt to build cracks acting as diffusion pathways for aggressive species. The loss in barrier effect when MBT@SHS were embedded was confirmed by the EIS results. Additionally, increasing the size of the embedded containers led to worse wet adhesion, as revealed by the Machu test results.

This work has improved the understanding of the factors influencing the overall performance of active anticorrosive coatings with embedded inhibitor loaded containers.

In conclusion, the balance between optimum barrier properties, active protection and adhesion is the key to a coating system with optimum anticorrosion efficiency.

6   References

1.   Schmitt, G.; Schütze, M.; Hays, G.F.; Burns, W.; Han, E.-H.; Pourbaix, A.; Jacobson, G. Global Needs for Knowledge Dissemination, Research, and Development in Materials Deterioration and Corrosion Control. http://www.corrosion.org/images_index/whitepaper.pdf (accessed May 2009).

2.   National Emission Standards for Hazardous Air Pollutants for Source Categories: Aerospace Manufacturing and Rework Facilities. EPA Federal Register: 1995; Vol. 60, p 45947.

3.   Twite, R.L.; Bierwagen, G.P., Review of alternatives to chromate for corrosion protection of aluminum aerospace alloys. *Progress in Organic Coatings* **1998,** 33 (2), 91-100.

4.   Hughes, A.E.; Cole, I.S.; Muster, T.H.; Varley, R.J., Designing green, self-healing coatings for metal protection. *NPG Asia Mater* **2010,** 2, 143-151.

5.   Garcia-Heras, M.; Jimenez-Morales, A.; Casal, B.; Galvan, J.C.; Radzki, S.; Villegas, M.A., Preparation and electrochemical study of cerium-silica sol-gel thin films. *Journal of Alloys and Compounds* **2004,** 380 (1-2), 219-224.

6.   Voevodin, N.N.; Grebasch, N.T.; Soto, W.S.; Arnold, F.E.; Donley, M.S., Potentiodynamic evaluation of sol–gel coatings with inorganic inhibitors. *Surface and Coatings Technology* **2001,** 140 (1), 24-28.

7.   Lvov, Y.M.; Shchukin, D.G.; Möhwald, H.; Price, R.R., Halloysite Clay Nanotubes for Controlled Release of Protective Agents. *ACS Nano* **2008,** 2 (5), 814-820.

8.   Pomorska, A.; Yliniemi, K.; Wilson, B.P.; Shchukin, D.; Johannsmann, D.; Grundmeier, G., QCM study of the adsorption of polyelectrolyte covered mesoporous TiO_2 nanocontainers on SAM modified Au surfaces. *Journal of Colloid and Interface Science* **2011,** 362 (1), 180-187.

9.   Wang, Y.; Zhang, D., Synthesis, characterization, and controlled release anticorrosion behavior of benzoate intercalated Zn–Al layered double hydroxides. *Materials Research Bulletin* **2011,** 46 (11), 1963-1968.

10.   Latnikova, A.; Grigoriev, D.O.; Hartmann, J.; Möhwald, H.; Shchukin, D.G., Polyfunctional active coatings with damage-triggered water-repelling effect. *Soft Matter* **2011,** 7 (2), 369-372.

11.   Shchukin, D.G.; Möhwald, H., Self-Repairing Coatings Containing Active Nanoreservoirs. *Small* **2007,** 3 (6), 926-943.

12.   Samadzadeh, M.; Boura, S.H.; Peikari, M.; Kasiriha, S.M.; Ashrafi, A., A review on self-healing coatings based on micro/nanocapsules. *Progress in Organic Coatings* **2010,** 68 (3), 159-164.

13.   Harvey, T.G.; Hardin, S.G.; Hughes, A.E.; Muster, T.H.; White, P.A.; Markley, T.A.; Corrigan, P.A.; Mardel, J.; Garcia, S.J.; Mol, J.M.C.; Glenn, A.M., The effect of inhibitor structure on the corrosion of AA2024 and AA7075. *Corrosion Science* **2011,** 53 (6), 2184-2190.

14.   Lamaka, S.V.; Zheludkevich, M.L.; Yasakau, K.A.; Montemor, M.F.; Ferreira, M.G.S., High effective organic corrosion inhibitors for 2024 aluminium alloy. *Electrochimica Acta* **2007,** 52 (25), 7231-7247.

15.   Ramaprasad, A., On the definition of feedback. *Behavioral Science* **1983,** 28 (1), 4-13.

16.   DiStefano, J.J.; Stubberud, A.R.; Williams, I.J., *Schaum's outline of theory and problems of feedback and control systems : continuous (analog) and discrete (digital).* McGraw-Hill: New York [etc.], **1995**.

17.   Zeigler, B.P.; Kim, T.G.; Praehofer, H., *Theory of modeling and simulation : integrating discrete event and continuous complex dynamic systems.* Acad. Press: San Diego, Calif. [u.a.], **2002**.

18.   Hall, J.E.; Guyton, A.C., *Guyton and Hall textbook of medical physiology.* Saunders Elsevier: Philadelphia, PA, **2011**.

19.   Shchukin, D.G.; Grigoriev, D.O.; Möhwald, H., Application of smart organic nanocontainers in feedback active coatings. *Soft Matter* **2010,** 6 (4), 720-725.

20.   Shchukin, D.G.; Möhwald, H., Smart nanocontainers as depot media for feedback active coatings. *Chemical Communications* **2011,** 47 (31), 8730-8739.

21. White, S.R.; Sottos, N.R.; Geubelle, P.H.; Moore, J.S.; Kessler, M.R.; Sriram, S.R.; Brown, E.N.; Viswanathan, S., Autonomic healing of polymer composites. *Nature* **2001,** 409 (6822), 794-797.

22. Ghosh, S.K., *Self-healing materials fundamentals, design strategies, and applications.* Wiley-VCH: Weinheim, **2009**.

23. Feng, W.; Patel, S.H.; Young, M.Y.; Zunino, J.L.; Xanthos, M., Smart polymeric coatings—recent advances. *Advances in Polymer Technology* **2007,** 26 (1), 1-13.

24. Brown, E.; Sottos, N.; White, S., Fracture testing of a self-healing polymer composite. *Experimental Mechanics* **2002,** 42 (4), 372-379.

25. Kessler, M.R.; Sottos, N.R.; White, S.R., Self-healing structural composite materials. *Composites Part A: Applied Science and Manufacturing* **2003,** 34 (8), 743-753.

26. Brown, E.N.; White, S.R.; Sottos, N.R., Microcapsule induced toughening in a self-healing polymer composite. *Journal of Materials Science* **2004,** 39 (5), 1703-1710.

27. Rule, J.D.; Brown, E.N.; Sottos, N.R.; White, S.R.; Moore, J.S., Wax-Protected Catalyst Microspheres for Efficient Self-Healing Materials. *Advanced Materials* **2005,** 17 (2), 205-208.

28. Sanada, K.; Yasuda, I.; Shindo, Y., Transverse tensile strength of unidirectional fibre-reinforced polymers and self-healing of interfacial debonding. *Plastics, Rubber & Composites* **2006,** 35 (2), 67-72.

29. Therriault, D.; White, S.R.; Lewis, J.A., Chaotic mixing in three-dimensional microvascular networks fabricated by direct-write assembly. *Nature Materials* **2003,** 2 (4), 265-271.

30. Kim, S.; Lorente, S.; Bejan, A., Vascularized materials: Tree-shaped flow architectures matched canopy to canopy. *Journal of Applied Physics* **2006,** 100 (6), 063525-8.

31. Keller, M.W.; White, S.R.; Sottos, N.R., A Self-Healing Poly(Dimethyl Siloxane) Elastomer. *Advanced Functional Materials* **2007,** 17 (14), 2399-2404.

32. Caruso, M.M.; Blaiszik, B.J.; White, S.R.; Sottos, N.R.; Moore, J.S., Full Recovery of Fracture Toughness Using a Nontoxic Solvent-Based Self-Healing System. *Advanced Functional Materials* **2008,** 18 (13), 1898-1904.

33. Blaiszik, B.J.; Caruso, M.M.; McIlroy, D.A.; Moore, J.S.; White, S.R.; Sottos, N.R., Microcapsules filled with reactive solutions for self-healing materials. *Polymer* **2009,** 50 (4), 990-997.

34. He, X.; Shi, X., Self-repairing coating for corrosion protection of aluminum alloys. *Progress in Organic Coatings* **2009,** 65 (1), 37-43.

35. Liu Harvey, A.; Gnade Bruce, E.; Balkus Kenneth, J., Preparation of a Delivery System for Smart Coatings by Electrostatic Deposition. In *Smart Coatings III*, American Chemical Society: **2010**; Vol. 1050, pp 31-44.

36. Suryanarayana, C.; Rao, K.C.; Kumar, D., Preparation and characterization of microcapsules containing linseed oil and its use in self-healing coatings. *Progress in Organic Coatings* **2008,** 63 (1), 72-78.

37. Alexandridou, S.; Kiparissides, C.; Fransaer, J.; Celis, J.P., On the synthesis of oil-containing microcapsules and their electrolytic codeposition. *Surface and Coatings Technology* **1995,** 71 (3), 267-276.

38. Liqun, Z.; Wei, Z.; Feng, L.; He, Y., Electrodeposition of composite copper/liquid-containing microcapsule coatings. *Journal of Materials Science* **2004,** 39 (2), 495-499.

39. Rule, J.D.; Sottos, N.R.; White, S.R., Effect of microcapsule size on the performance of self-healing polymers. *Polymer* **2007,** 48 (12), 3520-3529.

40. Johns, K., Hygienic coatings: The next generation. *Surface Coatings International Part B: Coatings Transactions* **2003,** 86 (2), 101-110.

41. Tiller, J.C.; Liao, C.J.; Lewis, K.; Klibanov, A.M., Designing surfaces that kill bacteria on contact. *Proceedings of the National Academy of Sciences of the United States of America* **2001,** 98 (11), 5981-5985.

42. Kim, J.-C.; Song, M.-E.; Lee, E.-J.; Park, S.-k.; Rang, M.-J.; Ahn, H.-J., Preparation and Characterization of Triclosan-Containing Microcapsules by Complex Coacervation. *Journal of Dispersion Science and Technology* **2001,** 22 (6), 591-596.

43. Edge, M.; Allen, N.S.; Turner, D.; Robinson, J.; Seal, K., The enhanced performance of biocidal additives in paints and coatings. *Progress in Organic Coatings* **2001,** 43 (1–3), 10-17.

44. Worley, S.D.; Li, F.; Wu, R.; Kim, J.; Wei, C.I.; Williams, J.F.; Owens, J.R.; Wander, J.D.; Bargmeyer, A.M.; Shirtliff, M.E., A novel N-halamine monomer for preparing biocidal polyurethane coatings. *Surface Coatings International Part B: Coatings Transactions* **2003,** 86 (4), 273-277.

45. Alistagen Corporation website https://www.alistagen.com/products.htm.

46. Pérez, M.; García, M.; del Amo, B.; Blustein, G.; Stupak, M., Core-shell pigments in antifouling paints. *Surface Coatings International Part B: Coatings Transactions* **2003,** 86 (4), 259-262.

47. Geiger, T.; Delavy, P.; Hany, R.; Schleuniger, J.; Zinn, M., Encapsulated Zosteric Acid Embedded in Poly[3-hydroxyalkanoate] Coatings—Protection against Biofouling. *Polymer Bulletin* **2004,** 52 (1), 65-72.

48. Bédard, M.F.; De Geest, B.G.; Skirtach, A.G.; Möhwald, H.; Sukhorukov, G.B., Polymeric microcapsules with light responsive properties for encapsulation and release. *Advances in Colloid and Interface Science* **2010,** 158 (1–2), 2-14.

49. Nakajima, A.; Hashimoto, K.; Watanabe, T.; Takai, K.; Yamauchi, G.; Fujishima, A., Transparent Superhydrophobic Thin Films with Self-Cleaning Properties. *Langmuir* **2000,** 16 (17), 7044-7047.

50. Guan, K., Relationship between photocatalytic activity, hydrophilicity and self-cleaning effect of TiO2/SiO2 films. *Surface and Coatings Technology* **2005,** 191 (2–3), 155-160.

51. Parkin, I.P.; Palgrave, R.G., Self-cleaning coatings. *Journal of Materials Chemistry* **2005,** 15 (17), 1689-1695.

52. Zhang, X.-T.; Sato, O.; Taguchi, M.; Einaga, Y.; Murakami, T.; Fujishima, A., Self-Cleaning Particle Coating with Antireflection Properties. *Chemistry of Materials* **2005,** 17 (3), 696-700.

53. Malcher, M.; Volodkin, D.; Heurtault, B.a.; André, P.; Schaaf, P.; Möhwald, H.; Voegel, J.-C.; Sokolowski, A.; Ball, V.; Boulmedais, F.; Frisch, B., Embedded Silver Ions-Containing Liposomes in Polyelectrolyte Multilayers: Cargos Films for Antibacterial Agents. *Langmuir* **2008,** 24 (18), 10209-10215.

54.   Volodkin, D.; Arntz, Y.; Schaaf, P.; Möhwald, H.; Voegel, J.-C.; Ball, V., Composite multilayered biocompatible polyelectrolyte films with intact liposomes: stability and temperature triggered dye release. *Soft Matter* **2008,** 4 (1), 122-130.

55.   Kulkarni, R.V.; Biswanath, S., Electrically responsive smart hydrogels in drug delivery: a review. *Journal of Applied Biomaterials & Biomechanics* **2007,** 5 (3), 125-139.

56.   Veerabadran, N.G.; Price, R.R.; Lvov, Y.M., Clay nanotubes for encapsulation and sustained release of drugs. *Nano* **2007,** 2 (2), 115-120.

57.   Lin, C.-C.; Metters, A.T., Hydrogels in controlled release formulations: Network design and mathematical modeling. *Advanced Drug Delivery Reviews* **2006,** 58 (12–13), 1379-1408.

58.   Shchukin, D.G.; Sukhorukov, G.B., Nanoparticle Synthesis in Engineered Organic Nanoscale Reactors. *Advanced Materials* **2004,** 16 (8), 671-682.

59.   Mehta, S.; Kaur, G.; Bhasin, K., Incorporation of Antitubercular Drug Isoniazid in Pharmaceutically Accepted Microemulsion: Effect on Microstructure and Physical Parameters. *Pharmaceutical Research* **2008,** 25 (1), 227-236.

60.   Köhler, K.; Shchukin, D.G.; Möhwald, H.; Sukhorukov, G.B., Thermal Behavior of Polyelectrolyte Multilayer Microcapsules. 1. The Effect of Odd and Even Layer Number. *The Journal of Physical Chemistry B* **2005,** 109 (39), 18250-18259.

61.   Antipov, A.A.; Sukhorukov, G.B., Polyelectrolyte multilayer capsules as vehicles with tunable permeability. *Advances in Colloid and Interface Science* **2004,** 111 (1–2), 49-61.

62.   Shchukin, D.G.; Köhler, K.; Möhwald, H., Microcontainers with Electrochemically Reversible Permeability. *Journal of the American Chemical Society* **2006,** 128 (14), 4560-4561.

63.   Kozlovskaya, V.; Shamaev, A.; Sukhishvili, S.A., Tuning swelling pH and permeability of hydrogel multilayer capsules. *Soft Matter* **2008,** 4 (7), 1499-1507.

64.   Kharlampieva, E.; Erel-Unal, I.; Sukhishvili, S.A., Amphoteric Surface Hydrogels Derived from Hydrogen-Bonded Multilayers: Reversible Loading of Dyes and Macromolecules†. *Langmuir* **2006,** 23 (1), 175-181.

65.   Davis, J.R., *Corrosion : understanding the basics.* ASM International: Materials Park, Ohio, **2000**.

66.   Fontana, M.G.; Greene, N.D., *Corrosion engineering.* McGraw-Hill: New York, **1967**.

67.   Schweitzer, P.A., *Corrosion engineering handbook. atmospheric and media corrosion of metals Fundamentals of metallic corrosion.* CRC Press: Boca Raton, **2007**.

68.   Pepe, A.; Aparicio, M.; Ceré, S.; Durán, A., Preparation and characterization of cerium doped silica sol–gel coatings on glass and aluminum substrates. *Journal of Non-Crystalline Solids* **2004,** 348 (0), 162-171.

69.   Frankel, G.S., Pitting corrosion of metals - A review of the critical factors. *Journal of The Electrochemical Society* **1998,** 145 (6), 2186-2198.

70.   Ghali, E., *Corrosion resistance of aluminum and magnesium alloys understanding, performance, and testing.* John Wiley: Hoboken, N.J., **2010**.

71.   Buchheit, R.G.; Grant, R.P.; Hlava, P.F.; McKenzie, B.; Zender, G.L., Local dissolution phenomena associated with S phase (Al2CuMg) particles in aluminum alloy 2024-T3. *Journal of The Electrochemical Society* **1997,** 144 (8), 2621-2628.

72.   Bucci, R.J.; Warren, C.J.; Starke, E.A., Need for new materials in aging aircraft structures. *Journal of Aircraft* **2000,** 37 (1), 122-129.

73.   Hughes, A.E.; MacRae, C.; Wilson, N.; Torpy, A.; Muster, T.H.; Glenn, A.M., Sheet AA2024-T3: a new investigation of microstructure and composition. *Surface and Interface Analysis* **2010,** 42 (4), 334-338.

74.   Boag, A.; Taylor, R.J.; Muster, T.H.; Goodman, N.; McCulloch, D.; Ryan, C.; Rout, B.; Jamieson, D.; Hughes, A.E., Stable pit formation on AA2024-T3 in a NaCl environment. *Corrosion Science* **2010,** 52 (1), 90-103.

75.   Boag, A.; Hughes, A.E.; Glenn, A.M.; Muster, T.H.; McCulloch, D., Corrosion of AA2024-T3 Part I: Localised corrosion of isolated IM particles. *Corrosion Science* **2011,** 53 (1), 17-26.

76.   Hughes, A.E.; Boag, A.; Glenn, A.M.; McCulloch, D.; Muster, T.H.; Ryan, C.; Luo, C.; Zhou, X.; Thompson, G.E., Corrosion of AA2024-T3 Part II: Co-operative corrosion. *Corrosion Science* **2011,** 53 (1), 27-39.

77.   Glenn, A.M.; Muster, T.H.; Luo, C.; Zhou, X.; Thompson, G.E.; Boag, A.; Hughes, A.E., Corrosion of AA2024-T3 Part III: Propagation. *Corrosion Science* **2011,** 53 (1), 40-50.

78.   García, S.J.; Muster, T.H.; Özkanat, Ö.; Sherman, N.; Hughes, A.E.; Terryn, H.; de Wit, J.H.W.; Mol, J.M.C., The influence of pH on corrosion inhibitor selection for 2024-T3 aluminium alloy assessed by high-throughput multielectrode and potentiodynamic testing. *Electrochimica Acta* **2010,** 55 (7), 2457-2465.

79.   Hare, C.H., A review of inhibitive metal primers. *Modern Paint and Coatings* **1996,** 86 (7), 26-33.

80.   Magnussen, O., Corrosion protection by inhibition. *Encyclopedia of electrochemistry* **2002,** 4, 435-459.

81.   McCafferty, E., Thermodynamics of chromate replacements by various homologous transition metal oxyanions. *Journal of Applied Electrochemistry* **2010,** 40 (3), 543-549.

82.   Aldykewicz, A.J.; Isaacs, H.S.; Davenport, A.J., The Investigation of Cerium as a Cathodic Inhibitor for Aluminum-Copper Alloys. *Journal of The Electrochemical Society* **1995,** 142 (10), 3342-3350.

83.   Hinton, B.R.W., Corrosion inhibition with rare earth metal salts. *Journal of Alloys and Compounds* **1992,** 180 (1–2), 15-25.

84.   Sanyal, B., Organic Compounds as Corrosion Inhibitors in Different Environments - A Review. *Progress in Organic Coatings* **1981,** 9 (2), 165-236.

85.   Casenave, C.; Pebere, N.; Dabosi, F., An electrochemical impedance study of the corrosion inhibition of a 2024 aluminum alloy in neutral chloride solutions. *Materials Science Forum* **1995,** 192-194, 599-610.

86.   Garrigues, L.; Pebere, N.; Dabosi, F., An investigation of the corrosion inhibition of pure aluminum in neutral and acidic chloride solutions. *Electrochimica Acta* **1996,** 41 (7–8), 1209-1215.

87.   Zheludkevich, M.L.; Yasakau, K.A.; Poznyak, S.K.; Ferreira, M.G.S., Triazole and thiazole derivatives as corrosion inhibitors for AA2024 aluminium alloy. *Corrosion Science* **2005,** 47 (12), 3368-3383.

88. Trachli, B.; Keddam, M.; Takenouti, H.; Srhiri, A., Protective effect of electropolymerized 2-mercaptobenzimidazole upon copper corrosion. *Progress in Organic Coatings* **2002,** 44 (1), 17-23.

89. van Ooij, W.J.; Zhu, D.Q.; Prasad, G.; Jayaseelan, S.; Fu, Y.; Teredesai, N., Silane based chromate replacements for corrosion control, paint adhesion, and rubber bonding. *Surface Engineering* **2000,** 16 (5), 386-396.

90. Zheludkevich, M.L.; Serra, R.; Montemor, M.F.; Salvado, I.M.M.; Ferreira, M.G.S., Corrosion protective properties of nanostructured sol-gel hybrid coatings to AA2024-T3. *Surface & Coatings Technology* **2006,** 200 (9), 3084-3094.

91. Sørensen, P.; Kiil, S.; Dam-Johansen, K.; Weinell, C., Anticorrosive coatings: a review. *Journal of Coatings Technology and Research* **2009,** 6 (2), 135-176.

92. Broek, A.D., Environment-friendly paints: their technical (im)possibilities. *Progress in Organic Coatings* **1993,** 22 (1–4), 55-68.

93. Raps, D.; Hack, T.; Wehr, J.; Zheludkevich, M.L.; Bastos, A.C.; Ferreira, M.G.S.; Nuyken, O., Electrochemical study of inhibitor-containing organic-inorganic hybrid coatings on AA2024. *Corrosion Science* **2009,** 51 (5), 1012-1021.

94. Palanivel, V.; Huang, Y.; van Ooij, W.J., Effects of addition of corrosion inhibitors to silane films on the performance of AA2024-T3 in a 0.5 M NaCl solution. *Progress in Organic Coatings* **2005,** 53 (2), 153-168.

95. Yasakau, K.A.; Zheludkevich, M.L.; Karavai, O.V.; Ferreira, M.G.S., Influence of inhibitor addition on the corrosion protection performance of sol–gel coatings on AA2024. *Progress in Organic Coatings* **2008,** 63 (3), 352-361.

96. Raps, D.; Hack, T.; Wehr, J.; Zheludkevich, M.L.; Bastos, A.C.; Ferreira, M.G.S.; Nuyken, O., Electrochemical study of inhibitor-containing organic–inorganic hybrid coatings on AA2024. *Corrosion Science* **2009,** 51 (5), 1012-1021.

97. Cho, S.H.; White, S.R.; Braun, P.V., Self-Healing Polymer Coatings. *Advanced Materials* **2009,** 21 (6), 645-649.

98. Szabó, T.; Molnár-Nagy, L.; Bognár, J.; Nyikos, L.; Telegdi, J., Self-healing microcapsules and slow release microspheres in paints. *Progress in Organic Coatings* **2011,** 72 (1–2), 52-57.

99.   Latnikova, A.; Grigoriev, D.; Schenderlein, M.; Möhwald, H.; Shchukin, D., A new approach towards "active" self-healing coatings: exploitation of microgels. *Soft Matter* **2012**.

100. Rosero-Navarro, N.; Pellice, S.; Durán, A.; Ceré, S.; Aparicio, M., Corrosion protection of aluminium alloy AA2024 with cerium doped methacrylate-silica coatings. *Journal of Sol-Gel Science and Technology* **2009,** 52 (1), 31-40.

101. Szunerits, S.; Walt, D.R., Aluminum Surface Corrosion and the Mechanism of Inhibitors Using pH and Metal Ion Selective Imaging Fiber Bundles. *Analytical Chemistry* **2002,** 74 (4), 886-894.

102. Buchheit, R.G.; Mamidipally, S.B.; Schmutz, P.; Guan, H., Active corrosion protection in Ce-modified hydrotalcite conversion coatings. *CORROSION* **2002,** 58 (1), 3-14.

103. Williams, G.; McMurray, H.N., Inhibition of Filiform Corrosion on Polymer Coated AA2024-T3 by Hydrotalcite-Like Pigments Incorporating Organic Anions. *Electrochemical and Solid-State Letters* **2004,** 7 (5), B13-B15.

104. Decher, G.; Hong, J.D.; Schmitt, J., Buildup of ultrathin multilayer films by a self-assembly process: III. Consecutively alternating adsorption of anionic and cationic polyelectrolytes on charged surfaces. *Thin Solid Films* **1992,** 210–211, Part 2 (0), 831-835.

105. Sukhorukov, G.B.; Rogach, A.L.; Zebli, B.; Liedl, T.; Skirtach, A.G.; Kohler, K.; Antipov, A.A.; Gaponik, N.; Susha, A.S.; Winterhalter, M.; Parak, W.J., Nanoengineered polymer capsules: Tools for detection, controlled delivery, and site-specific manipulation. *Small* **2005,** 1 (2), 194-200.

106. Neu, B.; Voigt, A.; Mitlohner, R.; Leporatti, S.; Gao, C.Y.; Donath, E.; Kiesewetter, H.; Möhwald, H.; Meiselman, H.J.; Baumler, H., Biological cells as templates for hollow microcapsules. *Journal of Microencapsulation* **2001,** 18 (3), 385-395.

107. Shchukin, D.G.; Sukhorukov, G.B.; Möhwald, H., Smart Inorganic/Organic Nanocomposite Hollow Microcapsules. *Angewandte Chemie International Edition* **2003,** 42 (37), 4472-4475.

108. Zheludkevich, M.L.; Shchukin, D.G.; Yasakau, K.A.; Möhwald, H.; Ferreira, M.G.S., Anticorrosion Coatings with Self-Healing Effect Based on Nanocontainers

Impregnated with Corrosion Inhibitor. *Chemistry of Materials* **2007,** 19 (3), 402-411.

109. Shchukin, D.G.; Zheludkevich, M.; Yasakau, K.; Lamaka, S.; Ferreira, M.G.S.; Möhwald, H., Layer-by-layer assembled nanocontainers for self-healing corrosion protection. *Advanced Materials* **2006,** 18 (13), 1672-+.

110. Grigoriev, D.O.; Kohler, K.; Skorb, E.; Shchukin, D.G.; Möhwald, H., Polyelectrolyte complexes as a "smart'' depot for self-healing anticorrosion coatings. *Soft Matter* **2009,** 5 (7), 1426-1432.

111. Skorb, E.V.; Skirtach, A.G.; Sviridov, D.V.; Shchukin, D.G.; Möhwald, H., Laser-Controllable Coatings for Corrosion Protection. *ACS Nano* **2009,** 3 (7), 1753-1760.

112. Skorb, E.V.; Sviridov, D.V.; Möhwald, H.; Shchukin, D.G., Light responsive protective coatings. *Chemical Communications* **2009,** (40), 6041-6043.

113. Skorb, E.V.; Fix, D.; Andreeva, D.V.; Möhwald, H.; Shchukin, D.G., Surface-Modified Mesoporous SiO_2 Containers for Corrosion Protection. *Advanced Functional Materials* **2009,** 19 (15), 2373-2379.

114. Shchukin, D.G.; Möhwald, H., Surface-engineered nanocontainers for entrapment of corrosion inhibitors. *Advanced Functional Materials* **2007,** 17 (9), 1451-1458.

115. Shchukin, D.G.; Lamaka, S.V.; Yasakau, K.A.; Zheludkevich, M.L.; Ferreira, M.G.S.; Möhwald, H., Active anticorrosion coatings with halloysite nanocontainers. *Journal of Physical Chemistry C* **2008,** 112 (4), 958-964.

116. Abdullayev, E.; Price, R.; Shchukin, D.; Lvov, Y., Halloysite Tubes as Nanocontainers for Anticorrosion Coating with Benzotriazole. *ACS Applied Materials & Interfaces* **2009,** 1 (7), 1437-1443.

117. Abdullayev, E.; Lvov, Y., Clay nanotubes for corrosion inhibitor encapsulation: release control with end stoppers. *Journal of Materials Chemistry* **2010,** 20 (32), 6681-6687.

118. Fix, D.; Andreeva, D.V.; Lvov, Y.M.; Shchukin, D.G.; Möhwald, H., Application of Inhibitor-Loaded Halloysite Nanotubes in Active Anti-Corrosive Coatings. *Advanced Functional Materials* **2009,** 19 (11), 1720-1727.

119. Balaskas, A.C.; Kartsonakis, I.A.; Tziveleka, L.A.; Kordas, G.C., Improvement of anti-corrosive properties of epoxy-coated AA2024-T3 with TiO_2 nanocontainers loaded with 8-hydroxyquinoline. *Progress in Organic Coatings* **2012,** 74 (3), 418-426.

120. Hollamby, M.J.; Fix, D.; Dönch, I.; Borisova, D.; Möhwald, H.; Shchukin, D., Hybrid Polyester Coating Incorporating Functionalized Mesoporous Carriers for the Holistic Protection of Steel Surfaces. *Advanced Materials* **2011,** 23 (11), 1361-1365.

121. Maia, F.; Tedim, J.; Lisenkov, A.D.; Salak, A.N.; Zheludkevich, M.L.; Ferreira, M.G.S., Silica nanocontainers for active corrosion protection. *Nanoscale* **2012,** 4 (4), 1287-1298.

122. Haase, M.F.; Grigoriev, D.O.; Möhwald, H.; Shchukin, D.G., Development of Nanoparticle Stabilized Polymer Nanocontainers with High Content of the Encapsulated Active Agent and Their Application in Water-Borne Anticorrosive Coatings. *Advanced Materials* **2012,** 24 (18), 2429-2435.

123. Borisova, D.; Möhwald, H.; Shchukin, D.G., Mesoporous Silica Nanoparticles for Active Corrosion Protection. *ACS Nano* **2011,** 5 (3), 1939-1946.

124. Borisova, D.; Möhwald, H.; Shchukin, D.G., Influence of Embedded Nanocontainers on the Efficiency of Active Anticorrosive Coatings for Aluminum Alloys Part I: Influence of Nanocontainer Concentration. *ACS Applied Materials & Interfaces* **2012,** 4 (6), 2931-2939.

125. Hollamby, M.J.; Borisova, D.; Möhwald, H.; Shchukin, D., Porous 'Ouzo-effect' silica-ceria composite colloids and their application to aluminium corrosion protection. *Chemical Communications* **2012,** 48 (1), 115-117.

126. Everett, D.H., Manual of Symbols and Terminology for Physicochemical Quantities and Units, Appendix II: Definitions, Terminology and Symbols in Colloid and Surface Chemistry. *Pure Appl. Chem.* **1972**, 577-638.

127. Bryskhe, K.; Bulut, S.; Olsson, U., Vesicle formation from temperature jumps in a nonionic surfactant system. *Journal of Physical Chemistry B* **2005,** 109 (19), 9265-9274.

128. Hoffmann, F.; Cornelius, M.; Morell, J.; Fröba, M., Silica-Based Mesoporous Organic–Inorganic Hybrid Materials. *Angewandte Chemie International Edition* **2006,** 45 (20), 3216-3251.

129. Cai, Q.; Luo, Z.S.; Pang, W.Q.; Fan, Y.W.; Chen, X.H.; Cui, F.Z., Dilute solution routes to various controllable morphologies of MCM-41 silica with a basic medium. *Chemistry of Materials* **2001,** 13 (2), 258-263.

130. Iler, R.K., *The chemistry of silica : solubility, polymerization, colloid and surface properties, and biochemistry.* Wiley: New York, **1979**.

131. Kleitz, F.; Schmidt, W.; Schuth, F., Calcination behavior of different surfactant-templated mesostructured silica materials. *Microporous and Mesoporous Materials* **2003,** 65 (1), 1-29.

132. Fulvio, P.F.; Grabicka, B.E.; Grudzien, R.M.; Jaroniec, M., Effects of hydrothermal treatment and template removal on the adsorption and structural properties of SBA-16 mesoporous silica. *Adsorption Science & Technology* **2007,** 25 (6), 439-449.

133. Slowing, I.I.; Vivero-Escoto, J.L.; Trewyn, B.G.; Lin, V.S.Y., Mesoporous silica nanoparticles: structural design and applications. *Journal of Materials Chemistry* **2010,** 20 (37), 7924-7937.

134. Kecht, J.; Schlossbauer, A.; Bein, T., Selective Functionalization of the Outer and Inner Surfaces in Mesoporous Silica Nanoparticles. *Chemistry of Materials* **2008,** 20 (23), 7207-7214.

135. Ren, J.; Ding, J.; Chan, K.-Y.; Wang, H., Dual-Porosity Carbon Templated from Monosize Mesoporous Silica Nanoparticles. *Chemistry of Materials* **2007,** 19 (11), 2786-2795.

136. Boissière, C.; Kümmel, M.; Persin, M.; Larbot, A.; Prouzet, E., Spherical MSU-1 Mesoporous Silica Particles Tuned for HPLC. *Advanced Functional Materials* **2001,** 11 (2), 129-135.

137. Lu, J.; Liong, M.; Zink, J.I.; Tamanoi, F., Mesoporous silica nanoparticles as a delivery system for hydrophobic anticancer drugs. *Small* **2007,** 3 (8), 1341-1346.

138. Liu, X.; Li, J.; Zhou, L.; Huang, D.; Zhou, Y., Adsorption of CO_2, CH_4 and N_2 on ordered mesoporous silica molecular sieve. *Chemical Physics Letters* **2005,** 415 (4–6), 198-201.

139. Möller, K.; Bein, T., Inclusion Chemistry in Periodic Mesoporous Hosts. *Chemistry of Materials* **1998,** 10 (10), 2950-2963.

140. Stein, A.; Melde, B.J.; Schroden, R.C., Hybrid inorganic-organic mesoporous silicates - Nanoscopic reactors coming of age. *Advanced Materials* **2000,** 12 (19), 1403-1419.

141. Cardin, D.J.; Constantine, S.P.; Gilbert, A.; Lay, A.K.; Alvaro, M.; Galletero, M.S.; Garcia, H.; Marquez, F., Polymerization of Alkynes in the Channels of Mesoporous Materials Containing Ni and Zn Cations: Almost Complete Filling of the Voids. *Journal of the American Chemical Society* **2001,** 123 (13), 3141-3142.

142. Lin, V.S.Y.; Radu, D.R.; Han, M.-K.; Deng, W.; Kuroki, S.; Shanks, B.H.; Pruski, M., Oxidative Polymerization of 1,4-Diethynylbenzene into Highly Conjugated Poly(phenylene butadiynylene) within the Channels of Surface-Functionalized Mesoporous Silica and Alumina Materials. *Journal of the American Chemical Society* **2002,** 124 (31), 9040-9041.

143. Wu, C.-G.; Bein, T., Conducting Carbon Wires in Ordered, Nanometer-Sized Channels. *Science* **1994,** 266 (5187), 1013-1015.

144. Schlossbauer, A.; Kecht, J.; Bein, T., Biotin-Avidin as a Protease-Responsive Cap System for Controlled Guest Release from Colloidal Mesoporous Silica. *Angewandte Chemie-International Edition* **2009,** 48 (17), 3092-3095.

145. Fukuoka, A.; Fujishima, K.; Chiba, M.; Yamagishi, A.; Inagaki, S.; Fukushima, Y.; Ichikawa, M., Photooxidation of cyclohexene and benzene with oxygen by fullerenes grafted on mesoporous FSM-16. *Catalysis Letters* **2000,** 68 (3), 241-244.

146. Díaz, J.F.; Balkus Jr, K.J., Enzyme immobilization in MCM-41 molecular sieve. *Journal of Molecular Catalysis B: Enzymatic* **1996,** 2 (2–3), 115-126.

147. Rosenholm, J.M.; Lindén, M., Towards establishing structure–activity relationships for mesoporous silica in drug delivery applications. *Journal of Controlled Release* **2008,** 128 (2), 157-164.

148. Cauda, V.; Argyo, C.; Schlossbauer, A.; Bein, T., Controlling the delivery kinetics from colloidal mesoporous silica nanoparticles with pH-sensitive gates. *Journal of Materials Chemistry* **2010,** 20 (21), 4305-4311.

149. Yang, Q.; Wang, S.; Fan, P.; Wang, L.; Di, Y.; Lin, K.; Xiao, F.-S., pH-Responsive Carrier System Based on Carboxylic Acid Modified Mesoporous Silica and Polyelectrolyte for Drug Delivery. *Chemistry of Materials* **2005,** 17 (24), 5999-6003.

150. Lai, C.-Y.; Trewyn, B.G.; Jeftinija, D.M.; Jeftinija, K.; Xu, S.; Jeftinija, S.; Lin, V.S.Y., A Mesoporous Silica Nanosphere-Based Carrier System with Chemically Removable CdS Nanoparticle Caps for Stimuli-Responsive Controlled Release of Neurotransmitters and Drug Molecules. *Journal of the American Chemical Society* **2003,** 125 (15), 4451-4459.

151. Giri, S.; Trewyn, B.G.; Stellmaker, M.P.; Lin, V.S.Y., Stimuli-Responsive Controlled-Release Delivery System Based on Mesoporous Silica Nanorods Capped with Magnetic Nanoparticles. *Angewandte Chemie International Edition* **2005,** 44 (32), 5038-5044.

152. Mal, N.K.; Fujiwara, M.; Tanaka, Y., Photocontrolled reversible release of guest molecules from coumarin-modified mesoporous silica. *Nature* **2003,** 421 (6921), 350-353.

153. Zhao, Y.; Trewyn, B.G.; Slowing, I.I.; Lin, V.S.Y., Mesoporous Silica Nanoparticle-Based Double Drug Delivery System for Glucose-Responsive Controlled Release of Insulin and Cyclic AMP. *Journal of the American Chemical Society* **2009,** 131 (24), 8398-8400.

154. Schlossbauer, A.; Kecht, J.; Bein, T., Biotin–Avidin as a Protease-Responsive Cap System for Controlled Guest Release from Colloidal Mesoporous Silica. *Angewandte Chemie International Edition* **2009,** 48 (17), 3092-3095.

155. Möller, K.; Kobler, J.; Bein, T., Colloidal Suspensions of Nanometer-Sized Mesoporous Silica. *Advanced Functional Materials* **2007,** 17 (4), 605-612.

156. Teng, Z.; Han, Y.; Li, J.; Yan, F.; Yang, W., Preparation of hollow mesoporous silica spheres by a sol–gel/emulsion approach. *Microporous and Mesoporous Materials* **2010,** 127 (1–2), 67-72.

157. Zheludkevich, M.L.; Serra, R.; Montemor, M.F.; Salvado, I.M.M.; Ferreira, M.G.S., Corrosion protective properties of nanostructured sol-gel hybrid coatings to AA2024-T3. *Surface and Coatings Technology* **2006,** 200 (9), 3084-3094.

158. Kral, J.; Smid, R.; Ramos, H.M.G.; Ribeiro, A.L. In *Thickness measurement using transient eddy current techniques*, Instrumentation and Measurement Technology Conference (I2MTC), 2011 IEEE, 10-12 May 2011; 2011; pp 1-6.

159. QUALICOAT, Specifications for a quality label for liquid and powder organic coatings on aluminium for architectural applications. *http://www.qualicoat.net* **2012**.

160. Isaacs, H.S.; Davenport, A.J.; Shipley, A., The Electrochemical Response of Steel to the Presence of Dissolved Cerium. *Journal of The Electrochemical Society* **1991,** 138 (2), 390-393.

161. Akid, R.; Garma, M., Scanning vibrating reference electrode technique: a calibration study to evaluate the optimum operating parameters for maximum signal detection of point source activity. *Electrochimica Acta* **2004,** 49 (17–18), 2871-2879.

162. Borisova, D. Fabrication of nanostructered materials for feedback active coatings. Master thesis, Gottfried Wilhelm Leibniz Universität Hannover, Hannover, **2009**.

163. Iler, R.K., *The Chemistry of Silica: Solubility, Polymerization, Colloid and Surface Properties, and Biochemistry.* John Wiley and Sons: New York **1979**; p 866.

164. Thommes, M.; Smarsly, B.; Groenewolt, M.; Ravikovitch, P.I.; Neimark, A.V., Adsorption Hysteresis of Nitrogen and Argon in Pore Networks and Characterization of Novel Micro- and Mesoporous Silicas. *Langmuir* **2005,** 22 (2), 756-764.

165. Kruk, M.; Jaroniec, M., Gas Adsorption Characterization of Ordered Organic−Inorganic Nanocomposite Materials. *Chemistry of Materials* **2001,** 13 (10), 3169-3183.

166. Wang, J.; Xia, Y.; Wang, W.; Poliakoff, M.; Mokaya, R., Synthesis of mesoporous silica hollow spheres in supercritical CO_2/water systems. *Journal of Materials Chemistry* **2006,** 16 (18), 1751-1756.

167. Cauda, V.; Schlossbauer, A.; Kecht, J.; Zürner, A.; Bein, T., Multiple Core-Shell Functionalized Colloidal Mesoporous Silica Nanoparticles. *Journal of the American Chemical Society* **2009,** 131 (32), 11361-11370.

168. Vallet-Regí, M.; Balas, F.; Arcos, D., Mesoporöse Materialien für den Wirkstofftransport. *Angewandte Chemie* **2007,** 119 (40), 7692-7703.

169. Hollamby, M.J.; Borisova, D.; Brown, P.; Eastoe, J.; Grillo, I.; Shchukin, D., Growth of Mesoporous Silica Nanoparticles Monitored by Time-Resolved Small-Angle Neutron Scattering. *Langmuir* **2011,** 28 (9), 4425-4433.

170. Né, F.; Testard, F.; Zemb, T.; Grillo, I., How Does ZrO_2/Surfactant Mesophase Nucleate? Formation Mechanism. *Langmuir* **2003,** 19 (20), 8503-8510.

171. Urata, C.; Aoyama, Y.; Tonegawa, A.; Yamauchi, Y.; Kuroda, K., Dialysis process for the removal of surfactants to form colloidal mesoporous silica nanoparticles. *Chemical Communications* **2009,** (34), 5094-5096.

172. Keppeler, M.; Holzbock, J.; Akbarzadeh, J.; Peterlik, H.; Hüsing, N., Inorganic–organic hybrid materials through post-synthesis modification: Impact of the treatment with azides on the mesopore structure. *Beilstein Journal of Nanotechnology* **2011,** 2, 486-498.

173. Flodström, K.; Teixeira, C.V.; Amenitsch, H.; Alfredsson, V.; Lindén, M., In Situ Synchrotron Small-Angle X-ray Scattering/X-ray Diffraction Study of the Formation of SBA-15 Mesoporous Silica. *Langmuir* **2004,** 20 (12), 4885-4891.

174. Fedeyko, J.M.; Vlachos, D.G.; Lobo, R.F., Formation and Structure of Self-Assembled Silica Nanoparticles in Basic Solutions of Organic and Inorganic Cations. *Langmuir* **2005,** 21 (11), 5197-5206.

175. Zajíčková, Z.; Párkányi, C., Photodegradation of 2-mercaptobenzothiazole disulfide and related benzothiazoles. *Journal of Heterocyclic Chemistry* **2008,** 45 (2), 303-306.

176. Woods, R.; Hope, G.A.; Watling, K., A SERS spectroelectrochemical investigation of the interaction of 2-mercaptobenzothiazole with copper, silver and gold surfaces. *Journal of Applied Electrochemistry* **2000,** 30 (11), 1209-1222.

177. U.S. Environmental Protection Agency. *Hazard Characterization Document* **June 2010**.

178. Clark, W.J.; Ramsey, J.D.; McCreery, R.L.; Frankel, G.S., A Galvanic Corrosion Approach to Investigating Chromate Effects on Aluminum Alloy 2024-T3. *Journal of the Electrochemical Society* **2002,** 149 (5), B179-B185.

179. He, J.; Gelling, V.J.; Tallman, D.E.; Bierwagen, G.P., A Scanning Vibrating Electrode Study of Chromated-Epoxy Primer on Steel and Aluminum. *Journal of the Electrochemical Society* **2000,** 147 (10), 3661-3666.

180. Cohen, S.M., Review - Replacements for Chromium Pretreatments on Aluminum. *Corrosion* **1995,** 51 (1), 71-78.

181. Rickerby, D.S., A review of the methods for the measurement of coating-substrate adhesion. *Surface and Coatings Technology* **1988,** 36 (1–2), 541-557.

182. Mohler, J.B., Practical adhesion testing. *Metal Finishing* **1983,** 81 (9), 71-73.

183. Standard Test Method for Pull-Off Strength of Coatings Using Portable

Adhesion Testers. *ASTM International* **2009,** DOI: 10.1520/D4541-09E01, ASTM Standard D4541.

184. Galio, A.F.; Lamaka, S.V.; Zheludkevich, M.L.; Dick, L.F.P.; Müller, I.L.; Ferreira, M.G.S., Inhibitor-doped sol–gel coatings for corrosion protection of magnesium alloy AZ31. *Surface and Coatings Technology* **2010,** 204 (9–10), 1479-1486.

185. Pratt Jr, K.W.; Johnson, D.C., Vibrating wire electrodes--I. Literature review, design and evaluation. *Electrochimica Acta* **1982,** 27 (8), 1013-1021.

186. Lamaka, S.V.; Taryba, M.; Montemor, M.F.; Isaacs, H.S.; Ferreira, M.G.S., Quasi-simultaneous measurements of ionic currents by vibrating probe and pH distribution by ion-selective microelectrode. *Electrochemistry Communications* **2011,** 13 (1), 20-23.

187. Worsley, D.A.; McMurray, H.N.; Belghazi, A., Determination of localised corrosion mechanisms using a scanning vibrating reference electrode technique. *Chemical Communications* **1997,** (24), 2369-2370.

188. Fix, D.; Skorb, E.V.; Shchukin, D.G.; Möhwald, H., Quantitative analysis of scanning electric current density and pH-value observations in corrosion studies. *Measurement Science & Technology* **2011,** 22 (7).

189. Grundmeier, G.; Schmidt, W.; Stratmann, M., Corrosion protection by organic coatings: electrochemical mechanism and novel methods of investigation. *Electrochimica Acta* **2000,** 45 (15–16), 2515-2533.

190. Zheludkevich, M.L.; Serra, R.; Montemor, M.F.; Yasakau, K.A.; Salvado, I.M.M.; Ferreira, M.G.S., Nanostructured sol–gel coatings doped with cerium nitrate as pre-treatments for AA2024-T3: Corrosion protection performance. *Electrochimica Acta* **2005,** 51 (2), 208-217.

191. Chang, B.-Y.; Park, S.-M., Electrochemical Impedance Spectroscopy. *Annual Review of Analytical Chemistry* **2010,** 3 (1), 207-229.

192. Hsu, C.H.; Mansfeld, F., Technical note: Concerning the conversion of the constant phase element parameter Y-0 into a capacitance. *Corrosion* **2001,** 57 (9), 747-748.

193. Borisova, D.; Möhwald, H.; Shchukin, D.G., Influence of Embedded Nanocontainers on the Efficiency of Active Anticorrosive Coatings for Aluminum Alloys Part II: Influence of Nanocontainer Position. *ACS Applied Materials & Interfaces* **2012,** submitted.

194. Castela, A.S.; Simões, A.M., An impedance model for the estimation of water absorption in organic coatings. Part I: A linear dielectric mixture equation. *Corrosion Science* **2003,** 45 (8), 1631-1646.

Acknowledgements

I'd also like to thank all group members and co-workers, who contributed to this work, helped me overcome everyday research difficulties and supported me during the last three years. Special thanks to Alexandra Latnikova, Dmitri Fix, Adam Brotchie, Amy Peterson, Denis Voronin, Valentina Belova, Tatiana Kolesnikova, Torsten Sievers, John Berg, Andre Skirtach, Mihaela Delcea, Stephanie Riedel, Radostina Georgieva and Georgi Gochev.

The continuous support of my friends from all over the world helped me during the course of my Phd work. Thank you all for believing in me!

Last but not least, I'd like to kindly thank my family for their sacrifices, help and encouragement without which I couldn't have gone my educational path. Their constant love and belief in me were the main driving force to complete this work.

Благодаря ви много, скъпо семейство!

Declaration of authorship

I hereby declare, that I completed this work without assistance from any third party and without using other references, sources or aids than the cited ones. I certify that this thesis has not been submitted in the same or similar form to any other examination office and has not been accepted as an examination part.

Potsdam, 01. October 2012

_____

Dimitriya Borisova